

## RESTRICTED



FP7-ICT Future Networks  
SPECIFIC TARGETED RESEARCH PROJECT  
Project Deliverable

<b>PHYDYAS Doc. Number</b>	PHYDYAS_ 005
<b>Project Number</b>	ICT – 211887
<b>Project Acronym+Title</b>	PHYDYAS – PHYsical layer for DYnamic AccesS and cognitive radio
<b>Deliverable Nature</b>	Report
<b>Deliverable Number</b>	D2.2
<b>Contractual Delivery Date</b>	January 1, 2009
<b>Actual Delivery Date</b>	January 28, 2009
<b>Title of Deliverable</b>	Synchronization and initialization with single antenna. Blind Techniques
<b>Contributing Workpackage</b>	WP2
<b>Project starting date; Duration</b>	01/01/2008; 30 months
<b>Dissemination Level</b>	RE
<b>Author(s)</b>	Mario Tanda (UNINA – WP2 leader), Markku Renfors (TUT), Jérôme Louveaux (UCL), Maurice Bellanger (CNAM)

**Abstract:** The synchronization techniques for FBMC systems which were introduced in document D2.1 are extended and completed in the present report. Simulation results are discussed. A blind approach based on cyclostationarity properties of the FBMC signals is proposed with simulation results. Reference to the WiMAX burst structure for downlink and uplink is considered. Some tracking issues are also discussed. To conclude, the main achievements of WP2 are listed and strategies for initialization are proposed.

## TABLE OF CONTENTS

<b>1</b>	<b>Overview of the Work Carried out Under WP2: Synchronization and Initialization .....</b>	<b>9</b>
<b>2</b>	<b>Synchronization and initialization in existing systems (WiMAX) and future systems .....</b>	<b>12</b>
<b>3</b>	<b>Synchronization and Initialization in Downlink .....</b>	<b>14</b>
3.1	FBMC signals in the presence of synchronization errors .....	14
3.2	Preamble-based Joint CFO and FTD Synchronization .....	15
3.2.1	LS Estimator .....	16
3.2.2	ML Estimator .....	18
3.2.3	Performance Evaluation of Preamble-Based Estimators .....	21
3.2.4	Comparison with OFDM Systems .....	24
3.3	Blind Synchronization .....	27
3.3.1	Cyclostationarity properties of the FBMC Signal .....	27
3.3.2	Blind ML CFO Synchronization .....	28
3.3.3	Simplified CFO Synchronization .....	30
3.3.4	Blind ML Symbol Timing Synchronization .....	31
3.3.5	Performance Evaluation of CFO Estimators .....	32
3.3.6	Performance Evaluation of Symbol Timing Estimators .....	34
3.3.7	Comparisons With Preamble-based Estimators .....	36
3.4	Synchronization Based on Scattered Pilots .....	37
3.5	Decision-directed tracking of fractional time delay .....	53
3.5.1	Simulation setup .....	53
3.5.2	Comparison with Theoretical Results .....	54
3.5.3	Tracking Simulations .....	58
3.5.4	Conclusion .....	60
3.6	Filter Bank Memory Preloading and Frequency Domain Processing .....	61
3.6.1	The Memory Preloading Concept .....	63
3.6.2	Transmission Parameter Estimation .....	66
3.6.3	Compatibility with OFDM Transmission Parameter Estimation .....	68
3.7	Burst structures .....	69
3.7.1	Burst Truncation in WiMAX-Like FBMC System .....	69
3.7.2	Burst Truncation in Cognitive Radio Scenarios .....	71
3.7.3	Numerical Results .....	71
<b>4</b>	<b>Synchronization and Initialization in Uplink .....</b>	<b>78</b>
4.1	Synchronization Based on Preamble .....	78
4.1.1	Joint CFO and symbol Timing Estimator .....	78
4.1.2	Numerical Results .....	80
4.2	Synchronization Based on Scattered Pilots .....	82
4.3	The Case of Arbitrary Timing Offset .....	92
4.3.1	Sub-channel Equalization with Timing Offset .....	92
4.3.2	Simulation Results .....	94
<b>5</b>	<b>Achievements and Conclusion .....</b>	<b>95</b>
<b>6</b>	<b>References .....</b>	<b>97</b>

**List of Acronyms:**

A/D	Analog-to-Digital
AFB	Analysis Filter Bank
AMC	Adaptive Modulation and Coding
AWGN	Additive White Gaussian Noise
BER	Bit Error Rate
CFO	Carrier Frequency Offset
CP-OFDM	Orthogonal Frequency Division Multiplexing with Cyclic Prefix
D/A	Digital-to-Analog
DAC	Digital-to-Analog Conversion
DFT	Discrete Fourier Transform
DL	Downlink
EMFB	Exponentially Modulated Filter Bank
FB	Filter Bank
FBMC	Filter Bank based MultiCarrier
FDD	Frequency Division Duplexing
FDMA	Frequency Division Multiple Access
FFT	Fast Fourier Transform
FIR	Finite Impulse Response
FTD	Fractional Time Delay
IDFT	Inverse Discrete Fourier Transform
IFFT	Inverse Fast Fourier Transform
ICI	Intercarrier Interference
ISI	Intersymbol Interference
LS	Least Squares
MAI	Multiple Access Interference
MDFT	Modified Discrete Fourier Transform
MIMO	Multiple-Input Multiple-Output
ML	Maximum Likelihood
MMSE	Minimum Mean Squared Error
MS	Mobile Station
NPR	Nearly Perfect Reconstruction
OFDM	Orthogonal Frequency Division Multiplexing
OFDMA	OFDM Access
OQAM	Offset Quadrature Amplitude Modulation
PAPR	Peak-to-Average Power Ratio
PR	Perfect Reconstruction
PSD	Power Spectrum Density
PUSC	Partial Usage of Subchannels
QAM	Quadrature Amplitude Modulation
QPSK	Quadrature Phase Shift Keying
QoS	Quality-of-Service
RC	Raised Cosine
RHS	Right hand side
RMSE	Root Mean Squared Error

SFB	Synthesis Filter Bank
SNR	Signal-to-Noise Ratio
TDD	Time Division Duplexing
TDMA	Time Division Multiple Access
TED	Timing Error Detector
UL	Uplink
WiMAX	Worldwide Interoperability for Microwave Access

## Notations

$\angle\{x\}$	the argument of a complex number $x$ in $[0, 2\pi)$ ,
$\text{Re}\{\cdot\}$	real part
$\text{Im}\{\cdot\}$	imaginary part
$(\cdot)^*$	complex conjugation
$ \cdot $	absolute value
$M$	overall number of subcarriers, FFT size
$M_u^i$	number of used subcarriers of the $i$ th user (in single-user case, index $i$ is dropped)
$\mathcal{M}_u^i$	set of used subcarriers of the $i$ th user
$M_v$	number of virtual (unused) subcarriers
$K$	overlapping factor in prototype filter design
$\alpha$	roll-off factor in prototype filter design
$L_p$	prototype filter length
$L_{eq}$	subcarrier equalizer length
$T_s$	sampling interval (at SFB output and AFB input)
$f_s$	sampling rate (at SFB output and AFB input) $f_s = 1/T_s$
$T$	OQAM symbol duration; $T = MT_s$
$\Delta f$	subcarrier spacing, $\Delta f = 1/T = f_s/M$
$k$	subcarrier index ( $k=0, \dots, M-1$ ; $k=0$ corresponds to center subcarrier)
$l$	time index at OQAM symbol rate ( $\rightarrow T$ )
$n$	time index at OQAM subsymbol rate ( $\rightarrow T/2$ )
$m$	time index at SFB output/AFB input ( $\rightarrow T/M$ )
$i$	user index in multiuser cases
$U$	number of users
$v^R[n]$	real part of (arbitrary) complex sequence $v[n]$
$v^I[n]$	imaginary part of (arbitrary) complex sequence $v[n]$
$p(t)$	prototype filter impulse response, continuous-time model
$p[m]$	prototype filter impulse response, discrete-time <sup>(1)</sup> $p[m] = \sqrt{T_s} p(mT_s)$
$P(z)$	prototype filter transfer function
$f_k[m]$	analysis filter impulse response for subchannel $k$
$F_k(z)$	analysis filter transfer function for subchannel $k$
$G_k(z)$	synthesis filter transfer function for subchannel $k$
$g_k[m]$	synthesis filter impulse response for subchannel $k$ $g_k[m] = p[m] e^{j \frac{2\pi}{M} k \left( m - \frac{L_p-1}{2} \right)}$

$p_{k,n}[m]$  SFB impulse response for real symbol  $d_{k,n}$  (see also definition of  $s[m]$ )

$$\begin{aligned} p_{k,n}[m] &= \theta_{k,n} \beta_{k,n} g_k[m - nM/2] \\ &= \theta_{k,n} \beta_{k,n} p[m - nM/2] e^{j \frac{2\pi}{M} km} \end{aligned}$$

$\theta_{k,n}$  phase mapping between real data sequence and complex samples at the SFB input  
In general,

$$\theta_{k,n} = \begin{cases} \pm 1 & \text{for } k+n \text{ even} \\ \pm j & \text{for } k+n \text{ odd} \end{cases}$$

The recommended choice (following Siohan's papers) is <sup>(2)</sup>:

$$\theta_{k,n} = j^{k+n}$$

$$\beta_{k,n} = e^{j 2\pi k \left( -\frac{n}{2} - \frac{L_p - 1}{2M} \right)}$$

$d_{k,n}^i$  transmitted sequence of the  $i$ th user (data & pilots) (real)

$x_{k,n}$  observed ideal (without channel) complex sample sequence at AFB output,

$$\theta_{k,n}^* x_{k,n} = d_{k,n} + j u_{k,n}$$

Here  $u_{k,n}$  is the un-interesting part of the received complex samples.

$$\tilde{x}_{k,n} = \theta_{k,n}^* x_{k,n}$$

$y_{k,n}$  observed channel-distorted complex sample sequence at AFB output

$\tilde{d}_{k,n}$  real part of the subcarrier sequence after equalization and multiplication by  $\theta_{k,n}^*$

$\hat{d}_{k,n}$  detected sequence (real)

$s[m]$  transmitted sequence at SFB output, single user case

$$\begin{aligned} s[m] &= \sum_{k \in \mathcal{M}_u} \sum_{n=-\infty}^{\infty} d_{k,n} \theta_{k,n} g_k[m - nM/2] \\ &= \sum_{k \in \mathcal{M}_u} \sum_{n=-\infty}^{\infty} d_{k,n} \theta_{k,n} p[m - nM/2] e^{j \frac{2\pi}{M} k \left( m - n\frac{M}{2} - \frac{L_p - 1}{2} \right)} \\ &= \sum_{k \in \mathcal{M}_u} \sum_{n=-\infty}^{\infty} d_{k,n} \theta_{k,n} (-1)^{kn} p[m - nM/2] e^{j \frac{2\pi}{M} k \left( m - \frac{L_p - 1}{2} \right)} \\ &= \sum_{k \in \mathcal{M}_u} \sum_{n=-\infty}^{\infty} d_{k,n} \theta_{k,n} \beta_{k,n} p[m - nM/2] e^{j \frac{2\pi}{M} km} \\ &= \sum_{k \in \mathcal{M}_u} \sum_{n=-\infty}^{\infty} d_{k,n} p_{k,n}[m] \end{aligned}$$

$s_i[m]$  transmitted sequence at SFB output in the uplink multiuser FBMC system, e.g.,

$$s_i[m] = \sum_{k \in \mathcal{M}_i} \sum_{n=-\infty}^{\infty} d_{k,n} p_{k,n}[m]$$

$s(t)$  transmitted continuous-time signal ( $s_i(t)$  correspondingly for user  $i$  in multiuser case)

$$s(t) = \sum_{k \in \mathcal{M}_i} \sum_{n=-\infty}^{\infty} d_{k,n} \theta_{k,n} (-1)^{kn} p\left(t - n \frac{T}{2}\right) e^{j2\pi k \left(\Delta f t - \frac{L_p - 1}{2M}\right)}$$

$r(t)$  received continuous-time signal in the uplink multiuser FBMC system

$$r(t) = \sum_{i=1}^U e^{j2\pi \left(\frac{\varepsilon_i}{T} t\right)} h_i(t, \tau) * s_i(t) + \eta(t) \quad \text{general case}$$

$$r(t) = \sum_{i=1}^U e^{j2\pi \left(\frac{\varepsilon_i}{T} t\right)} \sum_{p=0}^{P_i-1} c_{i,p} s_i(t - \tau_{i,p}) + \eta(t) \quad \text{discrete multipath case}$$

$$r(t) = \sum_{i=1}^U e^{j2\pi \left(\frac{\varepsilon_i}{T} t\right)} c_i s_i(t - \tau_i) + \eta(t) \quad \text{AWGN case}$$

$$= \sum_{i=1}^U e^{j2\pi \left(\frac{\varepsilon_i}{T} t + \phi_i\right)} |c_i| s_i(t - \tau_i) + \eta(t)$$

$\varepsilon_i$  carrier frequency offset of the  $i$ th user, normalized to subcarrier spacing

$\phi_i$  carrier phase offset (radians) of the  $i$ th user in the AWGN model

$h_i(t, \tau)$  time-variant channel impulse response of  $i$ th user

$P_i$  number of paths in the multipath channel model of user  $i$

$c_{i,p}$  complex gain of the  $p$ th path of the channel of user  $i$

$\tau_{i,p}$  delay of the  $p$ th path of the channel of user  $i$

$\tau_i$  timing offset of the  $i$ th user in the AWGN model

$\eta(t)$  complex envelope of white (Gaussian) noise whose real and imaginary parts are statistically independent and have a power spectral density level of  $N_0$

$\sigma_\eta^2$  channel noise variance

$N_0$  one-sided noise power spectral density of white channel noise

$r[m]$  received complex sequence at AFB input

$\eta[m]$  channel noise

$h_i[m]$  discrete-time channel impulse response for user  $i$  in block-fading model

$H_i(e^{j\omega})$  channel frequency response for user  $i$

$H_k$  channel response of subcarrier  $k$  (assuming flat-fading and time invariant/block-fading case)

$H_{k,n}$  channel response for subcarrier  $k$  and symbol  $n$  (assuming flat-fading and time variant case)

$H_{k,n}^{p,q}$  channel response for subcarrier  $k$  and symbol  $n$  from TX antenna  $p$  to RX antenna  $q$

$w_k[n]$  subcarrier-wise channel equalizer impulse response for subchannel  $k$

**Notes:**

<sup>(1)</sup> This assumes causal continuous-time prototype filter impulse response, which is different from Siohan's continuous-time model.

<sup>(2)</sup> The choice of  $\theta_{k,n}$ , i.e., the signs in mapping real data sequence to complex samples at the SFB input is an internal choice of the filter bank module (i.e., the definition of  $x_{k,n}$  above can be assumed to be valid in any case). However, it has an effect on the signal models at the SFB output and for the complex sequences at the AFB output. In the receiver side,  $\beta_{k,n}^*$  is implemented before the subband processing, and  $\theta_{k,n}^*$  after it. With this choice, all the subchannels are centered at DC at the subchannel processing stage.



# 1 Overview of the Work Carried out Under WP2: Synchronization and Initialization

The objectives of the WP2 is to study techniques and provide tools for the design of an efficient strategy for initialization and synchronization in FBMC (filter bank based multicarrier) systems. A number of the techniques and schemes which have been developed for OFDM (orthogonal frequency division multiplexing) apply to FBMC as well, but they might be not optimal in this context. Therefore, the objective is to exploit the specificities of FBMC and propose specific approaches potentially leading to a more optimized design. The present overview is intended to guide the reader.

The relevant specificities of FBMC are :

## *1) the impulse response of the prototype filter.*

This is a major difference with OFDM, because it introduces a transition phase for both the initialization signals and the data. This implies that more symbols are necessary to complete the initialization process. In fact, two situations can be distinguished :

- cognitive radio : the insertion of the signal in the spectrum must be made without any perturbation of the neighbouring signals. The transition phases have to be fully preserved.
- a spectrum gap exists between the systems, e.g. WiMAX-like case. The OFDM techniques can be used or similar techniques can be developed to reduce the impact of the prototype filter impulse response.

## *2) multi-tap sub-channel equalizer.*

With respect to OFDM, an additional operation is introduced, namely the determination of the initial values of the coefficients, which are derived from the channel measurements. An important point is that the multi-tap sub-channel equalizer gives the opportunity to track the evolution of the channel and potentially get rid of the scattered pilots in the bursts.

## *3) the independence of the sub-channels.*

Since groups of sub-channels can be made independent, there is no need to synchronize these groups. In particular, in the uplink, there is no need to perform time-alignment of different users before the establishment of the connection between the mobile and the base station. On the contrary, an OFDM system such as WiMAX requires such precise time-alignment. Therefore, two situations can be distinguished: full block of sub-channels and groups of sub-channels.

An illustration of the impact of the prototype filter impulse response is given in Figure 1-1, which shows the principle of initialization. The overlapping factor of the filter is taken as  $K=4$ , which implies that the transition phase at the receiver output has the length  $K-1=3$  symbols. A set of 2 preamble symbols P1 is used for the estimation of the carrier frequency offset (CFO), the timing offset and the channel frequency response. If conventional techniques are used for the estimation, the received preamble symbols must be free of any interference, which implies that a transition phase is introduced for the data sequence, to avoid overlap in time. A significant part of the work in WP2 has focused on studying approaches which eliminate or reduce the length of these transition phases.

The preamble transition phase can be eliminated by the filter bank memory preloading technique described in Section 3.5 of deliverable D2.2.

A significant reduction of both transition phases is obtained by the burst truncation scheme studied in Chapter 6 of D2.1 and Section 3.6 of D2.2.

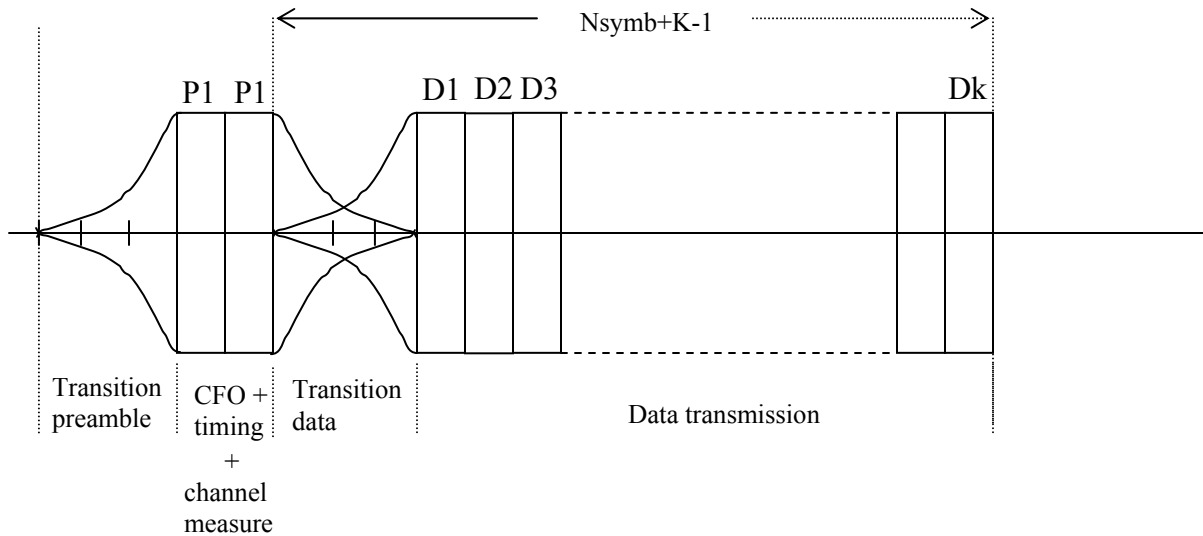


Figure 1-1. Principle of FBMC initialization

Now, in a multicarrier system, the estimations can be carried out in the time domain or in the frequency domain. The carrier frequency offset and the timing offset affect all the sub-channels in the same way. Therefore, it is appealing to estimate and compensate them in the time domain, as is usually done in OFDM systems. For the CFO, it is no problem because the principle consists of exploiting two or more identical symbols. However, the situation is different for the timing offset estimation because it is the contrast between the preamble symbols and other symbols which is exploited, and the impulse response of the prototype filter blurs the boundaries. Therefore, more involved techniques are needed if timing offset estimation in the time domain is envisaged and these involved techniques can also provide the CFO estimation.

Two approaches have been studied for the joint estimation of CFO and timing offset. The first one, presented in Section 3.1 of D2.1 and in Section 4.1 of D2.2 is based on least squares. It is independent of the channel frequency response but the performance is limited, particularly for the timing offset. The second approach relies on the maximum likelihood (ML) principle and it is presented in Section 4.2 of D2.1 and 3.2.2 of D2.2. The performance is improved but it is sensitive to the channel response because it exploits a training sequence. The extension of the ML approach to the blind case, exploiting cyclostationarity is presented in Section 3.2 of D2.2.

In FBMC transmission and a base station ruled network, the group of sub-channels case appears in the uplink. Chapter 4 of D2.2 is dedicated to applying the above estimators to this situation. In addition, it is shown in Section 4.4 of D2.2 that good quality of transmission can be achieved in the presence of arbitrary timing offsets, with the help of sub-channel equalizers. It is an important result, because it shows that precise time-alignment is not a prerequisite for establishing a link and this is crucial in opportunistic or peer-to-peer communications.

Also the use of scattered pilots for CFO and timing offset estimation has been investigated. Scattered pilots are used in the synchronization context mostly for tracking small CFO and timing offset variations

during data transmission. However, combining the pilot based estimation methods with efficient frequency-domain CFO and timing offset compensation techniques, it is possible to handle considerable synchronization offsets with good detection performance. The basic methods for scattered pilot based synchronization are developed in Chapter 5 of D2.1, and extensive performance evaluation results are presented in Section 3.4 of D2.2 for downlink and in Section 4.2 for the uplink.

Decision-directed synchronization methods are interesting because they could help to reduce the overhead due to preamble and/or scattered pilots. A decision directed timing offset tracking method is introduced in Chapter 7 of D2.1, and more complete performance analysis is found in Section 4.4 of D2.2.

## 2 Synchronization and initialization in existing systems (WiMAX) and future systems

As an introduction, some characteristics of present OFDM systems are reviewed and the potential of FBMC to meet the challenges of future systems is discussed.

Existing wireless communication systems are ruled by a base station (BS) and they operate in a synchronized manner. The initial synchronization of a mobile station (MS), after power-up, is not time critical and is allowed to take at least some hundreds of milliseconds. After initial synchronization, basic sync is maintained as long as the MS is connected to the network. Basic sync means synchronization of carrier frequencies and downlink timing with a resolution which is sufficient for detecting at least the data streams which are transmitted by the base station with low-order modulations (such as control data, which is vital for the operation of the network).

To maintain the synchronization, a MS carries out the following functionalities during the normal operation:

- Tracking the synchronization parameters (i) CFO and (ii) timing, here referred to as fractional time delay (FTD). These parameters are varying rather slowly, and fairly long integration times can be used to achieve good synchronization quality with simple algorithms. Any MS can use all characteristics of the downlink waveform, which contains large amount of training symbols or pilots for synchronization purposes.
- Compensation of small synchronization errors may be needed, especially with high mobility and high-order modulations. However, single coefficient channel equalization is often capable of handling such small synchronization errors.
- Synchronization should be maintained also in idle mode, i.e., during the wake-up periods.
- In handover situations, fairly fast (tens of ms) synchronization to the new base-station is needed.

On the base station side, the main synchronization task is to measure the CFO and FTD of each user and transmit feedback information to the mobiles to help them keep the synch. Especially in OFDM and TDMA based systems, it is important to keep the time-alignment of different uplink users. The synchronization tolerances are fairly tight, allowing demodulation of the uplink signals with the help of single coefficient channel equalization. Especially with high-order modulation, fine synchronization independently for each uplink user might be needed or could be useful anyway. The uplink CFO and FTD estimation can be based on the normal uplink waveforms, which contain significant amount of pilots for synchronization and channel estimation purposes. However, initial time synchronization cannot be achieved in the normal transmission mode without endangering other users' signal quality. Furthermore, in case of low uplink data rate, the number of pilots during normal operation may be too small for reliable synchronization. For these situations, special elements are included in the uplink waveforms: ranging zones and sounding zones. They give, for the mobiles, the possibility for initial entry without good time synchronization. During normal operation, base station may request a mobile to send ranging signal for checking the sync, if the pilots in uplink transmission are not sufficient.

Existing wireless communication systems are further characterized by dedicated frequency bands and well-defined frequency channels. After analog and digital receiver front-ends, the signal contains only the transmissions allocated to that channel, which have well-controlled dynamics under the radio resource management functionalities of the wireless network. No strong interfering spectral components due to other kinds of waveforms are expected to be present. In OFDM systems, different user signals are

quasi-synchronous due to the use of cyclic prefixes, and can be separated using FFT-based processing. Naturally, there are distorting effects which, e.g., introduce inter-carrier interference (ICI), but these effects are kept under control by proper system and algorithm designs.

In such an environment, synchronization algorithms can be implemented in time domain, basically by correlating the received signal with the waveform corresponding to the known training signal or pilot pattern. In case of an OFDM system, this can be done, no matter whether the training signal is defined in time or frequency domain. Alternatively, if the reference is based on pilots constructed in frequency domain, frequency domain methods can be used for synchronization parameter estimation, and compensation of synchronization errors as well. During initial synchronization, and always when running only the synchronization parameter estimation, time-domain processing is expected to have lower complexity, because transform processing would need to be done only for synchronization purposes for the frequency-domain methods.

As described, the synchronization in existing wireless communication systems is fairly robust and reliable. However, there is significant complexity of the overall concept, and also significant overhead in terms of data transmission capacity. The overheads could be reduced by developing blind or semi-blind synchronization methods which are able to operate with reduced training/pilot overhead. But there are great challenges in doing this, especially regarding channel estimation, since the mobile channel characteristics are fast varying in comparison to the synchronization parameters.

The high system-level complexity of feedback-based synchronization schemes can be reduced by developing waveforms which are more robust than OFDM against CFO and timing offsets of different uplink users. FBMC waveforms are promising in this sense, since they do not rely on the use of cyclic prefixes and the filter bank provides a frequency domain separation between the users

The scarcity of frequency spectrum which can be used in wireless communications is a significant factor, which has given raise to the concepts of flexible dynamic spectrum use and cognitive radio. In this context, the used frequency band is not anymore dedicated to a specific service and specific waveforms. The band cannot be expected anymore to be free of other waveforms, the utilized frequency spectrum may be discontinuous, and the dynamics of signal power levels are not well-controlled anymore. This calls for efficient means to separate the portions of the frequency spectrum, which are utilized in a specific transmission, from other portions which are considered as interference. Filter banks are ideal for this purpose.

In OFDM systems, the FFT provides fairly good selectivity to signal elements which are synchronized to the CP structure, but not to any other spectral components. Therefore, the channel selectivity has to be implemented in the analog and digital front-end, as in traditional receiver architectures. Filter banks don't have this limitation, and they can be used for implementing major part of the channel selectivity, thus relaxing the digital front-end complexity. Furthermore, in dynamic spectrum use scenarios, filter banks are superior in terms of flexibility, in comparison to any other digital filtering structure.

As for the synchronization functionalities in case of dynamic spectrum use, it is clear that synchronization parameter estimation cannot be implemented in time-domain before major part of the selectivity is implemented and strong interferers are suppressed. If the filter bank itself is used for implementing the selectivity, the feasibility of time-domain synchronization becomes questionable.

Therefore, in the context of cognitive radio, there is a strong motivation to develop synchronization methods, which are operating in frequency domain, utilizing the subchannel signals only. The operation ranges of frequency-domain CFO and FTD estimation methods are often more limited than what is possible in time domain. If significant CFO or FTD exists, then it may also have to be compensated, preferably by frequency-domain methods. In fact, the possibilities for compensation of synchronization errors through frequency domain processing are much better in FBMC than in OFDM systems. Especially, the strict time-alignment within the CP interval in OFDM can be relaxed, due to the lack of CP-structure and availability of effective subcarrier-wise equalization methods with relatively low complexity.

Alternatively, if frequency-domain compensation is not feasible and fast initialization and synchronization is desired, there is the possibility to re-iterate the processing of current data block by doing time-domain compensation for buffered data, and then the filter bank processing again. This calls for increased instantaneous signal processing capacity, but it needs to be done only for initial synchronization, so the effects on energy consumption would not necessarily be critical.

In the cognitive radio context, networks will not necessarily be ruled by a base station and the global synchronization scheme is an open issue. The high system-level complexity of feedback-based synchronization schemes could be reduced by developing waveforms which are more robust against CFO and timing offsets of different uplink users. FBMC waveforms have a good potential in that respect, since they do not rely on the use of cyclic prefixes and they provide a good frequency domain separation. Further, with opportunistic use of the spectrum, maintaining tight feedback loops between mobiles and base-station is likely to become more difficult. Therefore, it is desirable to get rid of tight feedback loops. However, for optimization purposes, it is preferable to establish and maintain some level of synchronism between connected users.

In the next section, the application of FBMC in downlink is considered.

### 3 Synchronization and Initialization in Downlink

To set the stage, signals and variables are defined.

#### 3.1 FBMC signals in the presence of synchronization errors

In the presence of a timing offset  $\tau$ , a CFO normalized to the subcarrier spacing  $\varepsilon$ , a carrier phase offset  $\phi$  and an attenuation  $|c|$ , the received continuous-time FBMC waveform is

$$r(t) = e^{j2\pi\left(\frac{\varepsilon}{T}t + \phi\right)} |c| s(t - \tau_i) + \eta(t) \quad (1)$$

where

$$s(t) = \sum_{k \in \mathcal{M}_u} \sum_{n=-\infty}^{+\infty} d_{k,n} \beta_{k,n} \theta_{k,n} p\left(t - n\frac{T}{2}\right) e^{j\frac{2\pi}{T}kt} \quad (2)$$

Taking into account the analysis filter bank (see D2.1), the received symbol in the subchannel  $k$  is given by

$$\begin{aligned}
\hat{d}_{k,n} = & d_{k,n} |c| \text{Re} \left\{ b_{k,k}^{\varepsilon} (-\tau) e^{j2\pi \left( \phi - \frac{\tau}{T} k \right)} \right\} \\
& + \sum_{\substack{k' \in \mathcal{M}_u \\ k' \neq k}} d_{k',n} |c| \text{Re} \left\{ b_{k',k}^{\varepsilon} (-\tau) e^{j2\pi \left( \phi - \frac{\tau}{T} k' \right)} \right\} \\
& + \sum_{\substack{k' \in \mathcal{M}_u \\ n' \neq n}} \sum_{\substack{n'=-\infty \\ n' \neq n}}^{+\infty} d_{k',n'} |c| \text{Re} \left\{ b_{k',k}^{\varepsilon} ((n'-n)T/2 - \tau) e^{j2\pi \left( \phi - \frac{\tau}{T} k' \right)} \right\} \\
& + \text{Re} \left\{ \eta(qT_s) e^{-j\frac{2\pi}{T} k q T_s} \beta_{k,n}^* \theta_{k,n}^* \otimes \tilde{p}(qT_s) \right\}_{q=nM/2}
\end{aligned} \tag{3}$$

where

$$b_{k',k}^{\varepsilon} ((n'-n)T/2 - \tau) = \beta_{k,n}^* \theta_{k,n}^* \beta_{k',n'} \theta_{k',n'} e^{j\pi\varepsilon} e^{j\pi n(k'-k)} p((n'-n)T/2 - \tau) \otimes \tilde{p}(nT/2) \tag{4}$$

and  $\tilde{p}(t)$  is the matched filter to  $p(t)$ .

In the presence of synchronization errors and non dispersive channel, at the receiver side the useful term is subject to an attenuation and a phase rotation related to the subchannel index  $k$ , the timing offset  $\tau$ , the phase offset  $\phi$ , the CFO  $\varepsilon$  and the index of information symbol  $n$ . Furthermore, intercarrier interference, intersymbol interference and multiple access interference are present.

Now, it is proposed to begin by the study of a joint approach to estimate the timing offset or fractional time delay (FTD) and the carrier frequency offset.

### 3.2 Preamble-based Joint CFO and FTD Synchronization

With the joint approach for CFO and FTD estimation, we can obtain estimators robust against the other kind of synchronization errors (CFO estimators can be sensitive to FTD errors and vice versa) and potentially efficient, since they exploit the information of a short preamble to obtain at the same time CFO and FTD estimation.

Preamble-based synchronization techniques have been extensively used in OFDM wireless multimedia systems. Precisely, as described in [1] efficient symbol timing and CFO estimators can be obtained by exploiting a preamble having repeated parts. For example, in [2] Schmidl and Cox consider a timing and CFO synchronization scheme that exploits the redundancy associated with a training symbol composed by two identical halves.

In FBMC systems joint FTD and CFO acquisition presents several challenges and in the literature very little effort is dedicated to this issue.

In this section we address the problem of preamble-based synchronization for FBMC systems. In particular, in Subsection 3.2.1 we recall the joint CFO and symbol timing estimator derived in [3] based on the LS approach and exploiting the transmission of a preamble made up of identical FBMC symbols. In Subsection 3.2.2 we address the problem of joint ML phase offset, CFO and symbol timing estimation exploiting the transmission of a known training sequence. Moreover, since the

implementation complexity of the joint ML estimator is high, an approximate ML (AML) synchronization algorithm is considered. In Subsection 3.2.3 the performance of the considered estimators is evaluated both in AWGN and multipath channel.

### 3.2.1 LS Estimator

The proposed data-aided joint CFO and symbol timing estimator is based on the LS approach and exploits the transmission of a training sequence made up of two identical FBMC symbols.

In order to obtain these two identical blocks at the output of the SFB, with reference to the structure of SFB transmitter the contents of the PPN memories must be identical. There are two ways to obtain this:

- a) preload the  $K$  memories with the IFFT output associated with the input preamble symbol  $P$  and apply again the symbol  $P$  at the input of the IFFT during the next symbol, so that the contents of the memories stay the same. Of course, the operation can be repeated, if a sequence of more than 2 identical symbols is desired. An illustration is given in the figure below, for the overlapping factor  $K=4$ .
- b) apply the preamble symbol  $P$  at the input of the IFFT in the transmitter  $K+1$  times. Of course, in this case a transition of  $K-1$  symbols is present.

Then, as soon as 2 identical signal blocks are available, the following simple and fast correlation technique can be implemented.

Let us indicate with  $s_{TR}[m]$  the training sequence obtained by exploiting  $K+1$  identical preamble symbols, whose expression is given by

$$s_{TR}[m] = \sum_{k \in M_u} \sum_{n=0}^{2K+2} d_k^{TR} \theta_{k,n} \beta_{k,n} p[m - nM/2] e^{j \frac{2\pi}{M} km}. \quad (5)$$

After a transient of  $(K-1)M$  samples<sup>1</sup> and, in particular for  $m \in \{(K-1)M, \dots, KM-1\}$ , the training sequence satisfies the following relationship

$$s_{TR}[m] = s_{TR}[m + M]. \quad (6)$$

The transmitted sequence  $s[m]$  feeds a DAC and propagates through a physical channel characterized by AWGN noise  $\eta(t)$ . The received signal  $r(t)$  is filtered with an ideal low-pass filter with a bandwidth of  $1/T_s$  and sampled with a frequency  $f_s = 1/T_s$ , yielding the sequence

$$r[m] = e^{j \frac{2\pi}{M} \tilde{\epsilon} m} c_0 s[m - \tau/T_s] + \eta[m]. \quad (7)$$

Accounting for (6) a joint symbol timing and CFO estimator can be obtained by considering the minimization problem

$$(\hat{\epsilon}, \hat{\tau}) = \arg \min_{(\tilde{\epsilon}, \tilde{\tau})} \left\{ \sum_{m=(K-1)M}^{KM-1} \left| r[m + \tilde{\tau}/T_s] - r[m + M + \tilde{\tau}/T_s] e^{-j 2\pi \tilde{\epsilon}} \right|^2 \right\} \quad (8)$$

where  $\tilde{\epsilon}$  and  $\tilde{\tau}$  are trial values for CFO and symbol timing, respectively.

<sup>1</sup> The transient can be avoided if preloading techniques are used.



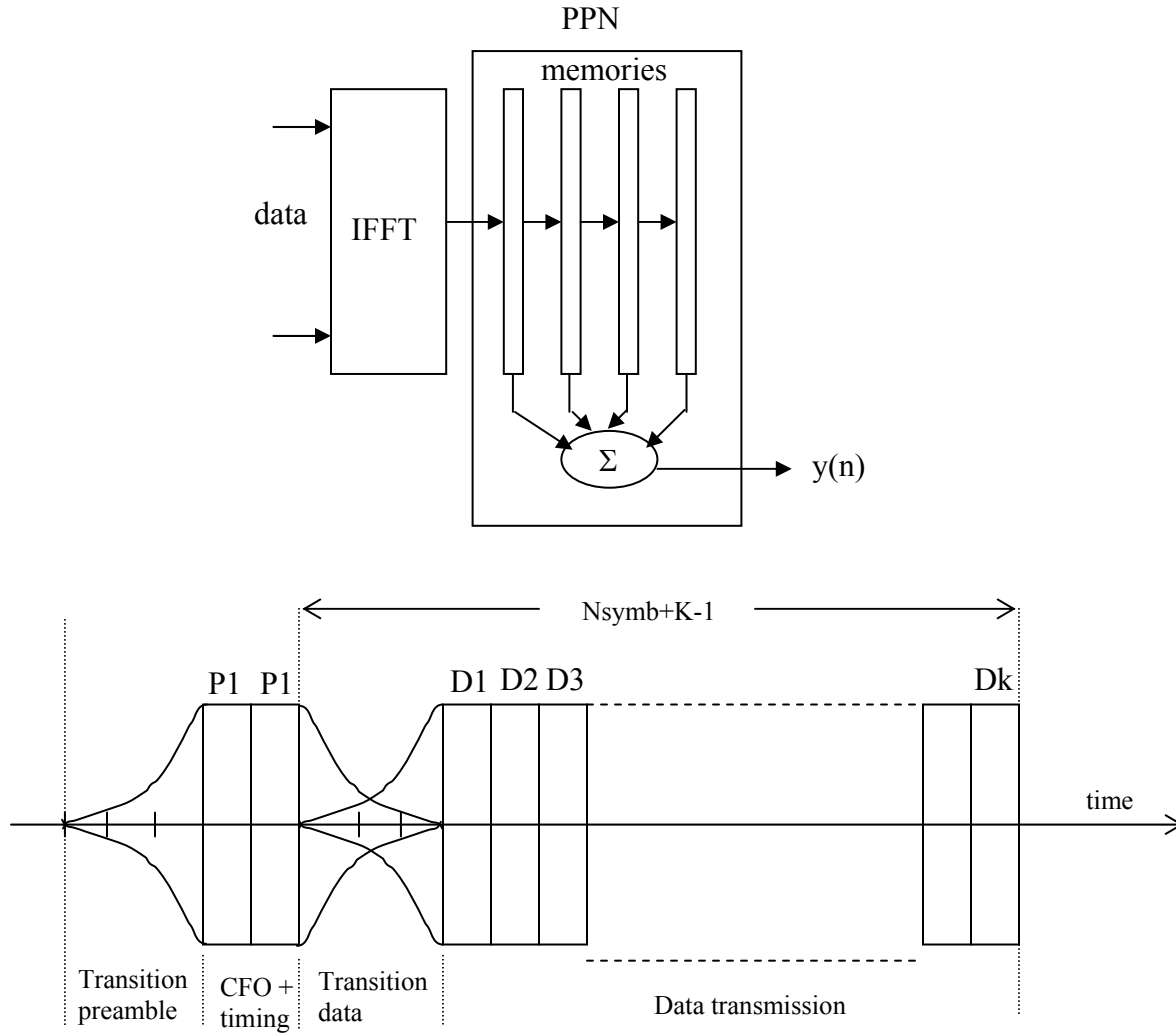


Figure 3-1. SFB in the transmitter and structure of the burst

The minimization in (8) leads to the following joint CFO and symbol timing estimator referred to as LS estimator

$$\hat{\tau}_{LS} = \arg \max_{\tilde{\tau}} \{2|R(\tilde{\tau})| - Q(\tilde{\tau})\} \quad (9)$$

and

$$\hat{\epsilon}_{LS}(\hat{\tau}_{LS}) = \frac{1}{2\pi} \angle \{R(\hat{\tau}_{LS})\} \quad (10)$$

with

$$R(\tilde{\tau}) = \sum_{m=(K-1)M}^{KM-1} r^*[m + \tilde{\tau}/T_s] r[m + M + \tilde{\tau}/T_s] \quad (11)$$

and

$$Q(\tilde{\tau}) = \sum_{m=(K-1)M}^{KM-1} |r[m + \tilde{\tau}/T_s]|^2 + \sum_{m=(K-1)M}^{KM-1} |r[m + M + \tilde{\tau}/T_s]|^2. \quad (12)$$

The derived joint CFO and FTD estimator operates in the time domain, that is before the SFB, and has the following characteristics:

- 1) it does not require the knowledge of the channel impulse response and of the SNR;
- 2) the LS CFO estimator in (10), provides a closed form solution for the CFO estimate and can assure unambiguous CFO estimates if  $|\varepsilon| < 1/2$ ;
- 3) it exploits the transmission of a short preamble composed by two identical FBMC symbols or, alternatively, only one FBMC symbol with two identical parts. Therefore, it can be successfully used in a downlink WiMAX-like context.

The developed method exploits the transmission of a preamble composed by 2 identical FBMC symbols, therefore it is characterized by a latency of about  $K-1$  FBMC symbols, this latency can be avoided if preloading techniques are considered. Moreover its complexity is essentially due to the FTD estimator that requires a maximization procedure with respect to the parameter  $\tau$ .

### 3.2.2 ML Estimator

In this section we derive the joint ML phase offset, CFO and symbol timing estimator for FBMC systems exploiting the transmission of a known training sequence. In particular, let us consider a preamble of  $N_{TR}$  FBMC symbols, as shown in Fig.3-2, given by

$$z[m] = \sum_{k \in M_u} \sum_{n=0}^{2N_{TR}-1} d_{k,n} \theta_{k,n} \beta_{k,n} p[m - nM/2] e^{j \frac{2\pi}{M} kn} \quad (13)$$

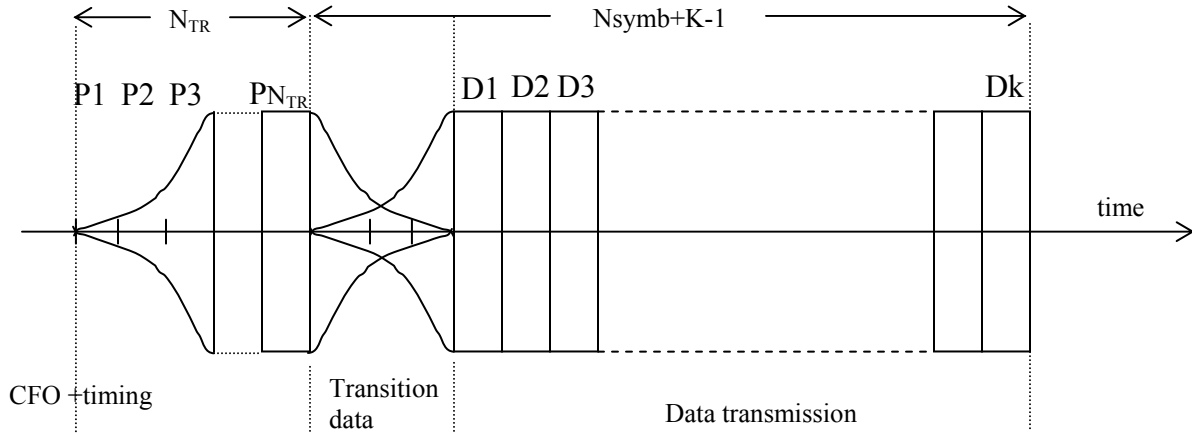


Figure 3-2 Structure of the burst for ML estimation

The received signal in AWGN channel, when the information-bearing signal  $s[m]$  presents a timing offset  $\tau$ , a CFO  $\varepsilon$ , a carrier phase offset  $\phi$  and an attenuation  $|c|$ , can be expressed as

$$r[m] = e^{j2\pi \left[ \frac{m\varepsilon}{M} + \phi \right]} |c| s[m - \tau/T_s] + \eta[m]. \quad (14)$$

By considering an observations window of length  $M\eta$  samples containing the non-zero support of the received preamble, the likelihood function in AWGN channel for the unknown parameters  $\{\tau, \varepsilon, \phi\}$  is given by (up to an irrelevant multiplicative factor)

$$\Lambda(\tilde{\tau}, \tilde{\varepsilon}, \tilde{\phi}) = \exp \left\{ -\frac{T_s}{N_0} \sum_{m=0}^{\eta M-1} \left| r[m] - |c| e^{j2\pi \left( \frac{\tilde{\varepsilon}m}{M} + \tilde{\phi} \right)} \tilde{z}[m - \tilde{\tau}/T_s] \right|^2 \right\}. \quad (15)$$

By replacing (13) in (15) and dropping irrelevant multiplicative and additive factors we get

$$\ln \Lambda(\tilde{\tau}, \tilde{\varepsilon}, \tilde{\phi}) = \text{Re} \left[ |c| e^{-j2\pi \tilde{\phi}} \gamma(\tilde{\tau}, \tilde{\varepsilon}) \right] \quad (16)$$

where

$$\gamma(\tilde{\tau}, \tilde{\varepsilon}) = \sum_{m=0}^{\eta M-1} r[m] \tilde{z}[m - \tilde{\tau}/T_s]^* e^{-j \frac{2\pi \tilde{\varepsilon}}{M} m}. \quad (17)$$

In particular, in the derivation of (16), we have neglected the quantity

$$\sum_{m=0}^{\eta M-1} \|c\| \tilde{z}_i[m - \tilde{\tau}/T_s]^2 \quad (18)$$

independent of the phase offset and the CFO, and slightly dependent of the symbol timing. Therefore, for a given value of the parameters  $\{\tilde{\tau}, \tilde{\varepsilon}\}$  the ML estimator of  $\tilde{\phi}$  is equal to

$$\hat{\phi}_{ML}(\tilde{\varepsilon}, \tilde{\tau}) = \frac{1}{2\pi} \angle \{ \gamma(\tilde{\varepsilon}, \tilde{\tau}) \} \quad (19)$$

and, moreover,

$$(\hat{\tau}_{ML}, \hat{\varepsilon}_{ML}) = \arg \max_{(\tilde{\tau}, \tilde{\varepsilon})} [|\gamma(\tilde{\varepsilon}, \tilde{\tau})|]. \quad (20)$$

Note that the solution of the considered two-dimensional maximization problem can be found only by numerical methods. Therefore, due to the computational complexity of the joint ML estimator, we consider a more feasible synchronization scheme that requires two one-dimensional maximization procedures. Precisely, let us suppose that the CFO is sufficiently small that within a time  $\Delta Q$  comparable with the length of the prototype filter it results that  $e^{-j \frac{2\pi}{M} \tilde{\varepsilon} \Delta Q} \approx 1$ , into the case of a training sequence of total length  $N_{TR} = 1$  it follows that

$$\begin{aligned} & \sum_{m=0}^{\eta M-1} r[m] \tilde{z}[m - \tilde{\tau}/T_s]^* e^{-j \frac{2\pi \tilde{\varepsilon}}{M} m} \\ &= \sum_{n=0}^1 \sum_{k \in M_u} d_{k,n} (\theta_{k,n} \beta_{k,n})^* \underbrace{\sum_{m=0}^{\eta M-1} r[m] p[m - nM/2 - \tilde{\tau}/T_s] e^{j \frac{2\pi}{T} k(\tilde{\tau}-m)} e^{-j \frac{2\pi \tilde{\varepsilon}}{M} m}}_{w_n^{(k)}(\tilde{\varepsilon}, \tilde{\tau})} \\ &\approx \sum_{n=0}^1 \sum_{k \in M_u} d_{k,n} (\theta_{k,n} \beta_{k,n})^* w_n^{(k)}(0, \tilde{\tau}) e^{-j \pi \tilde{\varepsilon} n} \end{aligned} \quad (21)$$

then

$$\gamma(\tilde{\varepsilon}, \tilde{\tau}) = \underbrace{\sum_{k \in M_u} d_{k,0} \theta_{k,0}^* \beta_{k,0}^* w_0^{(k)}(0, \tilde{\tau})}_{A(\tilde{\tau})} + e^{-j\pi\tilde{\varepsilon}} \underbrace{\sum_{k \in M_u} d_{k,1} \theta_{k,1}^* \beta_{k,1}^* w_1^{(k)}(0, \tilde{\tau})}_{B(\tilde{\tau})}. \quad (22)$$

Therefore, the joint ML estimator in (20) can be simplified as

$$\hat{\tau}_{AML} = \arg \max_{\tilde{\tau}} [|A(\tilde{\tau})| + |B(\tilde{\tau})|]. \quad (23)$$

and

$$\hat{\varepsilon}_{AML}(\hat{\tau}_{AML}) = \frac{1}{\pi} \angle \{ A^*(\hat{\tau}_{AML}) B(\hat{\tau}_{AML}) \}. \quad (24)$$

The derived joint AML symbol timing and CFO estimator in (23) and (24) results to be particularly attractive since, differently from the joint ML estimator considered in (20), provides a closed form solution for the CFO estimate and, then, it requires only a one-dimensional maximization with respect to the parameter  $\tilde{\tau}$ .

In the case of perfect CFO synchronization, by following the same steps as before, we obtain that the joint ML symbol timing and phase offset estimator is given by

$$\hat{\tau}_{ML} = \arg \max_{\tilde{\tau}} \left[ \left| \sum_{k=0}^{\eta M-1} r[k] z[k - \tilde{\tau} / T_s]^* \right| \right] \quad (25)$$

and, moreover,

$$\hat{\phi}_{ML}(\hat{\tau}_{ML}) = \frac{1}{2\pi} \angle \left\{ \sum_{k=0}^{\eta M-1} r[k] z[k - \hat{\tau}_{ML} / T_s]^* \right\}. \quad (26)$$

Analogously, into the case of perfect symbol timing synchronization, the joint ML CFO and phase offset estimator is given by

$$\hat{\varepsilon}_{ML} = \arg \max_{\tilde{\varepsilon}} \left[ \left| \sum_{k=0}^{\eta M-1} r[k] z[k]^* e^{-j\frac{2\pi}{M}\tilde{\varepsilon}k} \right| \right] \quad (27)$$

and

$$\hat{\phi}_{ML}(\hat{\varepsilon}_{ML}) = \frac{1}{2\pi} \angle \left\{ \sum_{k=0}^{\eta M-1} r[k] z[k]^* e^{-j\frac{2\pi}{M}\hat{\varepsilon}_{ML}k} \right\} \quad (28)$$

Advantages, complexity and latency of the joint AML estimator proposed in (23) and (24) can be summarized as follows:

- 1) it does not require the knowledge of the channel impulse response and of the SNR. Its performance is improved with respect to the LS estimator but it is sensitive to the channel response because it exploits a training sequence;
- 2) the AML CFO estimator in (24), provides a closed form solution for the CFO estimate and can assure unambiguous CFO estimates if  $|\varepsilon| < 1$ ;
- 3) it exploits the knowledge of a training sequence composed by  $N_{TR}$  FBMC symbols. As demonstrated in the numerical results shown in the following it can assure accurate estimates also when the preamble is composed by only one FBMC symbol;

- 4) as demonstrated in Section 4.1.2 the proposed estimator can be successfully exploited in an uplink scenario;
- 5) it has a latency of about  $N_{TR}$  FBMC-OQAM symbols;
- 6) finally, its complexity is very similar to that of the joint LS symbol timing and CFO estimator derived in the section 3.2.1. That is the AML CFO estimator presents a closed form solution while the symbol timing estimator requires a maximization procedure.

### 3.2.3 Performance Evaluation of Preamble-Based Estimators

In this section the performance of the derived joint LS and AML estimators reported in (9), (10), (23) and (24) is assessed via computer simulations. In the numerical results we have also considered the ML-based synchronization algorithm

$$\hat{\tau}_{ML} = \arg \max_{\tilde{\tau}} \left[ \sum_{k=0}^{\eta M - 1} r[k] z[k - \tilde{\tau} / T_s]^* \right] \quad (29)$$

$$\hat{\varepsilon}_{ML} = \arg \max_{\tilde{\varepsilon}} \left[ \sum_{k=0}^{\eta M - 1} r[k + \hat{\tau}_{ML} / T_s] z[k]^* e^{-j \frac{2\pi}{M} \tilde{\varepsilon} k} \right] \quad (30)$$

obtained by exploiting at first the symbol timing ML estimator (25) and successively the CFO ML estimator (27).

A number of  $10^3$  Monte Carlo trials has been performed under the following conditions:

- The value of the normalized CFO and of the timing offset are uniformly distributed in  $[-0.25, 0.25)$  and  $T_s\{-M/2, -M/2+1, \dots, M/2-1, M/2\}$ , respectively. In particular, the symbol timing is supposed to be an integer multiple of the sampling period  $T_s$ .
- The size of the set of subcarriers is  $M=1024$ .
- The joint LS CFO and symbol timing estimator exploits a preamble made up of two identical FBMC symbols. Moreover, preloading techniques are used to avoid the transient.
- The considered joint AML and ML-based estimators exploit a preamble made up of only one FBMC symbol.
- The prototype filter is that described in [4] with an overlapping factor  $K=4$ .
- Numerical results have been obtained by considering two different scenarios using 4-QAM constellation: AWGN channel and multipath channel modelled using the Vehicular-A channel model of ITU-R. Moreover, the channel is fixed in each run but it is independent from one run to another.

Figure 3-3 and Figure 3-4 show the RMSE of the considered joint symbol timing and CFO estimators in AWGN (solid lines) and multipath channel (dashed lines) as a function of the SNR. In Figure 3-4 we have included the Cramér-Rao bound for CFO estimation derived in [3].

The results show that in multipath channel the proposed AML and ML symbol timing estimators exhibit a significant performance degradation with respect to the AWGN case while the considered CFO estimators assure nearly the same RMSE. In particular, from Figure 3-4 we can note that the proposed LS CFO estimator provides in AWGN channel a performance very close to the bound, it assures performance gain with respect to the ML-based and the AML techniques, and, moreover, it does not present a floor also in multipath channel.

Figure 3-5 illustrates the BER in AWGN and multipath channel obtained by exploiting the derived joint CFO and symbol timing estimators. In the figure it is also reported the BER of the considered FBMC system into the case of perfect synchronization. It is assumed that on each subchannel it is exploited a one-tap equalizer with perfect knowledge of the channel and, of the symbol timing and the CFO. As shown in Figure 3-5 in AWGN the ML-based estimators assure the best performance while in multipath channel the ML-based, the AML and the much more simple LS estimators provide a BER very close to that obtained in the case of perfect synchronization.

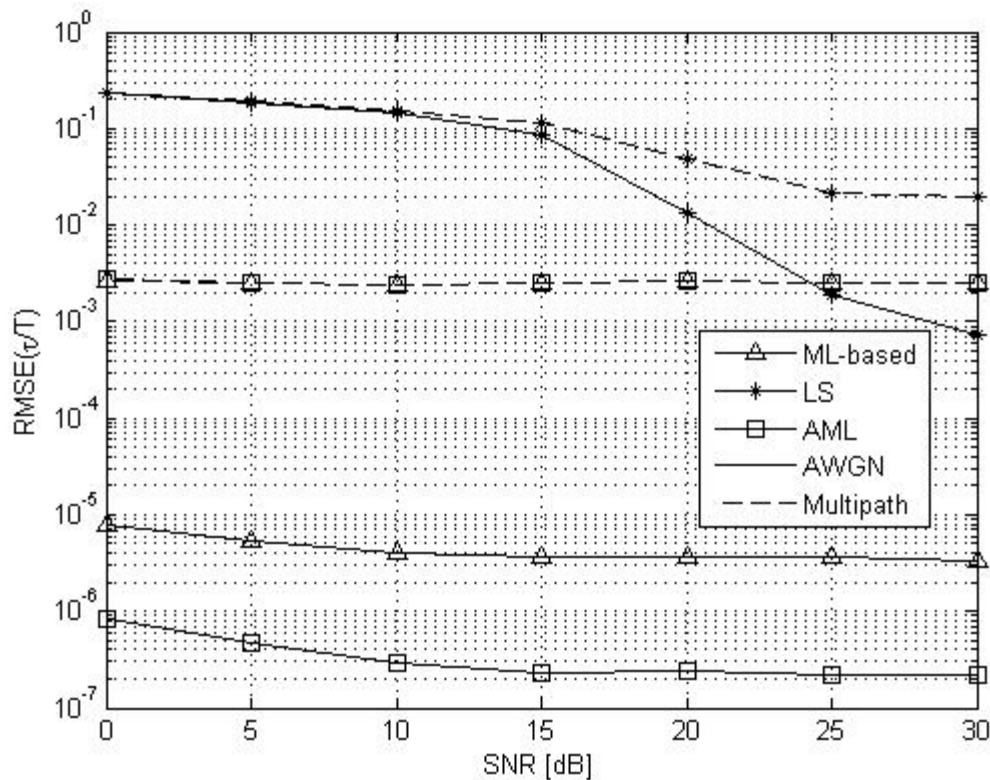


Figure 3-1. RMSE of the considered symbol timing estimators as a function of the SNR in AWGN (solid lines) and multipath channel (dashed lines).

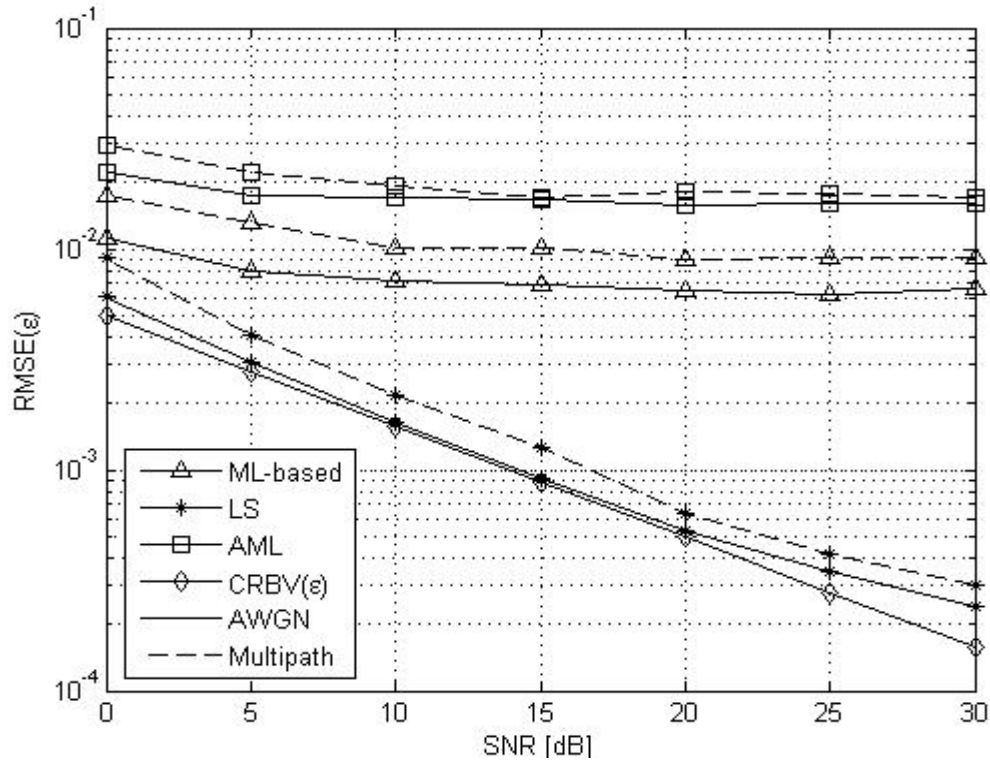


Figure 3-2. RMSE of the considered CFO estimators as a function of the SNR in AWGN (solid lines) and multipath channel (dashed lines).

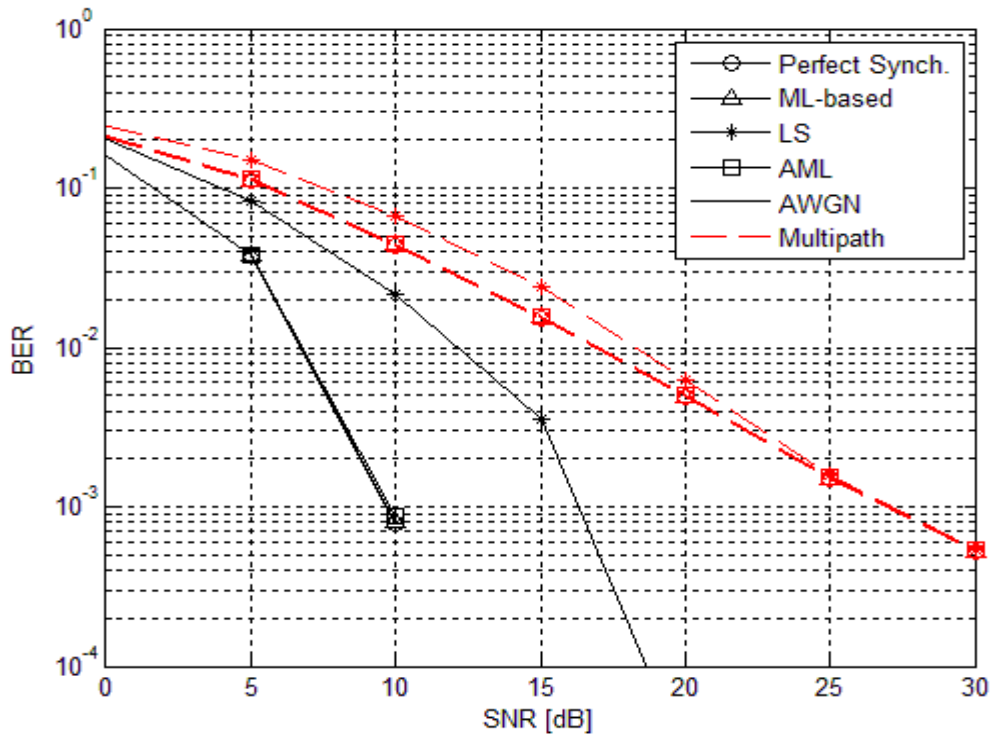


Figure 3-3. BER of the considered estimators as a function of the SNR in AWGN (solid lines) and multipath channel (dashed lines).

### 3.2.4 Comparison with OFDM Systems

In this section we evaluate the performance of a joint symbol timing and CFO estimation algorithm exploited for OFDM systems.

Precisely, in this case the training sequence is made up of two identical parts, obtained by transmitting pseudonoise data symbols on the subcarriers with even indices and setting zero on the remaining subcarriers. In this way, we obtain the training sequence

$$s_{TR}[m] = \sum_{l \in M_u} a_l^{TR} e^{jl \frac{2\pi}{M} m} \quad (31)$$

made up of two identical parts, that is,

$$s_{TR}[m] = s_{TR}[m + M / 2]. \quad (32)$$

Accounting for the redundancy of the training sequence a joint symbol timing and CFO estimator can be obtained by considering the minimization problem

$$(\hat{\varepsilon}_0, \hat{\tau}_0) = \arg \min_{(\tilde{\varepsilon}_0, \tilde{\tau}_0)} \left\{ \sum_{m=0}^{M/2-1} \left| r[m + \tilde{\tau}_0 / T_s] - r[m + M / 2 + \tilde{\tau}_0 / T_s] e^{-j\pi \tilde{\varepsilon}_0} \right|^2 \right\}. \quad (33)$$

The minimization in (33) leads to the following joint CFO and symbol timing estimator

$$\hat{\tau} = \arg \max_{\tilde{\tau}_0} \left\{ 2|U(\tilde{\tau}_0)| - V(\tilde{\tau}_0) \right\} \quad (34)$$

and

$$\hat{\varepsilon}(\hat{\tau}) = \frac{1}{\pi} \angle \{U(\hat{\tau})\} \quad (35)$$

with

$$U(\tilde{\tau}_0) = \sum_{m=0}^{M/2-1} r^*[m + \tilde{\tau}_0 / T_s] r[m + M / 2 + \tilde{\tau}_0 / T_s] \quad (36)$$

and

$$V(\tilde{\tau}_0) = \sum_{m=0}^{M/2-1} |r[m + \tilde{\tau}_0 / T_s]|^2 + \sum_{k=0}^{M/2-1} |r[m + M / 2 + \tilde{\tau}_0 / T_s]|^2. \quad (37)$$

Let us observe that if we divide the timing metric in (34) by  $V(\tilde{\tau}_0)$  we obtain a joint symbol timing and CFO estimator similar to that derived in [2] by Schmidt and Cox and referred in the following to as modified Schmidl and Cox estimator

$$\hat{\tau}_{SC} = \arg \max_{\tilde{\tau}_0} \left\{ \frac{2|U(\tilde{\tau}_0)|}{V(\tilde{\tau}_0)} \right\} \quad (38)$$

and

$$\hat{\varepsilon}_{SC}(\hat{\tau}_{SC}) = \frac{1}{\pi} \angle \{U(\hat{\tau}_{SC})\}. \quad (39)$$



In the following the performance of the considered estimator is assessed via numerical simulations and compared with that of the LS estimator proposed in 3.2.1 and obtained by considering a preamble with two identical parts.

In particular, a number of  $10^3$  Monte Carlo trials are performed under the following conditions:

- the value of the normalized CFO and of the timing offset are uniformly distributed in  $[-0.5, 0.5]$  and  $T_s\{-M/2, -M/2+1, \dots, M/2-1, M/2\}$ ;
- the size of the set of subcarriers for the considered OFDM system is  $M=1024$  while the cyclic prefix length is  $CP=M/16$ ;
- the OFDM training symbol has two identical parts each of length  $M/2=512$ , while the FBMC training symbol with two identical parts is obtained by applying  $K$  identical preamble symbols, with pseudonoise data only on even subcarriers, at the input of the IFFT in the transmitter;
- the multipath channel has been modelled using the Vehicular-A channel model of ITU-R.

In Figure 3-6 and Figure 3-7 is shown the performance of the considered joint SC and LS symbol timing and CFO estimators as a function of  $E_b/N_0$  in AWGN (solid lines) and multipath channel (dashed lines). The results show that the LS estimator outperforms the SC estimator when  $E_b/N_0$  is sufficiently high. In Figure 3-8 it is reported the BER of the considered CFO and symbol timing estimators. Moreover, the BER obtained in the case of perfect synchronization is considered. As indicated in the figure for moderate and high SNR values, the BER obtained by exploiting the proposed LS estimator for FBMC systems and the SC estimator for OFDM systems is nearly coincident with that obtained in the case of perfect synchronization.

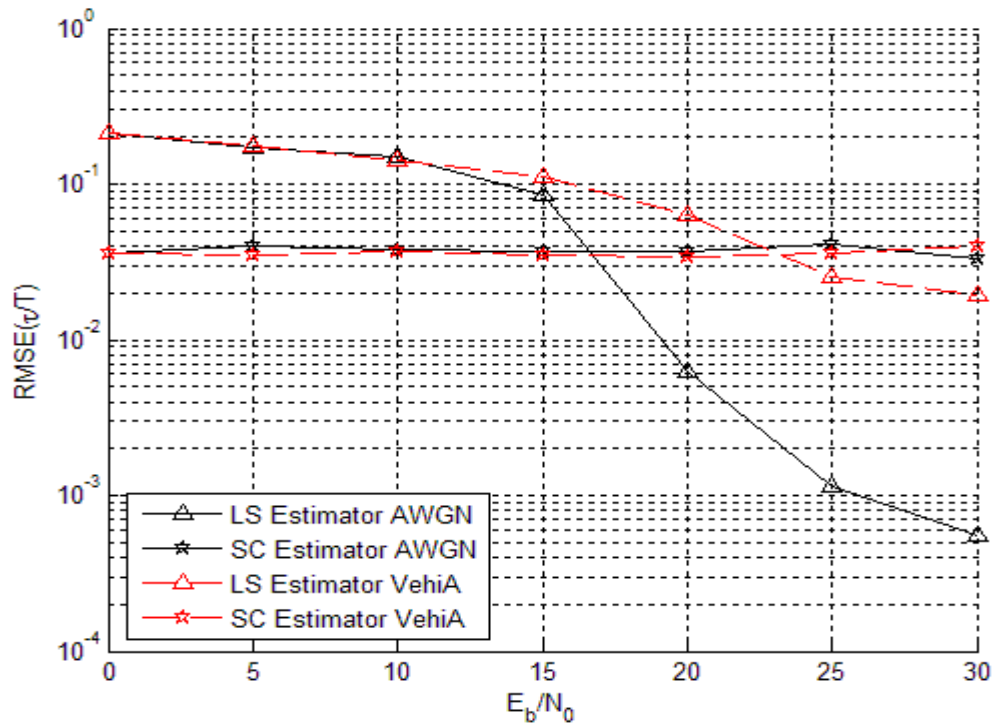


Figure 3-4. Performance of the considered SC and LS symbol timing estimators in AWGN (solid lines) and multipath channel (dashed lines).

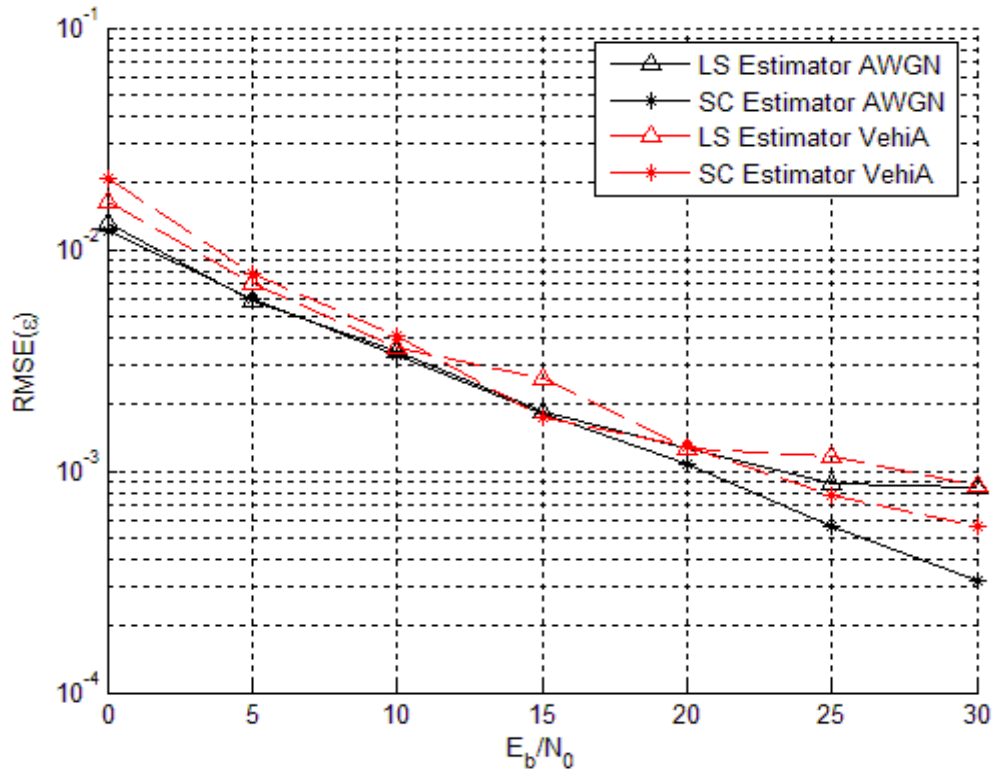


Figure 3-5. Performance of the considered SC and LS CFO estimator in AWGN (solid lines) and multipath channel (dashed lines).

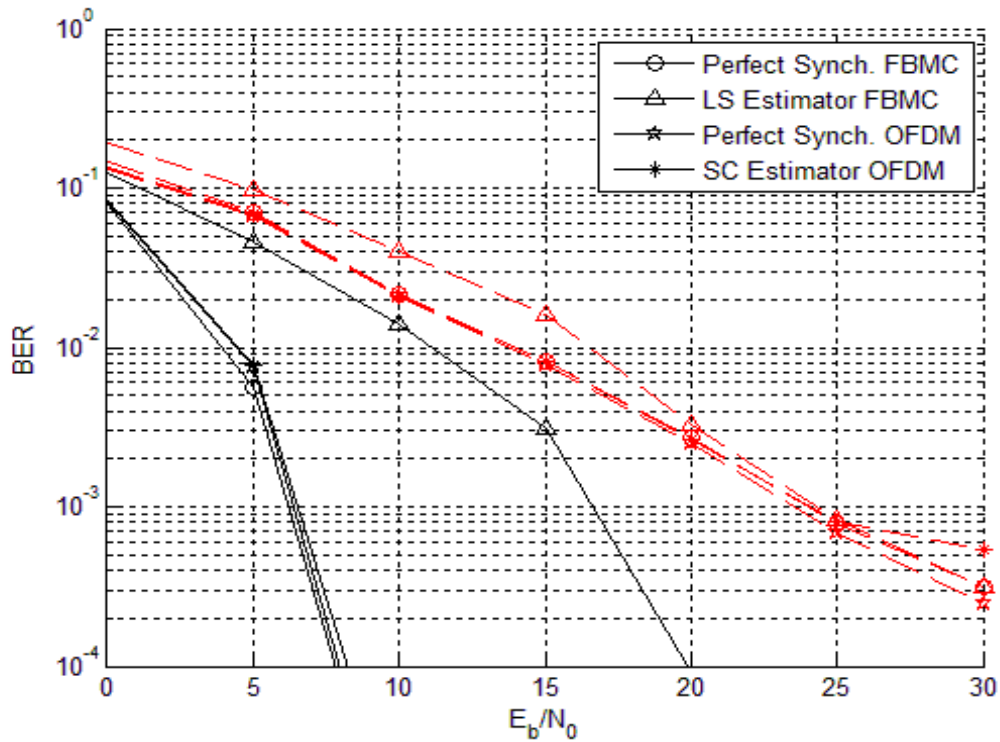


Figure 3-6. Performance of the considered SC and LS estimators in AWGN (solid lines) and multipath channel (dashed lines).

### 3.3 Blind Synchronization

In some situations, particularly for small groups of sub-channels or a single sub-channel, the use of training sequences can involve a significant overhead, leading to a spectral efficiency reduction, thus non data-aided (or blind) techniques must be studied and contrasted with data-aided schemes.

In this section we derive blind estimators for FBMC systems based on the ML principle, and under the assumptions of low SNR and AWGN channel. In particular, in the Subsection 3.3.2 the joint ML phase offset and CFO estimator is derived while in the Subsection 3.3.4 the joint ML phase offset and FTD estimator is considered. The proposed estimators exploit the cyclostationarity of the FBMC signal that is related to the bandwidth of the adopted pulse-shaping filter. In particular, if the adopted pulse-shaping filter pulse-shaping filter is bandlimited within  $[-1/T, 1/T]$  the FBMC signal results to be stationary with respect to its unconjugate correlation function and, then, the ML symbol timing cost function depends only on the conjugate correlation function, while the proposed CFO estimators can exploit both the conjugate and the unconjugate cyclostationarity properties of the received FBMC-OQAM signal.

#### 3.3.1 Cyclostationarity properties of the FBMC Signal

Let us consider an FBMC system with  $M$  subcarriers, the discrete-time received signal in AWGN channel, in the presence of a CFO normalized to the intercarrier spacing  $\varepsilon$ , a carrier phase offset  $\phi$  and an FTD  $\tau$  can be written as

$$r[k] = s[k - \tau / T_s] e^{j\left(\frac{2\pi\varepsilon}{M}k + 2\pi\phi\right)} + \eta[k] \quad (40)$$

where  $s[k]$  is the transmitted FBMC signal and  $\eta[k]$  denotes the zero-mean circular complex white Gaussian noise statistically independent of  $s[k]$ . The signal  $s[k]$  is equal to

$$s[k] = \sum_{l \in \mathcal{M}_u} \sum_{n=-\infty}^{\infty} d_{l,n} \theta_{l,n} p[k - nM / 2] e^{j\frac{2\pi}{M}l\left(k - n\frac{M}{2} - \frac{L_p - 1}{2}\right)} \quad (41)$$

In (41) the sequence  $d_{l,n}$  denotes the real data symbols transmitted on the  $l$ th subcarrier during the  $n$ th FBMC symbol while  $p[k]$  is the real transmitted pulse-shaping filter. In the following we assume that

**(AS1)** The data symbols  $\{d_{l,n}\}_{n=-\infty}^{\infty}$ ,  $\forall l \in \mathcal{M}_u$ , belonging to a PAM constellation, are statistically independent and identically distributed random variables with zero mean, and  $E[(d_{l,n})^2] = 1$ .

**(AS2)** The real-valued and unit-energy pulse-shaping filter  $p[k]$  is bandlimited within  $[-1/M, 1/M]$ .

From the assumptions (AS1) and (AS2) we can easily derive the following results:

*Result 1:* The unconjugate correlation function of the transmitted FBMC signal  $s[k]$  at time  $k$  and lag  $m$  is equal to

$$\begin{aligned} R_s(k; m) &= E[s^*[k]s[k+m]] = \sum_{l \in \mathcal{M}_u} e^{j\frac{2\pi}{M}lm} \sum_{n=-\infty}^{\infty} p\left[k - \frac{nM}{2}\right] p\left[k+m - \frac{nM}{2}\right] \\ &= \frac{2}{M} \sum_{l \in \mathcal{M}_u} e^{j\frac{2\pi}{M}lm} \int_{-1/2}^{1/2} |P(\nu)|^2 e^{-j2\pi\nu m} d\nu \end{aligned} \quad (42)$$

where the last equality follows from the assumption (AS2) on the pulse shaping filter, and, moreover

$$P(v) = \sum_{k=-\infty}^{\infty} p[k] e^{-j2\pi kv} \quad (43)$$

is the DFT of the real pulse shaping filter  $p[k]$ .

*Result 2:* The relation function (or the conjugate correlation function) of the transmitted signal  $s[k]$  is given by

$$C_s(k; m) = E[s[k]s[k+m]] = \sum_{l \in \mathcal{M}_u} e^{j\frac{2\pi}{M}l(2k+m)} \sum_{n=-\infty}^{\infty} (\theta_{n,l} \beta_{n,l})^2 p\left[k - \frac{nM}{2}\right] p\left[k+m - \frac{nM}{2}\right] \quad (44)$$

From result 1 we can deduce that under the assumption (AS2) on the pulse shaping filter the FBMC signal is stationary with respect to its unconjugate correlation function. On the other hand, from result 2 we can note that the conjugate correlation function results to be conjugate second-order cyclostationary with period  $M$ .

In the absence of virtual subcarriers (that is for  $M = M_u$ ) the unconjugate correlation function of the transmitted FBMC signal  $s[k]$  at time  $k$  and lag  $m$  is equal to (see [5])

$$R_s(k; m) = M \delta(m - \gamma M) \sum_{n=-\infty}^{\infty} p\left[k - \frac{nM}{2}\right] p\left[k+m - \frac{nM}{2}\right] = 2\delta(m). \quad (45)$$

Moreover, the conjugate correlation function results to be

$$C_s(k; m) = E[s[k]s[k+m]] = M \sum_{l=0}^{M-1} e^{j\frac{2\pi}{M}l(2k+m)} \sum_{n=-\infty}^{\infty} (\theta_{n,l} \beta_{n,l})^2 p\left[k - \frac{nM}{2}\right] p\left[k+m - \frac{nM}{2}\right]. \quad (46)$$

In the following, the unconjugate and the conjugate cyclostationarity properties of the FBMC signal are exploited to derive blind synchronization algorithms for CFO and FTD estimation.

### 3.3.2 Blind ML CFO Synchronization

In this section we derive three ML CFO estimators for FBMC systems under the assumption of low SNR conditions and perfect FTD estimation, see [5]. Precisely, let us consider an observations window of length  $M\eta$  samples, the likelihood function in AWGN channel, for the transmitted symbol sequence  $\underline{d} = \{d_{l,n}; l \in \mathcal{M}_u, n \in \mathbb{Z}\}$  and for the two unknown parameters  $\varepsilon$  and  $\phi$  is given by (up to an irrelevant multiplicative factor)

$$\Lambda(\underline{d}, \tilde{\varepsilon}, \tilde{\phi}) = \exp \left\{ -\frac{T_s}{N_0} \sum_{k=0}^{M\eta-1} \left| r[k] - e^{j2\pi\tilde{\phi}} e^{j\frac{2\pi\tilde{\varepsilon}}{M}k} \tilde{s}[k] \right|^2 \right\} \quad (47)$$

where  $r[k] = s[k] e^{j\frac{2\pi\varepsilon}{M}k} e^{j2\pi\phi} + \eta[k]$  is the received signal,

$$\tilde{s}[k] = \sum_{l \in \Omega_u} \sum_{n=-\infty}^{\infty} \tilde{d}_{l,n} \theta_{l,n} \beta_{l,n} p[k - nM/2] e^{j \frac{2\pi}{M} l k} \quad (48)$$

is the transmitted FBMC signal. Replacing (48) in (47) and dropping factors independent of the unknown parameters we get

$$\Lambda(\tilde{\underline{d}}, \tilde{\varepsilon}, \tilde{\phi}) = \exp \left\{ \frac{2T_s}{N_0} \operatorname{Re} \left[ e^{-j2\pi\tilde{\phi}} \sum_{k=0}^{\eta M-1} r[k] \underbrace{\left( \tilde{s}[k] e^{j \frac{2\pi\tilde{\varepsilon}}{M} k} \right)^*}_{\tilde{s}^{\tilde{\varepsilon}}[k]} \right] \right\}. \quad (49)$$

By developing in series the likelihood function until the second-order we obtain

$$\Lambda(\tilde{\underline{d}}, \tilde{\varepsilon}, \tilde{\phi}) = 1 + \frac{2T_s}{N_0} \operatorname{Re} \left[ e^{-j2\pi\tilde{\phi}} \sum_{k=0}^{\eta M-1} r[k] \tilde{s}^{\tilde{\varepsilon}}[k]^* \right] + \frac{1}{2} \left( \frac{2T_s}{N_0} \operatorname{Re} \left[ e^{-j2\pi\tilde{\phi}} \sum_{k=0}^{\eta M-1} r[k] \tilde{s}^{\tilde{\varepsilon}}[k]^* \right] \right)^2. \quad (50)$$

Moreover, by averaging the function (50) with respect to the data symbols and under the assumption AS1, we obtain the marginal likelihood function

$$\begin{aligned} \Lambda(\tilde{\varepsilon}, \tilde{\phi}) &= E \left[ \Lambda(\tilde{\underline{d}}, \tilde{\varepsilon}, \tilde{\phi}) \right] \\ &= 1 + \frac{T_s^2}{N_0^2} \operatorname{Re} \left[ e^{-j4\pi\tilde{\phi}} \sum_{k_1=0}^{\eta M-1} \sum_{k_2=0}^{\eta M-1} (r[k_1] r[k_2])^* E \left[ \tilde{s}^{\tilde{\varepsilon}}[k_1] \tilde{s}^{\tilde{\varepsilon}}[k_2] \right] \right] + \frac{T_s^2}{N_0^2} \sum_{k_1=0}^{\eta M-1} \sum_{k_2=0}^{\eta M-1} r[k_1] r[k_2]^* E \left[ \tilde{s}^{\tilde{\varepsilon}}[k_1] \tilde{s}^{\tilde{\varepsilon}}[k_2]^* \right]. \end{aligned} \quad (51)$$

The joint ML estimator is obtained by searching the values of the parameters  $\varepsilon$  and  $\phi$  that maximize the likelihood function (51). To proceed we keep the parameter  $\varepsilon$  fixed and let  $\phi$  vary. Under these conditions the function  $\Lambda(\tilde{\varepsilon}, \tilde{\phi})$  in (51) achieves a maximum for

$$\hat{\phi}_{ML} = \frac{1}{4\pi} \angle \left\{ \sum_{k_1=0}^{\eta M-1} \sum_{k_2=0}^{\eta M-1} (r[k_1] r[k_2])^* E \left[ \tilde{s}^{\tilde{\varepsilon}}[k_1] \tilde{s}^{\tilde{\varepsilon}}[k_2] \right] \right\}. \quad (52)$$

Hence, accounting for (51) and (52), the ML CFO estimator for low SNR values (MLLS) is given by

$$\hat{\varepsilon}_{MLLS} = \arg \max_{\tilde{\varepsilon}} \left\{ \left| \sum_{k_1=0}^{\eta M-1} \sum_{k_2=0}^{\eta M-1} (r[k_1] r[k_2])^* E \left[ \tilde{s}^{\tilde{\varepsilon}}[k_1] \tilde{s}^{\tilde{\varepsilon}}[k_2] \right] \right| + \sum_{k_1=0}^{\eta M-1} \sum_{k_2=0}^{\eta M-1} r[k_1] r[k_2]^* E \left[ \tilde{s}^{\tilde{\varepsilon}}[k_1] \tilde{s}^{\tilde{\varepsilon}}[k_2]^* \right] \right\}. \quad (53)$$

Note that if we consider the carrier phase as a random nuisance parameter uniformly distributed in  $[0, 1)$  and average (51) with respect to  $\phi$  we obtain

$$\Lambda(\tilde{\varepsilon}, \tilde{\underline{d}}) = \int_0^1 \Lambda(\tilde{\varepsilon}, \tilde{\phi}, \tilde{\underline{d}}) d\tilde{\phi} = I_0(|\mu|) \quad (54)$$

where  $\mu = \frac{2T_s}{N_0} \operatorname{Re} \left[ \sum_{k=0}^{\eta M-1} r[k] \tilde{s}^{\tilde{\varepsilon}}[k]^* \right]$  and  $I_0(\cdot)$  is the modified Bessel function of the first kind and order zero. Under the assumption of low SNR values the Bessel function can be approximated as

$$I_0(|\mu|) \cong 1 + \frac{|\mu|^2}{4}. \quad (55)$$

Moreover, by averaging the function (51) with respect to the data symbols and neglecting additive and multiplicative parameters independent of the CFO  $\tilde{\varepsilon}$ , we obtain

$$\Lambda(\tilde{\varepsilon}) = \sum_{k_1=0}^{\eta M-1} \sum_{k_2=0}^{\eta M-1} r[k_1]r[k_2]^* E[\tilde{s}^{\tilde{\varepsilon}}[k_1]\tilde{s}^{\tilde{\varepsilon}}[k_1]^*] \quad (56)$$

and the corresponding blind ML CFO estimator is given by

$$\hat{\varepsilon}_{UMLLS} = \arg \max_{\tilde{\varepsilon}} \left\{ \sum_{k_1=0}^{\eta M-1} \sum_{k_2=0}^{\eta M-1} r[k_1]r[k_2]^* E[\tilde{s}^{\tilde{\varepsilon}}[k_1]\tilde{s}^{\tilde{\varepsilon}}[k_1]^*] \right\}. \quad (57)$$

Thus, the ML estimator in (57) is coincident with the second term of the cost function in (51), depending on the unconjugate correlation function. Therefore, it is referred to as unconjugate MLLS estimator (UMLLS estimator). However, as demonstrated in [5], it cannot be used in the case of a fully loaded FBMC system ( $M_v = 0$ ). If we do not consider the second term of the cost function in (51), depending on the unconjugate correlation function, we obtain the CFO estimator

$$\hat{\varepsilon}_{CMLLS} = \arg \max_{\tilde{\varepsilon}} \left\{ \left| \sum_{k_1=0}^{\eta M-1} \sum_{k_2=0}^{\eta M-1} r[k_1]^* r[k_2] E[\tilde{s}^{\tilde{\varepsilon}}[k_1]\tilde{s}^{\tilde{\varepsilon}}[k_1]] \right| \right\}. \quad (58)$$

In the case of a fully loaded FBMC system the CFO estimator in (58), exploiting the conjugate correlation function of the FBMC signal, is coincident with the ML estimator for low SNR, then in the following it will be referred to as conjugate MLLS estimator (CMLLS estimator).

### 3.3.3 Simplified CFO Synchronization

Let us consider the following statistics

$$\hat{R}(m) = \frac{1}{M-m} \sum_{k=0}^{M-m-1} r^*[k]r[k+m] \quad (59)$$

and

$$\hat{R}(M-m) = \frac{1}{m} \sum_{k=0}^{m-1} r^*[k]r[k+M-m]. \quad (60)$$

Under the assumptions (AS1) and (AS2), for  $1 \leq m \leq M-1$  it follows that

$$\hat{R}(m) = e^{j\frac{2\pi\tilde{\varepsilon}}{M}m} z(m) \sum_{l \in \mathcal{M}_u} e^{j\frac{2\pi}{M}ml} + e_1(m) \quad (61)$$

where

$$e_1(m) = \hat{R}(m) - E[\hat{R}(m)] \quad (62)$$

and

$$z(m) = \frac{2}{M} \int_{-1/2}^{1/2} |P(v)|^2 e^{-j2\pi vm} dv \quad (63)$$

is a real function since  $|P(\nu)| = \left| \sum_{k=-\infty}^{\infty} g[k] e^{j2\pi k\nu} \right|$  is an even function.

Moreover, for  $1 \leq m \leq M-1$ , we have

$$\hat{R}(M-m) = e^{j\frac{2\pi\epsilon}{M}(M-m)} z(M-m) \sum_{l \in \mathcal{M}_u} e^{-j\frac{2\pi}{M}ml} + e_2(m) \quad (64)$$

where

$$e_2(m) = \hat{R}(M-m) - E[\hat{R}(M-m)]. \quad (65)$$

It is shown in [5] that, under the assumptions (AS1)-(AS2), the zero-mean "noise" terms in (62) and (65) have a variance  $\mathcal{O}((N-m)^{-1})$  and  $\mathcal{O}(m^{-1})$ , respectively. Moreover, if for the considered pulse-shaping filter  $p[k]$  and for  $1 \leq m \leq M-1$ ,  $z(m)z(M-m) > 0$ , taking into account (61) and (64) it follows that a CFO estimate can be obtained by minimizing the norm

$$J(\epsilon) = \left| \sum_{m=L_1}^{L_2-1} \hat{R}(m) \hat{R}(M-m) - e^{j2\pi\epsilon} \sum_{m=L_1}^{L_2-1} z(m) z(M-m) \sum_{l \in \mathcal{M}_u} e^{j\frac{2\pi}{N}ml} \right|^2 \quad (66)$$

where  $L_1$  and  $L_2$  are design parameters selected so that the conditions  $N-m \gg 1$  and  $m \gg 1$  are satisfied. The minimization of the least-square error in (66) with respect to  $\epsilon$  leads to the proposed closed-form LS CFO estimator

$$\hat{\epsilon}_{LS} = \frac{1}{2\pi} \angle \left\{ \sum_{m=L_1}^{L_2-1} \hat{R}(m) \hat{R}(N-m) \right\}. \quad (67)$$

It is worthwhile to emphasize that the CFO estimator in (67), whose acquisition range is  $|\epsilon| < 1/2$ , does not require the knowledge of the SNR.

### 3.3.4 Blind ML Symbol Timing Synchronization

In this section we derive the ML symbol timing estimator for FBMC systems with perfect CFO synchronization and under the assumption of low SNR conditions, see [6]. Precisely, the likelihood function in AWGN channel, for the transmitted symbol sequences  $\underline{d} = \{d_{l,n}; l \in M_u, n \in Z\}$ , and for the two unknown parameters  $\tau$  and  $\phi$  is given by

$$\Lambda(\tilde{\tau}, \tilde{\phi}, \tilde{\underline{d}}) = \exp \left\{ -\frac{T_s}{N_0} \sum_{k=0}^{\eta M-1} |r[m] - c| e^{j2\pi\tilde{\phi}} \tilde{s}^*[m] \right\}^2 \quad (68)$$

where  $r[m] = s[m - \tau/T_s] e^{j2\pi\phi} + \eta[m]$  and  $s^*[m] = s^*[m - \tau/T_s]$ . By developing in series the likelihood function until the second-order, by averaging with respect to the data symbols and, accounting for the algebraic manipulations considered in the subsection 3.3.2 we obtain (up to an irrelevant additive term)

$$\Lambda(\tilde{\tau}, \tilde{\phi}) = \frac{|c|^2 T_s^2}{N_0^2} \mathbb{E} \left[ \text{Re} \left\{ \left( e^{-j\tilde{\phi}} \sum_{k=0}^{\eta M-1} r[k] \tilde{s}^{\tilde{\tau}}[k]^* \right)^2 \right\} + \left| \sum_{k=0}^{\eta M-1} r[k] \tilde{s}^{\tilde{\tau}}[k]^* \right|^2 \right]. \quad (69)$$

The joint MLLS estimator is obtained by searching the values of the parameters  $\tau$  and  $\phi$  that maximize the likelihood function in (69). To proceed we keep the parameter  $\tau$  fixed and let  $\phi$  vary. Under these conditions the function  $\Lambda(\tilde{\tau}, \tilde{\phi})$  in (69) achieves a maximum for

$$\hat{\phi}_{MLLS} = \frac{1}{4\pi} \angle \left\{ \sum_{k_1=0}^{\eta M-1} \sum_{k_2=0}^{\eta M-1} r[k_1] r[k_2] \mathbb{E} [\tilde{s}^{\tilde{\tau}}[k_1]^* \tilde{s}^{\tilde{\tau}}[k_2]^*] \right\}. \quad (70)$$

Hence, accounting for (69) and (70), the MLLS symbol timing is given by

$$\hat{\tau}_{MLLS} = \arg \max_{\tilde{\tau}} \left[ uc(\tilde{\tau}) + |c(\tilde{\tau})| \right] \quad (71)$$

where

$$uc(\tilde{\tau}) = \sum_{k_1=0}^{\eta M-1} \sum_{k_2=0}^{\eta M-1} r[k_1] r^*[k_2] \mathbb{E} [\tilde{s}^{\tilde{\tau}}[k_1]^* \tilde{s}^{\tilde{\tau}}[k_2]] \quad (72)$$

and

$$c(\tilde{\tau}) = \sum_{k_1=0}^{\eta M-1} \sum_{k_2=0}^{\eta M-1} r[k_1] r[k_2] \mathbb{E} [\tilde{s}^{\tilde{\tau}}[k_1]^* \tilde{s}^{\tilde{\tau}}[k_2]^*]. \quad (73)$$

Since under the assumption (AS2) on the pulse-shaping filter the transmitted FBMC signal results to be stationary with respect to its unconjugate correlation function, the term  $uc(\tilde{\tau})$  in (71) does not depend on the symbol timing and, then, in this case we obtain

$$\hat{\tau}_{MLLS} = \arg \max_{\tilde{\tau}} [|c(\tilde{\tau})|]. \quad (74)$$

### 3.3.5 Performance Evaluation of CFO Estimators

The performance of the considered MLLS, UMLLS, CMLLS and LS estimators has been assessed via computer simulations by performing a number of  $10^3$  Monte Carlo trials under the following conditions (unless otherwise stated):

- the value of the CFO is uniformly distributed in  $[-0.5, 0.5]$ ;
- the size of the set of subcarriers is  $M=1024$  and the number of virtual subcarriers is  $M_v = 128$ ;
- the prototype filter is that described in [4] with an overlapping factor  $K=4$ ;
- numerical results have been obtained by considering two different scenarios: AWGN channel and multipath channel modelled using the Vehicular-A channel model of ITU-R. Moreover, the channel is fixed in each run but it is independent from one run to another;
- the considered MLLS, UMLLS and CMLLS estimators require a maximization procedure with respect to the continuous parameter  $\varepsilon$ . This maximization is performed exploiting a two step procedure. In the first step it is performed a coarse search with a step-size  $1/(16\eta M)$  followed, in the second step, by a parabolic interpolation.



Figure 3-9 displays the root mean square error (RMSE) of the considered CFO estimators as a function of the SNR in AWGN (solid lines) and multipath channel (dashed lines) and for one FBMC symbol. The results show that in AWGN channel the MLLS and UMLLS estimators provide the lowest RMSE while in the considered multipath channel, the LS estimator assures the most accurate estimates.

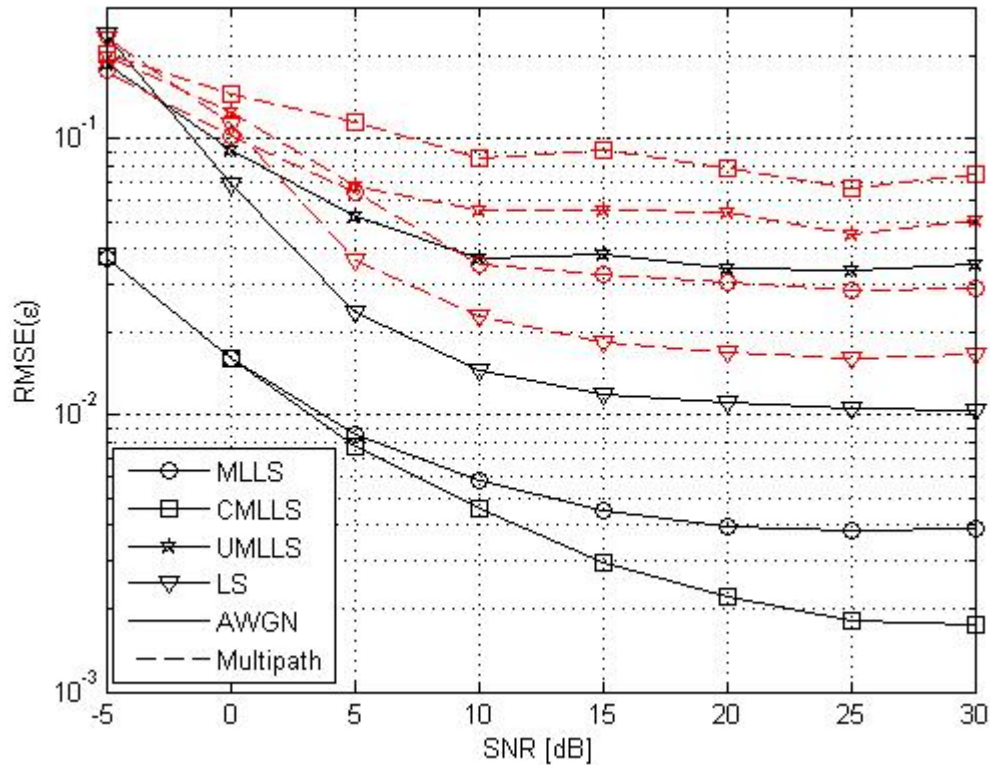


Figure 3-7. RMSE of the CFO estimators as a function of the SNR in AWGN (solid lines) and multipath channel (dashed lines) for  $M=1024$  and  $\eta=1$ .

### 3.3.6 Performance Evaluation of Symbol Timing Estimators

The performance of the MLLS estimator in (74) has been assessed via computer simulations by performing a number of  $10^4$  Monte Carlo trials under the following conditions (unless otherwise stated):

- The value of the timing offset and the carrier phase are uniformly distributed in  $T_s\{-M/4, -M/4+1, \dots, M/4-1, M/4\}$  and in  $[-1/2, 1/2)$ , respectively. In particular, the symbol timing is supposed to be an integer multiple of the sampling period  $T_s$ .
- The size of the set of subcarriers is  $M=1024$ .
- The prototype filter is that described in [4] with an overlapping factor  $K=4$ .
- Numerical results have been obtained by considering two different scenarios: AWGN channel and multipath channel modelled using the Vehicular-A channel model of ITU-R. Moreover, the channel is fixed in each run but it is independent from one run to another.

Figure 3-10 displays the RMSE (normalized to the FBMC interval  $T$ ) of the considered symbol timing estimator as a function of the logarithm of the number of subcarriers  $M$  and for one FBMC symbol. In the figure it is also reported the modified Cramér-Rao bound (MCRB) derived in [6]. The results show that in AWGN channel the proposed estimator provides accurate estimates and, moreover, the performance presents an asymptotic behaviour similar to that predicted by the MCRB. In the considered multipath channel, the ML estimator exhibits a performance degradation due to the mismatch with respect to the considered model. However, the estimates result to be quite accurate for a sufficiently large number of subcarriers also when only one FBMC symbol is used. This statement is corroborated by the results reported in Figure 3-11 where it is shown BER, as a function of the signal-to-noise ratio, obtained exploiting the proposed estimator and one FBMC symbol. In fact, except for very high SNR values, the adoption of the proposed algorithm assures a contained performance degradation with respect to the case of one-tap channel equalization with perfect channel knowledge. Finally, in Figure 3-12 we have analyzed the performance of the ML symbol timing estimator as a function of the residual frequency offset. It results that when a large number of subcarriers is used and only one symbol FBMC is exploited the accuracy of the estimates is not affected by the CFO.

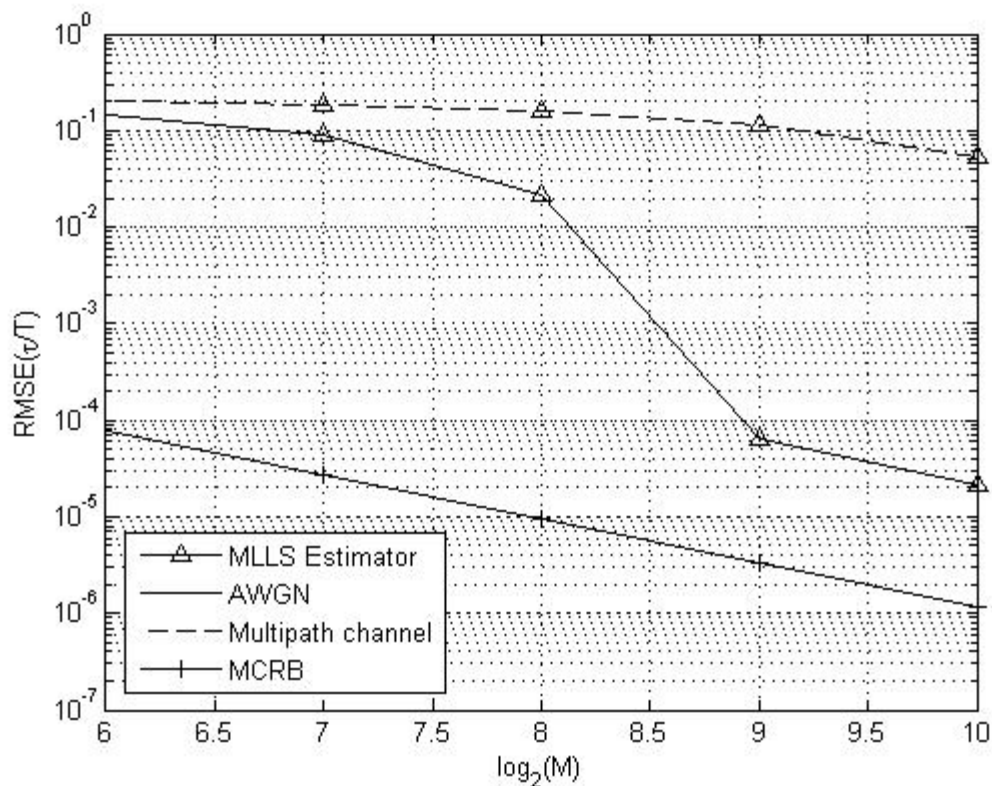


Figure 3-8. RMSE of the MLLS estimator as a function of the number of subcarriers for SNR=20dB and  $\eta=1$ .

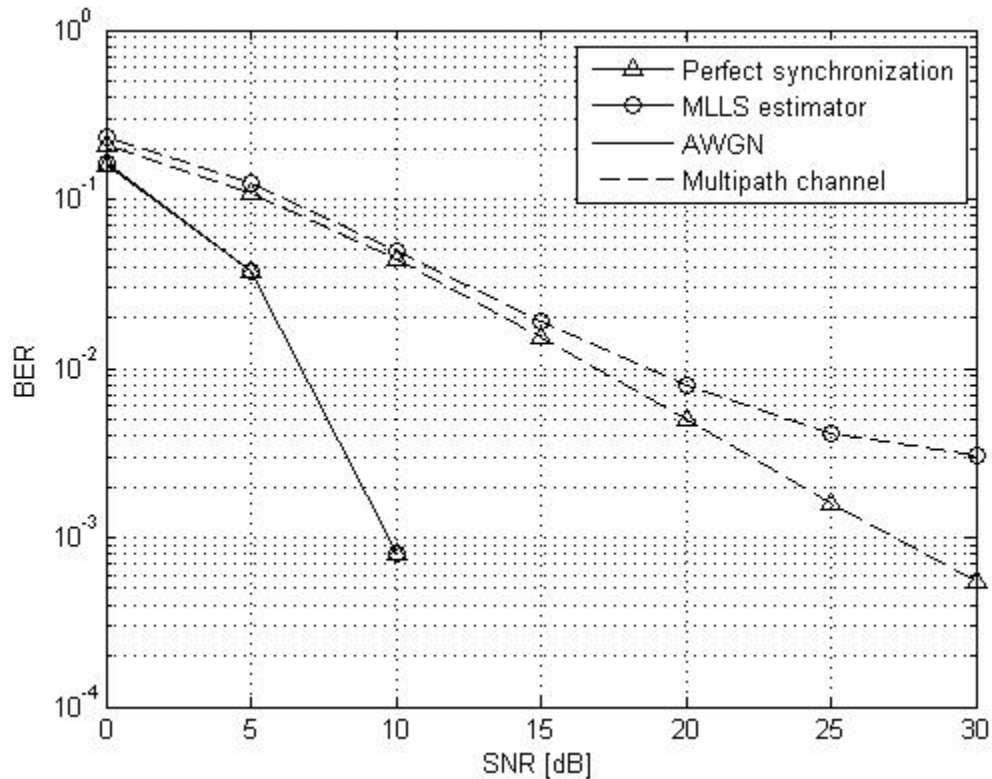


Figure 3-9. BER as a function of SNR for  $M = 1024$  and  $\eta=1$ .

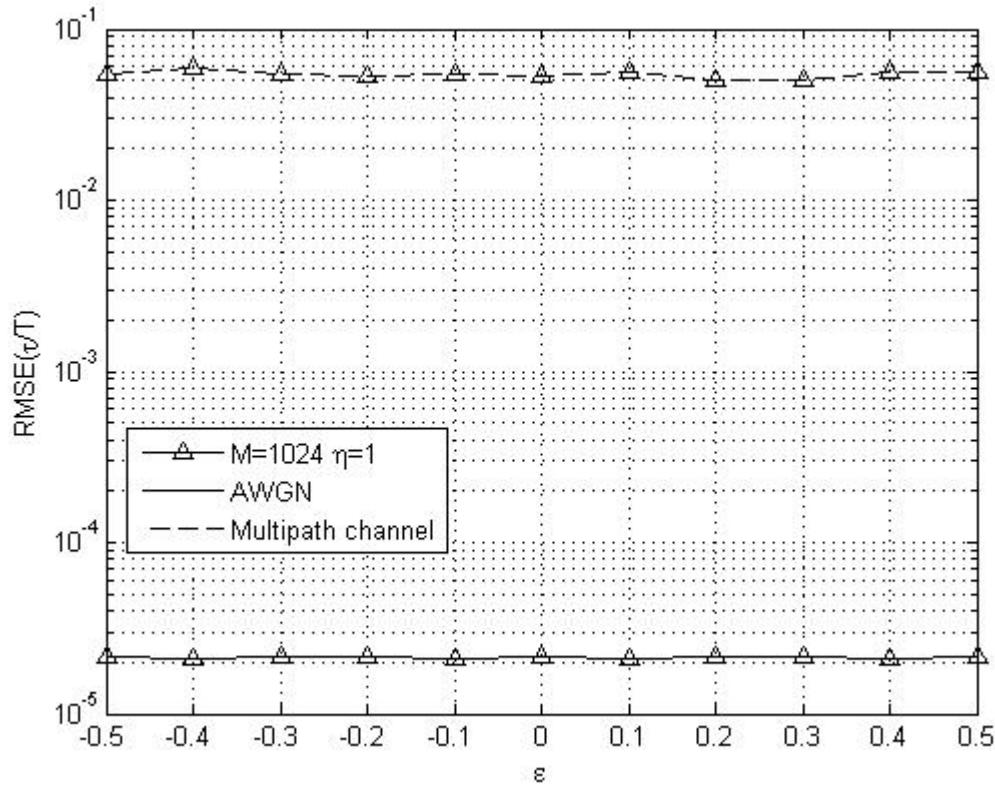


Figure 3-10. RMSE of the MLLS symbol timing estimator as a function of the residual frequency offset for SNR = 20 dB.

### 3.3.7 Comparisons With Preamble-based Estimators

In this subsection, we give general comparisons between the proposed blind estimators and the preamble-based synchronization algorithms considered in the Section 3.3. In particular, blind estimators do not rely on the transmission of the training sequence, but exploit the statistical properties of the transmitted signal, increasing the spectral efficiency at the expense of a poorer performance in the presence of dispersive channel (see Subsections 3.2.3, 3.3.5 and 3.3.6). The complexity of proposed blind estimators is quite similar to that of preamble-based estimators. In fact, the LS CFO estimator provides a closed form CFO solution, while the ML symbol timing estimator requires a maximization procedure. Moreover, as the considered preamble-based estimators, the derived blind estimators operate in the time-domain and do not require the knowledge of the SNR.

### 3.4 Synchronization Based on Scattered Pilots

The auxiliary pilot idea was first introduced in [7] as a way to construct FBMC pilots which can be used basically in the same way as pilots in OFDM. Scattered pilot schemes utilizing the auxiliary pilot idea were investigated in PHYDYAS Deliverable D2.1 [4], together with basic methods for CFO and FTD estimation. In Deliverable D3.1 [8], auxiliary pilot based methods for channel estimation were investigated, along with basic methods for compensating CFO and FTD through subchannel-wise processing.

For completeness' sake, we first state here the basic auxiliary pilot model, considering the case where the pilots are scattered among the data symbols. Then we review the basic elements used in frequency-domain CFO and FTD estimation. In this discussion, we will find that the interplay of estimation and compensation is crucial in this context: If a coarse estimate of CFO or FTD is available, then after compensating the effect, cleaner pilot observations are obtained, and next iteration of the estimation algorithm(s) gives better estimate of CFO and/or FTD. Also compensating the channel frequency response helps to get cleaner pilots. For this reason, CFO and FTD compensation methods, as well as channel estimation and equalization are included in the overall scheme.

In the following discussion of scattered pilot based methods, it is assumed that coarse timing and frequency offsets have been compensated in time domain. The required accuracy of coarse CFO and FTD estimates is an outcome of the following study.

The primary use of these methods is for channel tracking. In normal tracking mode, with continuous flow of data packets, only small CFO and FTD values are expected, and it is enough to use only the estimation algorithms in conjunction with time-domain compensation methods and some filtering to reduce the random variations of block-wise estimates. However, in advanced packet-based radio interfaces, there can be long gaps in the packet flow, especially when the terminal is in idle mode. This may result in significant drift of the CFO and FTD values, and it is advantageous to be able to compensate significant synchronization errors right away for the first received data packet.

For initial synchronization, the developed scheme could be a part of a search procedure, where different coarse CFO and FTD values are tested until synchronization can be established.

The methods are considered here first in the downlink case. The same methods are later in Section 4.2 adapted to the uplink case, for a group of subcarriers.

#### *Auxiliary pilot scheme*

In an OQAM-based FBMC system, either real or imaginary parts of the complex subcarrier symbols are used for data transmission in a staggered fashion. When a real (imaginary) part of a subcarrier symbol is used, the unused imaginary (real) part is, at the receiver, a fairly complicated function of surrounding data symbols. In the following, we refer to these two parts of the complex samples as primary and secondary parts, respectively. With a well-designed filter bank system, like the PHYDYAS reference bank, the crosstalk effects between the primary parts are small enough to be neglected.

The nature of FBMC systems makes it impossible to construct pilot symbols for channel estimation and synchronization purposes in the same way as in OFDM. The approach taken in [7] is based on the observation that it is enough to select one of the subcarrier symbols close to a pilot symbol as an associated auxiliary pilot. Adjusting the primary part of the auxiliary pilot depending on the surrounding data symbols, the secondary part of the actual pilot can be forced to take any desired value. Typically, the secondary part of the complex pilot symbol is forced to zero. Utilizing this idea, pilots can be used in FBMC systems in a similar way as in OFDM. It should be noticed that the relative pilot overhead using this idea is the same as the pilot overhead in OFDM.

In the following, the pilot and auxiliary pilot positions are denoted as  $(k_p, n_p)$  and  $(k_a, n_a)$ , respectively. Typically, the auxiliary pilot is the subcarrier symbol immediately preceding or following the pilot in the same subcarrier, i.e.,  $(k_a, n_a) = (k_p, n_p \pm 1)$ .

Based on Section 2.4 of [4], the secondary part of the pilot sample can be forced to zero by choosing the primary part of the auxiliary pilot as

$$d_{k_a, n_a} = - \frac{\sum_{\substack{(k,n) \in \Omega_{k_p, n_p} \\ (k,n) \neq (k_p, n_p) \\ (k,n) \neq (k_a, n_a)}} d_{k,n} \hat{t}_{k_p - k, n_p - n}}{\hat{t}_{k_p - k_a, n_p - n_a}} \quad (75)$$

Here  $\hat{t}_{k,n}$  is obtained from the transmultiplexer response  $t_{k,n}$  as follows:

$$\hat{t}_{k,n} = \text{Im} \left[ (-j)^{k+n} t_{k,n} \right] \quad (76)$$

Equation uses the data symbols  $d_{k,n}$  in a specified window  $\Omega_{k_p, n_p}$  around the pilot. This window is chosen to include those symbols which have significant effect on the secondary part of the pilot. The window typically used with the PHYDYAS reference filter bank includes subcarriers  $k-1$ ,  $k$ , and  $k+1$  and sample indices  $n-3$ ,  $n-2$ ,  $\dots$ ,  $n+3$ .

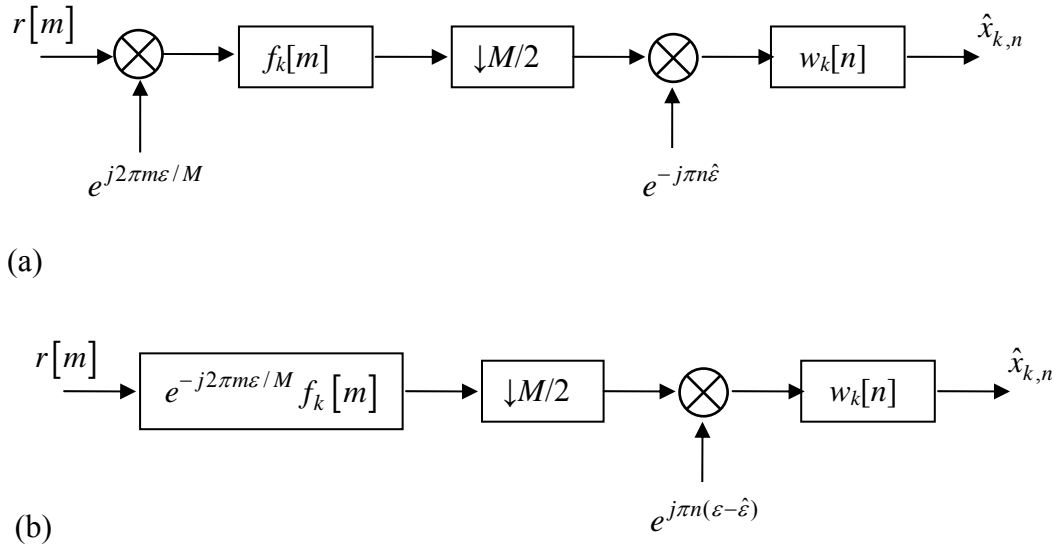


Figure 3-11. Subchannel receiver signal model in the presence of CFO, with CFO compensation and subchannel equalization. (a) Basic model. (b) Equivalent form.

### ***CFO estimation and compensation***

Figure 3-13(a) shows a baseband FBMC receiver signal model for a single subcarrier in the presence of CFO. In the figure,  $\varepsilon$  is the carrier frequency offset normalized to subcarrier spacing. The subchannel signal processing includes time-varying phase rotation to compensate the frequency shift due to CFO, as well as a linear filter as the subcarrier equalizer. Figure 3-13(b) shows an equivalent signal model. We can see the following distortion effects [9]:

- Time-varying phase rotation (frequency shift) by the residual CFO value,  $\varepsilon - \hat{\varepsilon}$ , where  $\hat{\varepsilon}$  is the CFO estimate used in compensation.
- The subchannel frequency response is distorted by the factor

$$F_{CFO}(e^{j\omega}) = \frac{P(e^{j(2\omega/M - 2\pi\varepsilon/M)})}{P(e^{j(2\omega/M)})}, \quad (77)$$

where  $\omega$  is the normalized angular frequency at subchannel sample rate and  $P(e^{j2\omega/M})$  is the prototype filter frequency response in the filter bank design. The PHYDYAS reference filter bank uses linear-phase channel filters in the analysis (and synthesis) filter banks. Consequently, in the zero-phase subchannel processing model, only the magnitude of distorting frequency response is significant. The CFO-related frequency response is shown in Figure 3-14 for some selected CFO values.

- Aliasing effects close to the subband edges.

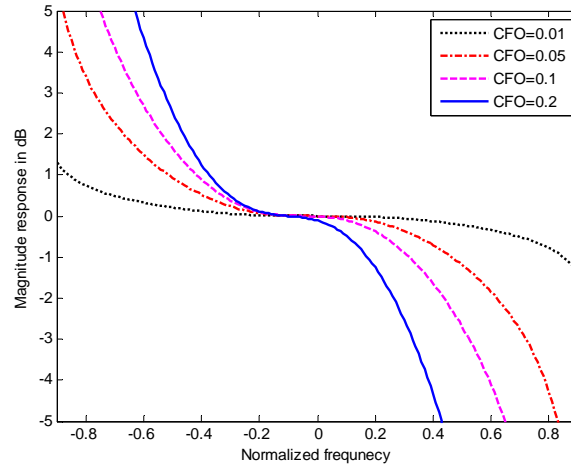


Figure 3-12. Subchannel frequency response distortion due to CFO for normalized frequency offsets of 0.01, 0.05, 0.1, and 0.2.

A very basic scheme for estimating the carrier frequency offsets in multicarrier systems is based on measuring the time-varying phase rotation of the pilots. In an FBMC system, the phase rotation between two consecutive pilots in the same subcarrier is

$$\Delta\phi = \pi\varepsilon \cdot \Delta n \quad (78)$$

where  $\Delta n$  is the pilot spacing in terms of subcarrier samples. In the auxiliary pilot scheme, the time-varying rotation of the pilots is the dominant effect with small CFO values. With linear-phase prototype filters, the transfer function (77) doesn't have an effect on the phase of the subcarrier signal. However, with increasing CFO, inter-symbol and inter-carrier interference (ISI and ICI) will also be introduced on top of the pilots due to the distorted subchannel transfer function. In CFO estimation, the ICI effect is reduced due to averaging over multiple pilot-based measurements, which naturally helps also against the effects of channel noise. Also the aliasing effects appear as noise, which is reduced by averaging.

In case of CFO together with (quasi-) static frequency selective channel with flat-fading subcarriers, the channel response causes constant phase rotation and attenuation, in addition to the time-varying phase-rotation due to CFO. The time-varying part of the CFO is the same in all subcarriers. To improve the estimation accuracy, the CFO estimates can be averaged over multiple subcarriers and over consecutive pilot pairs in each subcarrier. Naturally, it is advantageous to choose a sufficient number of the strongest subcarriers for the estimation. The estimate can be written as:

$$\hat{\varepsilon} = \frac{1}{\pi\Delta n} \angle \left( \sum_{(k,n) \in \Omega_{CFO}} j^{-\Delta n} y_{k,n+\Delta n} y_{k,n}^* \right) \quad (79)$$

where  $\Omega_{CFO}$  is the set of pilot locations used for CFO estimation and  $y_{k,n}$  are received complex subcarrier samples at the pilot locations.



In this scheme, the CFO estimation range is limited to  $[-\Delta f / \Delta n, \Delta f / \Delta n]$ , i.e., it depends essentially on the pilot distance within subcarriers, as discussed in [4].

Considering CFO compensation, the primary function is to compensate the time-varying phase-rotation. With small CFO values, especially with low-order modulation, this gives already significant improvement for the link performance [8]. However, this function alone does not essentially improve the pilot quality since the ICI induced by the distortion transfer function (77) is not affected. For improved compensation performance, the frequency response (77) should be equalized by the linear filter stage in subband processing. This compensation also improves the pilot quality by reducing ICI, so after the compensation, there is a possibility to improve the CFO estimate by applying (79) to the compensated subcarrier signal.

To compensate the distortion transfer function (77), the same linear subchannel filter can be used which is used also for channel equalization and, as discussed later, for FTD compensation. Our basic approach is to use a three-tap subchannel equalizer, which is designed in a frequency-sampled manner. The coefficients can be calculated easily [8] from the target frequency response at the subchannel center frequency and passband edges, i.e., normalized angular frequencies  $\{-\pi/2, 0, \pi/2\}$ . The target frequency response at these points is now calculated by combining the target responses of the subchannel equalizer, CFO compensator, and FTD compensator.

Regarding the aliasing effects close to the subchannel edges, they would be rather difficult to compensate. With modest CFO values, these effects are small, so they are considered here only as additive interference.

### ***Numerical results of CFO estimation and compensation***

All simulation in this section are for the WiMAX-like FBMC system with 10 MHz bandwidth and use the PHYDYAS reference filter bank with FFT-size of  $M=1024$  and impulse response length of  $4M-1$ . Downlink model is assumed and slot and pilot structures are as defined for the PUSC mode, with the modified auxiliary pilot structure described in [4]. All pilots in the DL-frame are utilized for CFO estimation, averaging the phase rotations between all pilots, first in time direction, then over the 50% of strongest subcarriers frequencies containing pilots. The vehicular A channel model of ITU-R is used. The results are obtained as an average over 3000 channel instances. Further, 3-tap subcarrier-wise channel equalizers are utilized. In cases where channel equalization is included, it is based on the same PUSC pilots and linear 2-D interpolation between pilot-wise estimates. The pilots, which are basically 2-PSK modulated, are boosted such that the average energy of a pilot-auxiliary pilot pair is 4.5 dB above the average energy of an OQAM data symbol.

Figure 3-15 compares the CFO estimation and compensation performance with 64-QAM modulation and at  $E_b / N_o = 20$  dB for a frame of 5 ms duration (53 MC symbols) and also for the case in which a zone of only 5 MC symbols is considered. The results include the following cases:

- 1) CFO compensation through frequency shift and amplitude correction based on known CFO; channel equalization based on channel knowledge.
- 2) CFO compensation through frequency shift only, based on known CFO; channel equalization based on channel knowledge.

- 3) CFO compensation through frequency shift and amplitude correction based on CFO estimate; channel equalization based on channel estimate.
- 4) As 3) but with 1 iteration.

It can be seen that the amplitude correction improves the performance with modest CFO values quite significantly. For example, it allows CFO to increase from 4.5 % to 6 % of subcarrier spacing at certain level of CFO degradation, comparing to the case in which the amplitude correction is not applied. Also the iteration gives a worthwhile improvement in performance. The degradation in the quasi-static channel estimation when using only a few multicarrier symbols is evident.

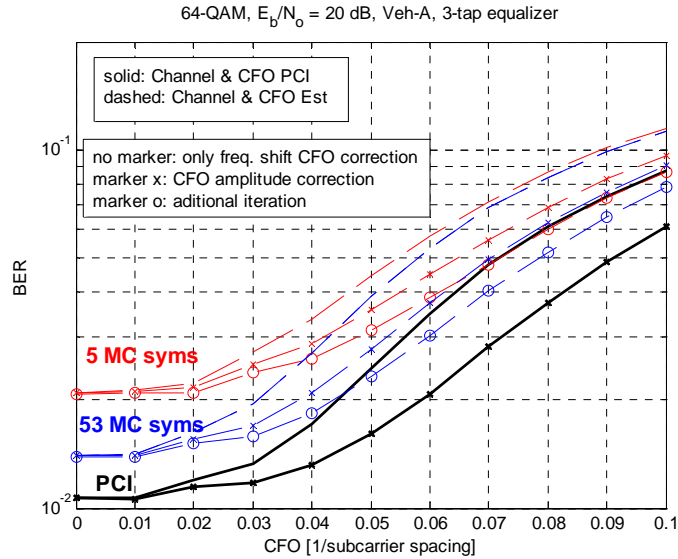


Figure 3-13. CFO estimation and compensation results for 64-QAM in DL-PUSC case using stationary Vehicular A channel model.

Figure 3-16 shows similar results as the above figure for 4-QAM modulation at  $E_b / N_o = 14$  dB and a wider CFO range. It can be seen, that the improvement due to CFO amplitude compensation is not as visible as in the 64-QAM case.

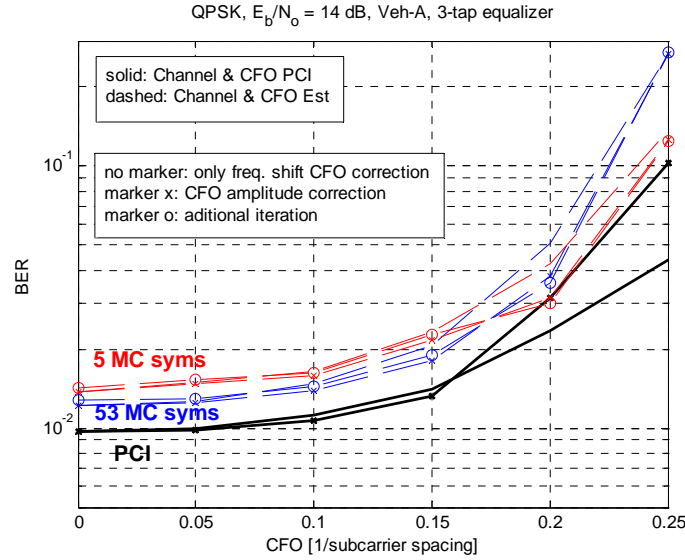


Figure 3-14. CFO estimation and compensation results for 4-QAM in DL-PUSC case using stationary Vehicular A channel model.

### *FTD estimation and compensation*

Timing offset, here also referred to as fractional time delay (FTD), since it is considered as a fraction of the multicarrier symbol length, introduces a linearly frequency-dependant phase slope. One possibility for estimating a relatively small timing offset is to use least-squares match of linear phase response to the subcarrier-wise channel estimates obtained through the auxiliary pilots. This can be approximated simply by averaging phase slope estimates obtained from consecutive pilots along the frequency axis.

One basic difficulty in pilot-based estimation of timing offset is that, in case of significant timing offset, the subchannels cannot be expected to be flat-fading anymore, and the quality of basic pilot-based estimation degrades. Here, again, the interplay of estimation and compensation becomes important.

FTD can basically be compensated by compensating the phase slope within each subchannel using a linear equalizer operating subcarrier-wise. We have used 3-tap subcarrier equalizers also for this purpose [8]. With low-order modulations, and WiMAX-like system parameters, the compensation performance has been good with practically any FTD value. Even with 64-QAM, FTD up to about 10% of the FBMC/OQAM symbol interval can be compensated with good quality. However, earlier tests regarding the combination of estimation and compensation didn't reach the expected performance.

The correct interpolation of the channel from the estimates at the pilots is not a trivial problem in the case of FTD due to the modulo  $2\pi$  phase ambiguity. For example, if the interpolation is separated into amplitude and phase, in order to include the FTD estimation for compensating the phase,  $2\pi$  hops can result in a very unsmooth 2-D channel interpolation. In these simulations we first eliminate the phase slope from the center frequencies of the pilots. Then we perform 2-D complex interpolation to obtain

the channel estimates at the data symbols and also edge frequencies and finally we add again the phase slope to the whole estimation matrix for final compensation at the equalizer.

Here we considered the combination of basic linear phase-slope estimation and 3-tap subcarrier equalizers operated in an iterative manner. An alternative scheme for FTD estimation and compensation, based on iterative interference minimization, was presented in [8]. The performance of these schemes will be compared in future studies.

### ***Numerical results of FTD estimation and compensation***

Figure 3-17 compares the FTD estimation and compensation performance with 64-QAM modulation and at  $E_b / N_o = 20$  dB in a stationary case and similar setup as described earlier. The symbol timing offset is a multiple of the sampling interval  $T_s$ . The results include the following cases:

- 1) No per-se FTD compensation for 1- and 3- tap subcarrier equalizers, i.e., the channel estimation interpolation between the pilots relies only on the pilot estimates.
- 2) FTD compensation based on known FTD; channel equalization based on channel estimate.
- 3) As 2) but averaging the channel estimate at the pilots over 4 consecutive pilots.
- 4) As 2) but with 1 iteration.
- 5) FTD compensation utilizing phase slope based FTD estimate; channel equalization based on channel estimate; 1 iteration of FTD estimation and compensation. This case is presented with a maximum FTD of  $0.1T$ , since at higher timing delays the pilot separation in the DL-PUSC mode is too large to give reliable phase slope estimates without  $2\pi$  jumps.

It can be seen that iteration of the FTD estimation and compensation improves the performance quite significantly, even more than averaging over multiple pilot symbols. As a reference, the curve with perfect channel information, including the knowledge of the FTD, is drawn in the figure. Figure 3-18 shows a similar comparison with the mobility of 60 km/h, assuming 2.5 GHz carrier frequency. Here, the pilot averaging is over 3 consecutive pilots only. The performance for the shown curves is only marginally worse than in the stationary case. The difference is greatest with low FTD's and the performance tends to converge to the 0 km/h case with growing FTD.

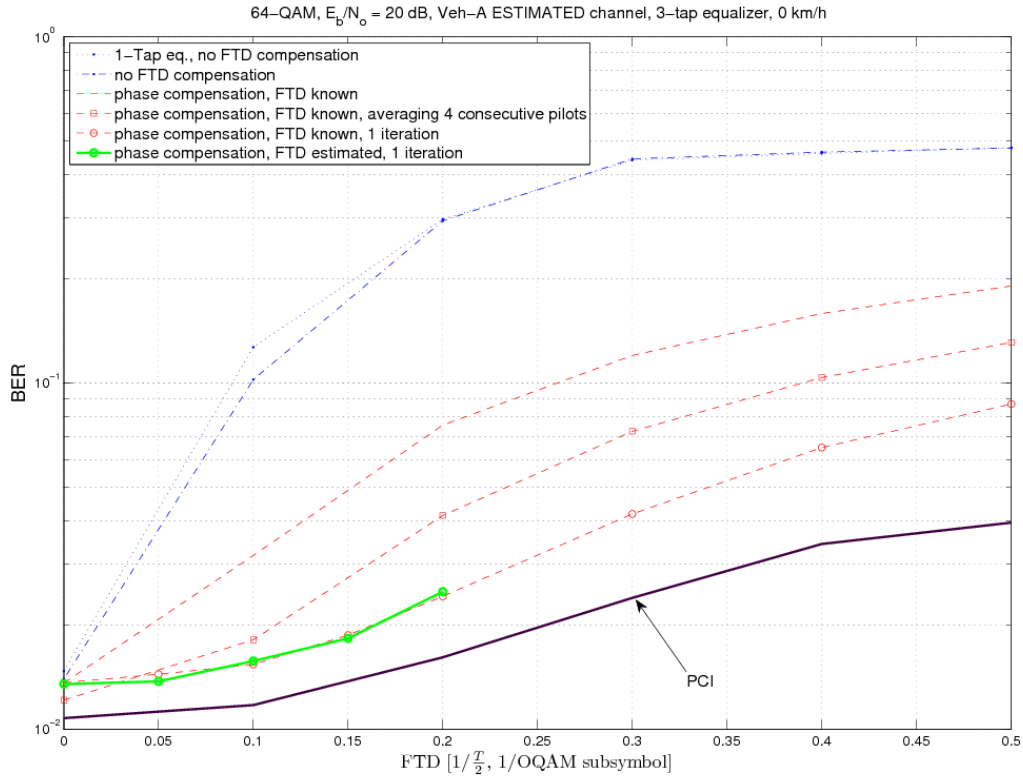


Figure 3-15. FTD estimation and compensation results for 64-QAM in DL-PUSC case using stationary Vehicular A channel model.

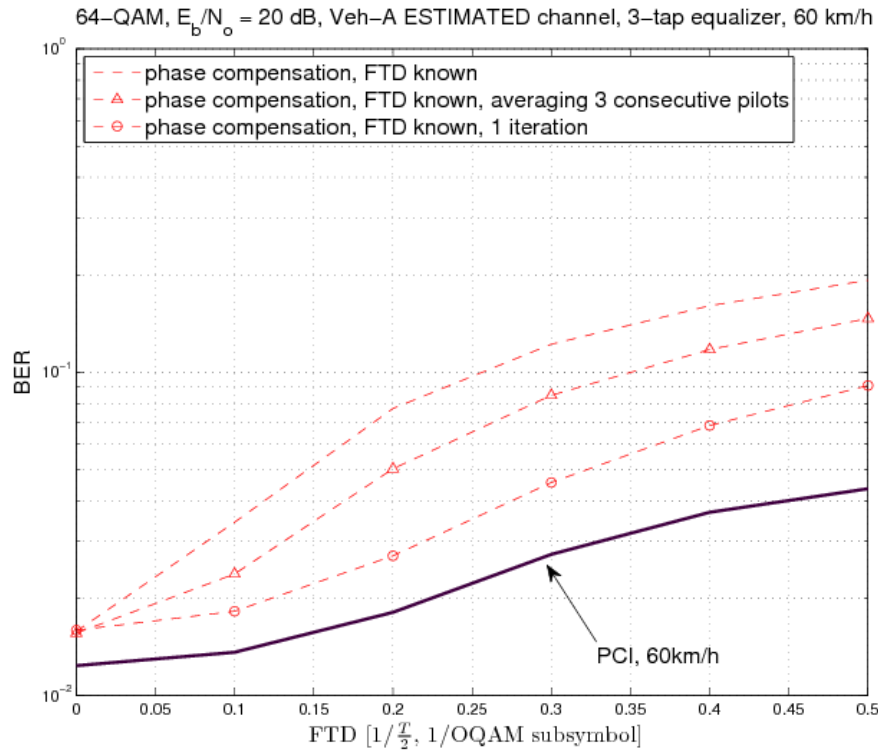


Figure 3-16. FTD estimation and compensation results for 64-QAM in DL-PUSC case using Vehicular A channel model with 60 km/h mobility.

### ***Joint CFO and FTD estimation and compensation***

In practical situations, both CFO and FTD are present in the received signal and both of them have to be estimated, and possibly also compensated with frequency-domain processing. Utilizing the basic ideas discussed above, an obvious solution is to apply CFO estimation & compensation and FTD estimation & compensation, one after another. Also further iterations of both functions may be considered to enhance the performance and extend the feasible estimation range. Then an obvious question is: How to construct optimally the overall iterative estimation-compensation scheme.

There is no obvious analytical answer to this question. The considered CFO and FTD estimation method exhibits certain degree of robustness against the other kind of synchronization error. Details of the iterative structure (i.e., number of iterations of both inner loops and outer loop) can be optimized through simulation-based studies. This is discussed in the following subsection in case of full group of subcarriers (downlink), and later in Section 4.2 in case of small group of subcarriers (uplink).

### ***Numerical results of joint CFO and FTD estimation and compensation***

Based on some experiments, it seems better to start with CFO estimation and compensation, and then execute FTD estimation and compensation at the second stage. Another round of these two stages is expected to enhance the performance, especially if both CFO and FTD values are significant. In more details, the joint CFO estimation and compensation scheme we used is as follows:

- First the CFO is estimated and compensated by a time varying frequency shift.
- Then the FTD and channel are estimated.
- The channel estimate is combined with the result of the time delay estimation stage, and, if applied, with the knowledge of the amplitude distortion introduced by the estimated CFO following Figure 3-14. The subcarrier equalizer coefficients are calculated based on the combined target response.
- If iterative processing is considered, the presented synchronization process is repeated.

For the downlink, the following simulation setup was considered:

- Transmission of a zone consisting of preamble (not used for synchronization) and 4 MC symbols (2 slots in time direction) in DL-PUSC configuration.
- 4-QAM modulation at  $E_b / N_o = 14$  dB and 64-QAM modulation at  $E_b / N_o = 20$  dB.
- Transmission in quasi-static Vehicular-A channel model.

For synchronization, the following modalities are applied:

- 1) Synchronization based on perfect knowledge of the channel distortions, without additional CFO amplitude correction.
- 2) As 1) with synchronization based on estimation of all parameters.
- 3) As 2) with CFO amplitude correction by the 3 tap equalizer.
- 4) As 3) with one iteration of the synchronization stage.

Figures 3-19 to 3-21 show the BER performance of this simulation setup. The first figure presents a general view of the performance as a function of the FTD and CFO present in the system. The following curves are the performance at selected fixed CFOs and FTDs.

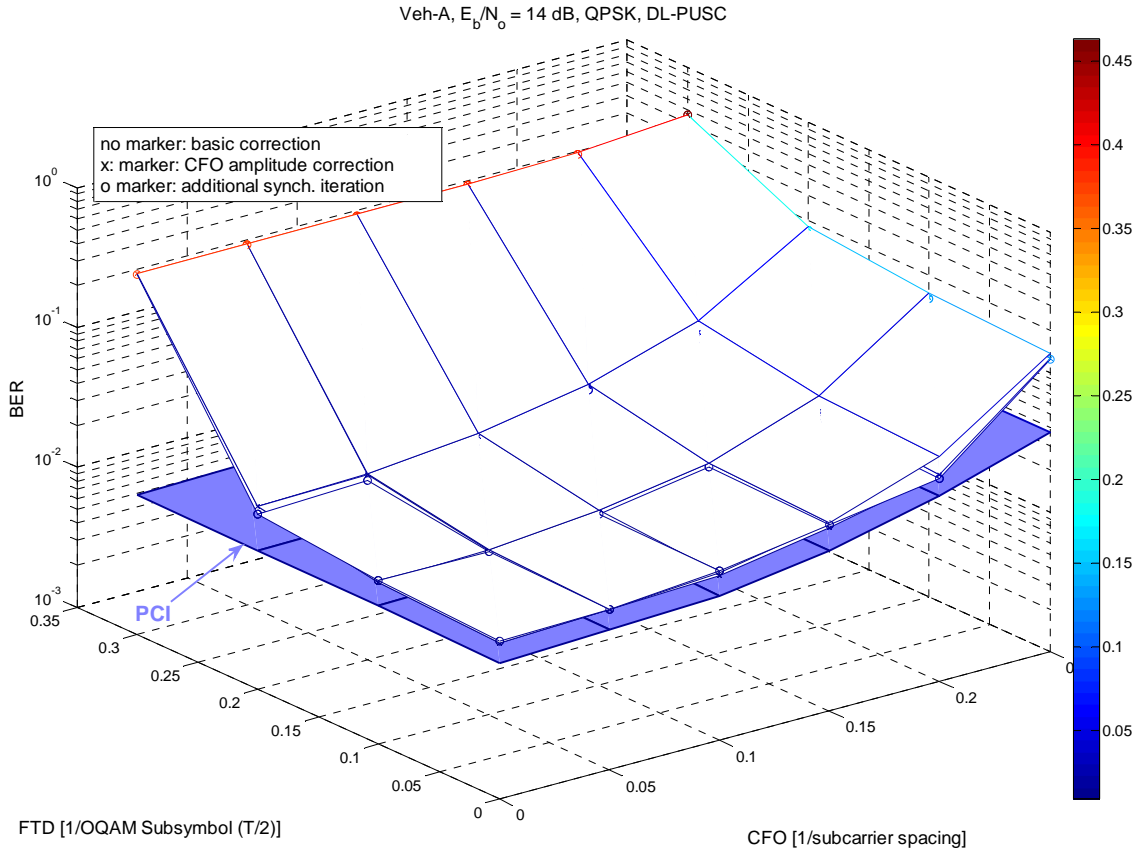


Figure 3-17. BER performance vs. CFO and FTD for a DL-PUSC zone of 4 MC symbols in Vehicular-A channel at  $E_b/N_o = 14$  dB. 4-QAM modulation and different synchronization options.

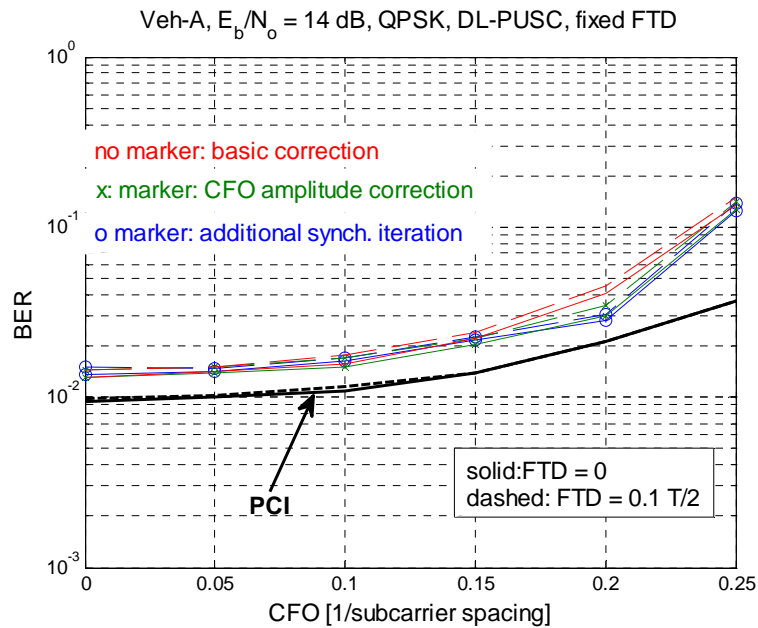


Figure 3-18. BER performance vs. CFO with fixed FTD values. DL-PUSC zone consisting of 4 MC symbols within Vehicular-A channel at  $E_b/N_o = 14$  dB, 4-QAM modulation and different synchronization options.

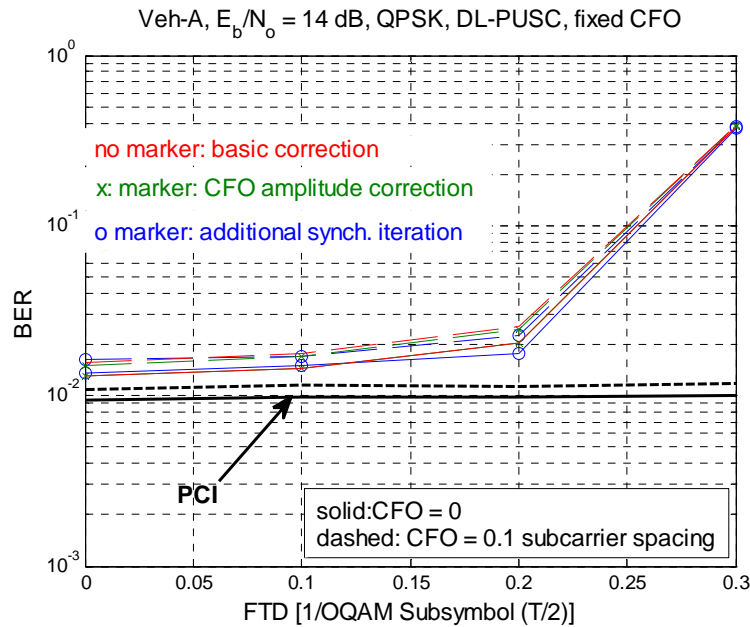


Figure 3-19. BER performance vs. FTD with fixed CFO values. DL-PUSC zone consisting of 4 MC symbols within Vehicular-A channel at  $E_b/N_o = 14$  dB, 4-QAM modulation and different synchronization options.

The presented figures show that for 4-QAM, the iteration has only a certain advantage in the region where the performance commences a rapid decay. As in the above CFO estimation results, the iteration slightly worsens the performance in the region of minimal distortion.

Figure 3-22 and the two following figures present similar results as can be seen in Figures 3-19 to 3-21, but for 64-QAM at  $E_b/N_o = 20$  dB. In this higher order modulation communication, the performance gain obtained from the amplitude compensation of the CFO induced distortion and also from the iteration of the synchronization stage can be separately observed. The performance gain is due to the distortion reduction at the pilots.



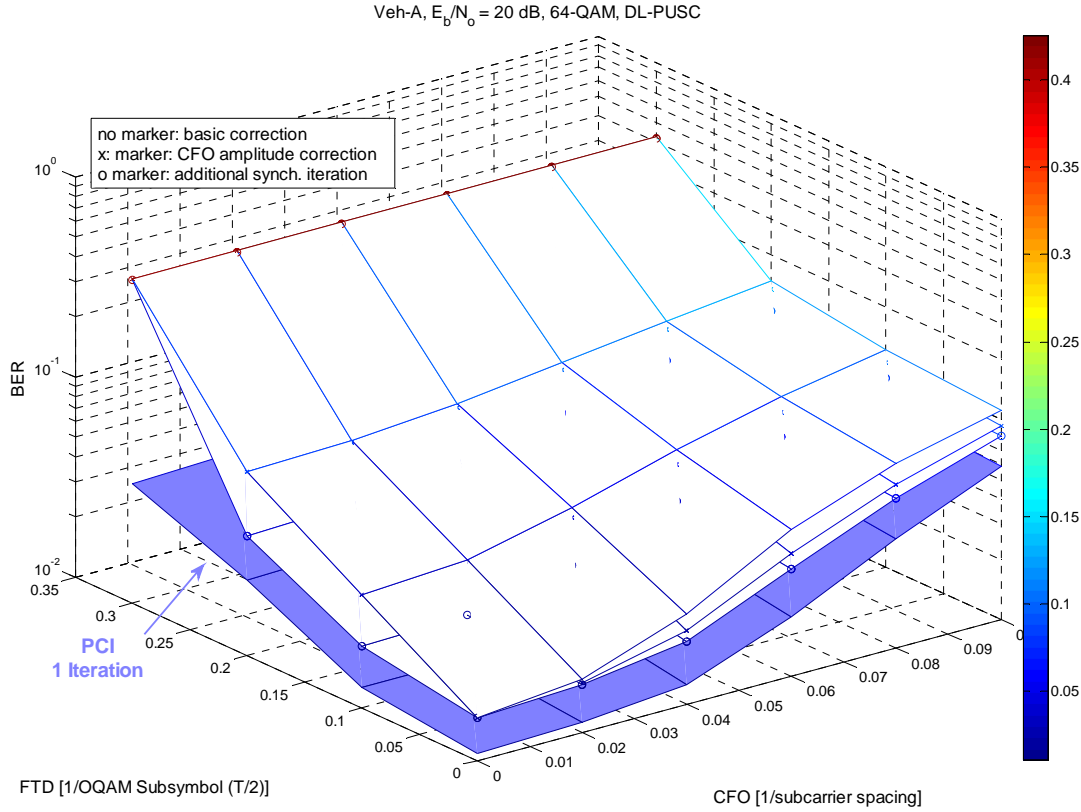


Figure 3-20. BER performance vs. CFO and FTD for a DL-PUSC zone of 4 MC symbols in Vehicular-A channel at  $E_b/N_0 = 20$  dB. 64-QAM modulation and different synchronization options.

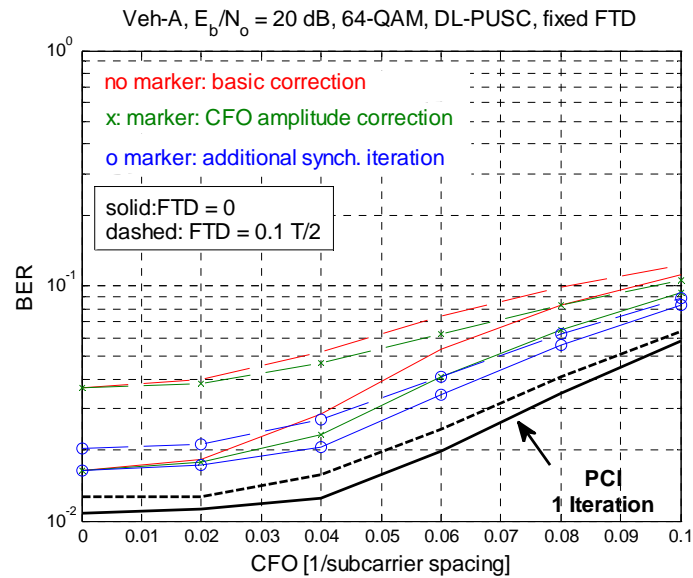


Figure 3-21. BER performance vs. CFO with fixed FTD values. DL-PUSC zone consisting of 4 MC symbols within Vehicular-A channel at  $E_b/N_0 = 20$  dB, 64-QAM modulation and different synchronization options.

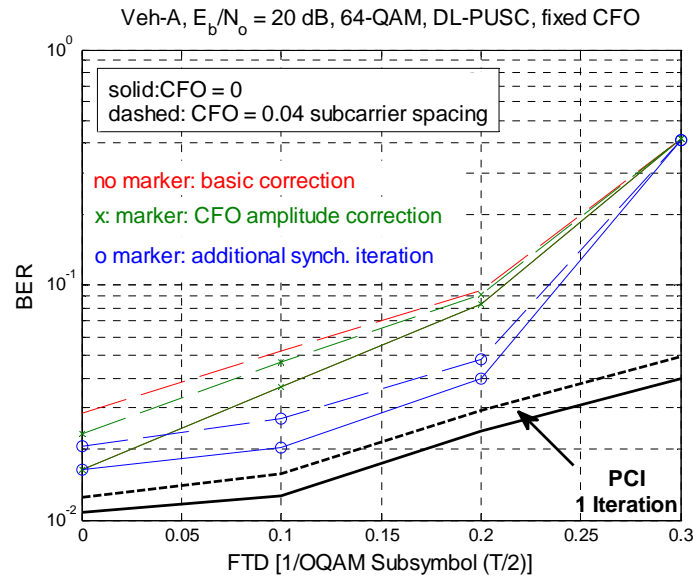


Figure 3-22. BER performance vs. FTD with fixed CFO values. DL-PUSC zone consisting of 4 MC symbols within Vehicular-A channel at  $E_b/N_o = 20$  dB, 64-QAM modulation and different synchronization options.

Next we present the RMS error performance of the synchronization parameter estimates obtained from the 4-QAM simulations (at lower SNR than in the 64-QAM case). Figures 3-25 and 3-26 present the error of the FTD estimation, first the general 3-D overview, then the slices at fixed CFO. The following Figures 3-27 and 3-28 show the dual case, i.e., the RMS error in the CFO estimation. From the figures that show the variation with respect to the two variables, we can learn that the error as a function of the distortion it estimates depends only marginally on the other distortion variable. It is interesting to note that the iteration actually degrades the CFO estimate slightly. Thus, when explicit CFO estimate is needed, it is better to use the first estimated value, before iteration. The same tendency is followed in the higher SNR case (64-QAM simulations) for the CFO estimation. However, the FTD estimates when iterating are marginally better here than when no iteration is applied.

In summary, we can conclude:

- The iterative compensation scheme significantly extends the CFO and FTD compensation range with high-order modulations. With 4-QAM, the improvement is marginal.
- Iterations are not useful for reducing the CFO and FTD estimation errors.
- The proposed joint estimation approach works well for CFOs up to  $\pm 15\%$  of subcarrier spacing and FTDs of  $\pm 10\%$  of FBMC/OQAM symbol duration. These limits are imposed by the pilot separation in time and frequency domain of the respective WiMAX transmission mode.
- Relatively good compensation performance can be achieved with 4-QAM (64-QAM) modulation for CFOs up to  $\pm 15\%$  ( $\pm 4\%$ ) of subcarrier spacing and FTDs of  $\pm 10\%$  ( $\pm 8\%$ ) of FBMC/OQAM symbol duration.

Since the CFO and FTD values are relatively slowly varying, the parameter estimates can be improved by extending the averaging range. This can be achieved by using a higher number of symbols in the estimation, or even by averaging over multiple consecutive transmission bursts in the tracking mode. These studies were based on using a very basic FTD estimation method based on the phase slope. The

next step is to use the interference cancellation based FTD estimation method [8] in the joint CFO-FTD estimation and compensation scheme. Preliminary studies indicate that this method could provide significantly extended FTD estimation and compensation range.

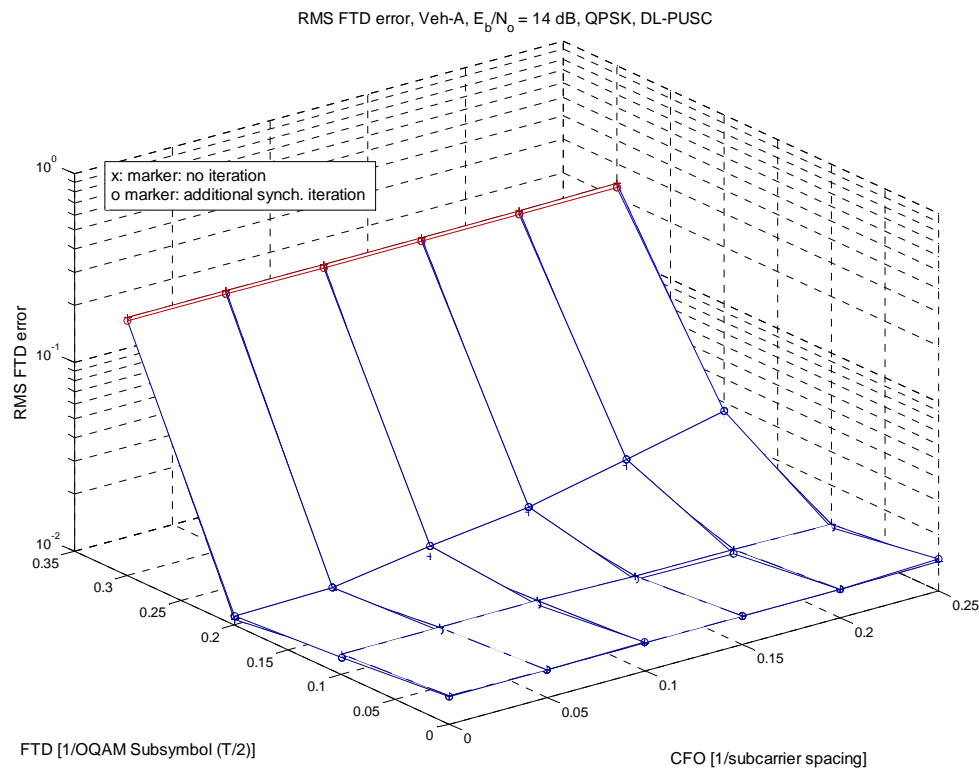


Figure 3-23. RMS error in FTD estimation in a zone consisting of 4 MC symbols with DL-PUSC configuration in Vehicular-A channel at  $E_b/N_o = 14$  dB and with FTD and CFO distortions. 4-QAM modulation. Straight estimation or 1 iteration.

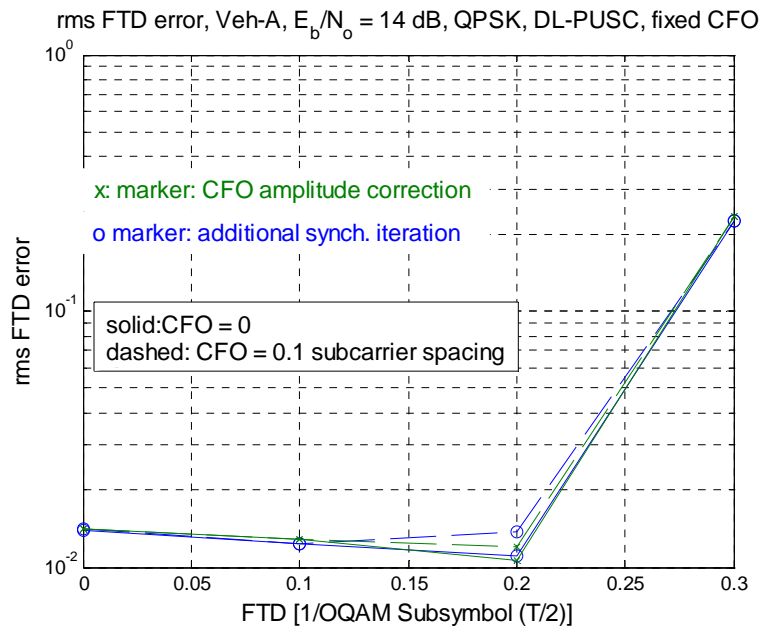


Figure 3-24. RMS error in FTD estimation in a zone consisting of 4 MC symbols with DL-PUSC configuration in Vehicular-A channel at  $E_b/N_o = 14$  dB with fixed CFO values. 4-QAM modulation. Straight estimation or 1 iteration.

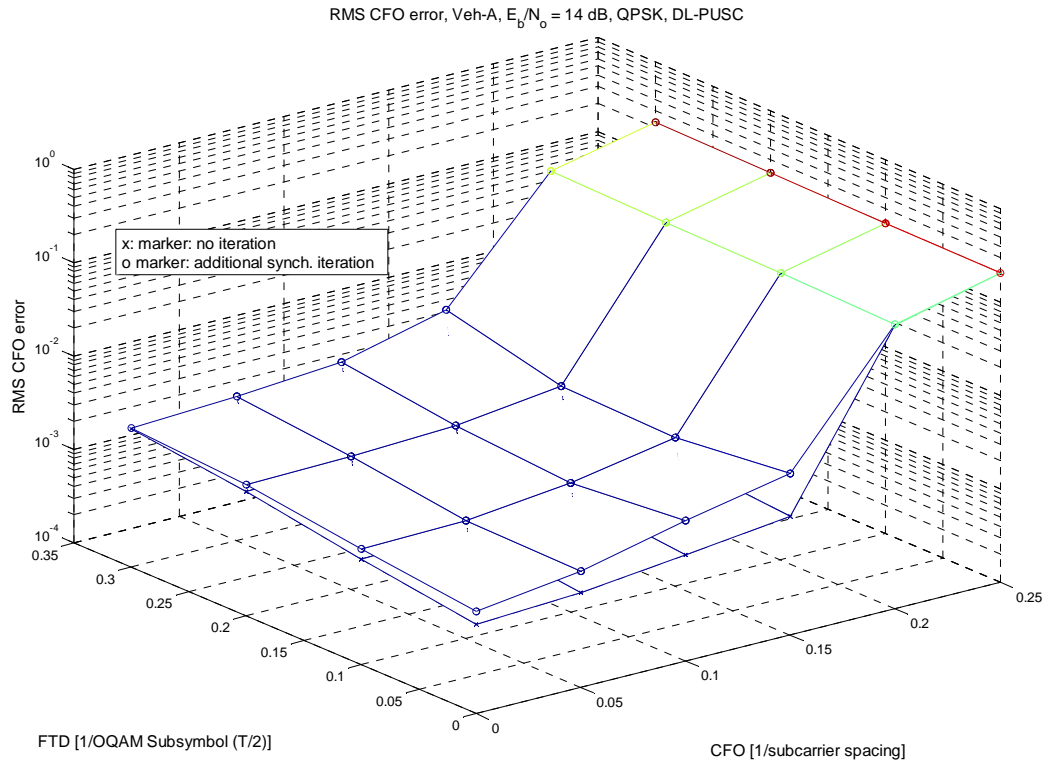


Figure 3-25. RMS error in CFO estimation in a zone consisting of 4 MC symbols with DL-PUSC configuration in Vehicular-A channel at  $E_b/N_o = 14$  dB and with FTD and CFO distortions. 4-QAM modulation. Straight estimation or 1 iteration.

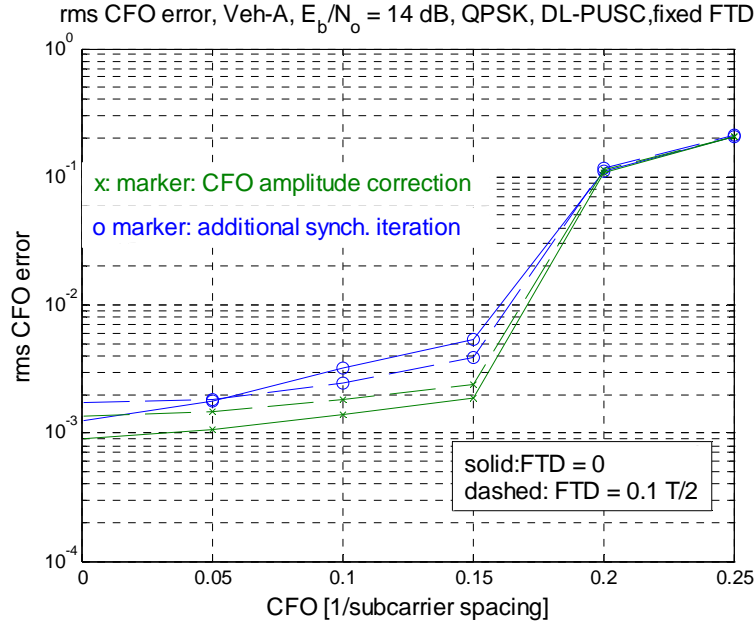


Figure 3-26. RMS error in CFO estimation in a zone consisting of 4 MC symbols with DL-PUSC configuration in Vehicular-A channel at  $E_b / N_o = 14$  dB with fixed FTDs. 4-QAM modulation. Straight estimation or 1 iteration.

### 3.5 Decision-directed tracking of fractional time delay

In this section, we analyze, by simulations, the performance of the decision-directed tracking method for fractional time delay proposed in D2.1. The objective is to show that it is possible, under some reasonable conditions, to perform the tracking of the timing without the help of any pilots.

#### 3.5.1 Simulation setup

The simulations are using the estimation method as presented in Section 3.4 of D2.1 applied to a WiMAX scenario. The WiMAX system considered here is working with 1024 subcarriers on a 11.2 MHz bandwidth. The PHYDYAS prototype is used with overlapping factor 4. We consider the downlink case, with a Vehicular-A channel model.

As described in deliverable D2.1, the fractional time delay (FTD) estimator provides an estimate proportional to the true value (at least in some reasonable range around the optimal value) which is then fed into a tracking loop with some kind of low-pass filtering. In our setup, the low-pass filtering is simply done by computing an average of the last 30 outputs. This corresponds to an estimate based on 30 OFDM-OQAM symbols. It is obviously only possible in tracking, as the initialization is much shorter. Then, based on this average over 30 symbols, the fractional time delay is adjusted at the receiver. It has been assumed here that the estimation/adjustment scheme is implemented sequentially. That is to say, each timing adjustment is based on a block of 30 received symbols, independent of previous blocks. It is theoretically possible to have a digital locked loop with a lowpass filter working on the estimator outputs and adjustments being made to the timing at every sample, but the implementation

used here is of course much simpler, and should not suffer from any significant degradation in performance. The size of the block for estimation can be increased above 30, depending on the desired tracking capabilities. The value chosen here ensures that the system is capable of following timing changes up to approximately 300-400Hz, which is much more than what is needed for typical timing drifts. Hence increasing the size of the blocks for estimation could further reduce the estimation noise and the observed jitter.

The timing adjustments are performed by shifting the received signal by a few samples in either direction, so that the window of application of the analysis bank is shifted accordingly. Only integer adjustments are made.

This simulation focuses on timing estimation. Hence, it is assumed that channel estimation is constantly performed to adapt the equalizer to changes of the channel (including the effect of timing changes on the channel). For the current simulations, we use either perfect channel estimation or channel estimation methods based on pilots, as presented in D3.1. Obviously, in order to really decrease the need of pilots, the tracking of the equalizer with limited amount of pilots will also have to be investigated. Similarly, it is assumed that CFO has been estimated and corrected, so we neglect the effect of CFO in these simulations.

### 3.5.2 Comparison with Theoretical Results

First, we present several results to validate the theoretical performance presented in deliverable D2.1. The simulated s-curve of the estimator, for perfect channel estimation, is shown in Figure 4-17, where 4-QAM is used, and  $E_b/N_0=15$  dB. It is obtained by averaging over 100 simulations. Each simulation performs an estimate on 30 symbols as stated above. Only the positive half is represented as the curve is symmetrical around a zero FTD. The corresponding RMS estimation error is shown in Figure 4-18. The results confirm the linearity of the s-curve as well as the good range of the method. It shows that the tracking scheme is able to correct an error of up to  $\pm 25\%$  of the symbol duration. Note that the s-curve amplitude has been normalized in the figure, as the actual amplitude is a parameter that can be adjusted when used in a tracking loop. Similarly, the bias has been suppressed, as it is difficult to define in the case of a selective channel and usually has a negligible impact on the performance, as long as it remains reasonable (more on this below). The RMSE (root mean square error) provides an idea of the jitter that can be expected when using this estimation in a tracking loop. Even though some more complex method might provide higher performance, the corresponding error is remaining on the order of 1% of the symbol duration here which is certainly sufficiently low to avoid any performance degradation.

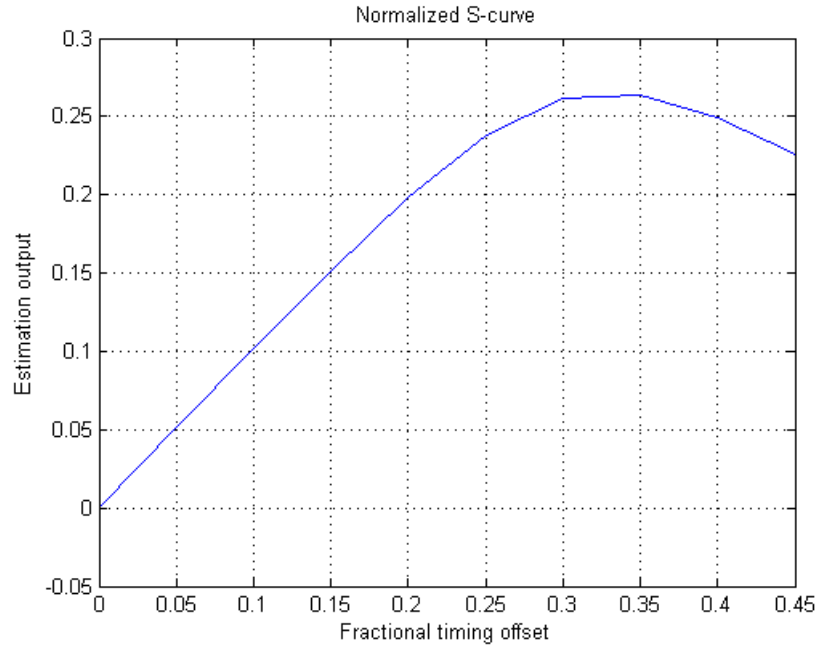


Figure 4-27. Normalized s-curve for the proposed timing estimator (4-QAM,  $E_b/N_0=15$  dB)

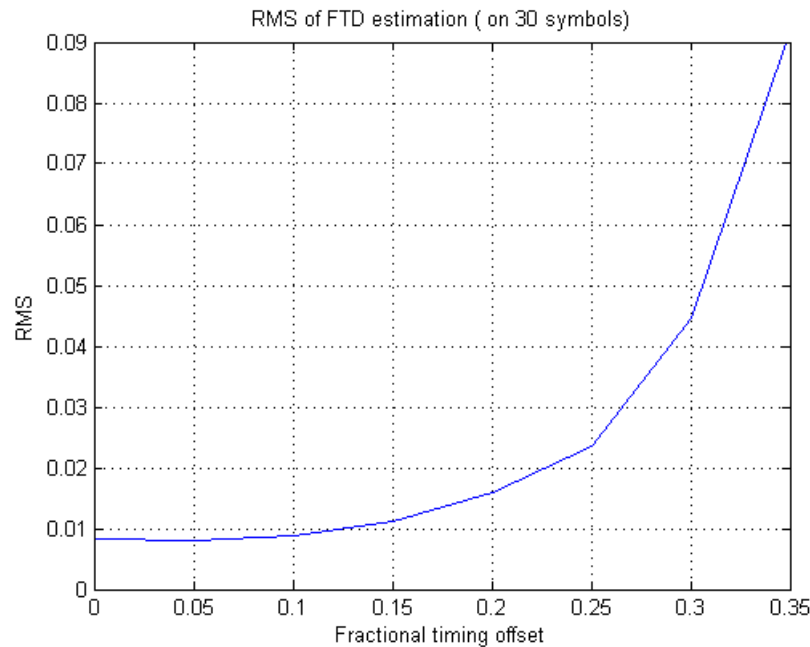


Figure 4-28. RMS error for the proposed estimation method.

Both results presented above assume that the equalizer uses perfect channel estimation. In practice, the channel estimation error may generate additional detection errors and impact the performance of the timing estimator. Figure 4-19 and Figure 4-20 provide the same results when a pilot channel estimation scheme is used, as proposed in D3.1. The DL-AMC32 pilot structure is considered here while all other

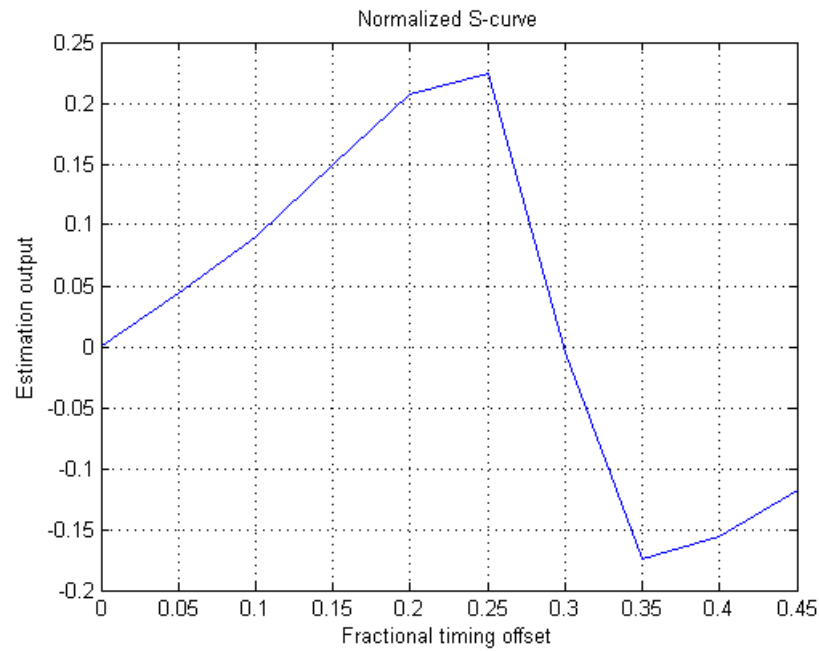


Figure 4-29. Normalized s-curve with imperfect channel estimation (4QAM,  $E_b/N_0=15$  dB)

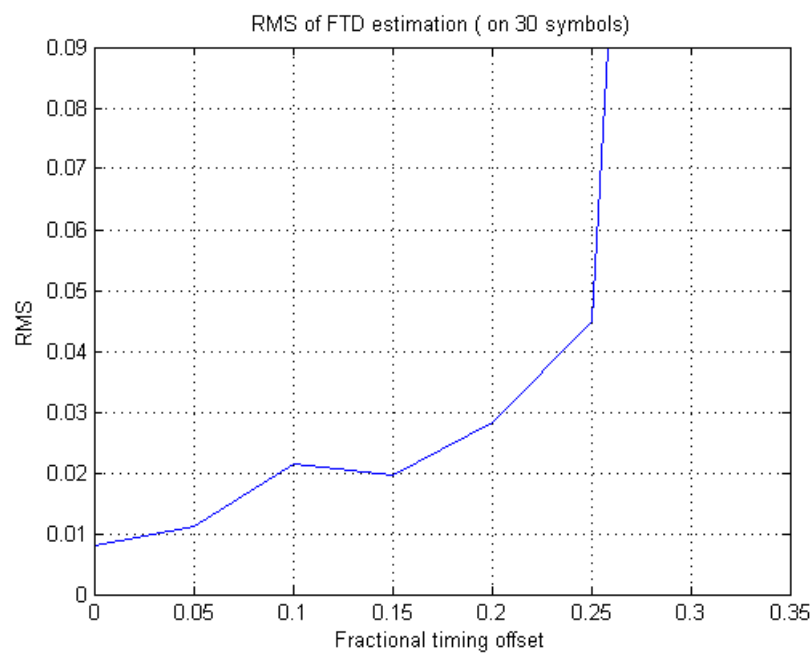


Figure 4-30. RMSE with imperfect channel estimation (4QAM,  $E_b/N_0=15$  dB)



In a low SNR environment, the large amount of detection errors will decrease the performance of the estimation method even further. Similar results are shown in Figure 4-21 and Figure 4-22 for a lower SNR situation of  $E_b/N_0=10$  dB (but with perfect channel estimation in this case). Note that we do not take into account the effect of coding here. Hence the detections error rate corresponds to the uncoded BER. At an FTD of 0.25, the BER is approximately 0.16, which appears to be just sufficient to provide a reasonable estimation. All higher values result in a BER above 0.2 and the obtained estimation is unreliable.

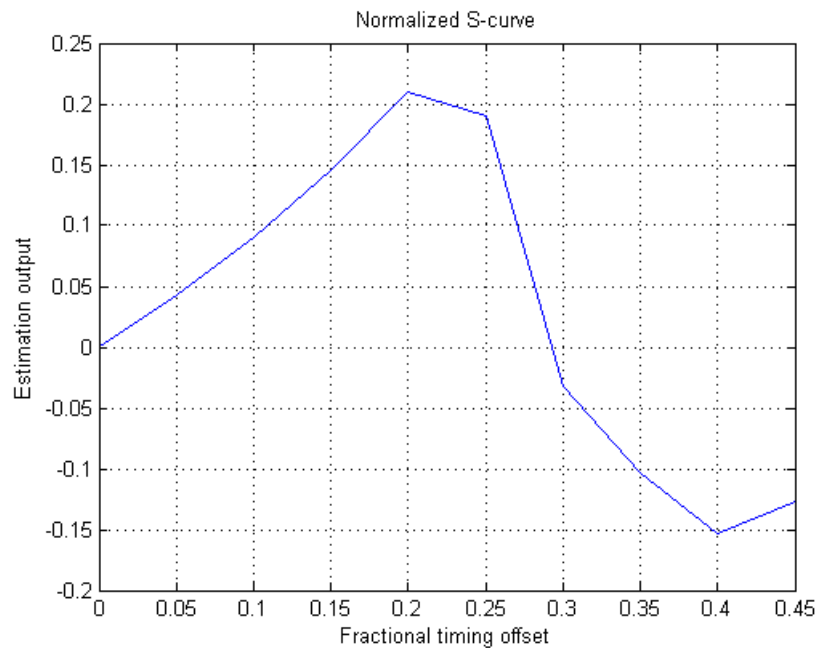


Figure 4-31. Normalized s-curve with perfect channel estimation (4QAM,  $E_b/N_0=10$  dB)

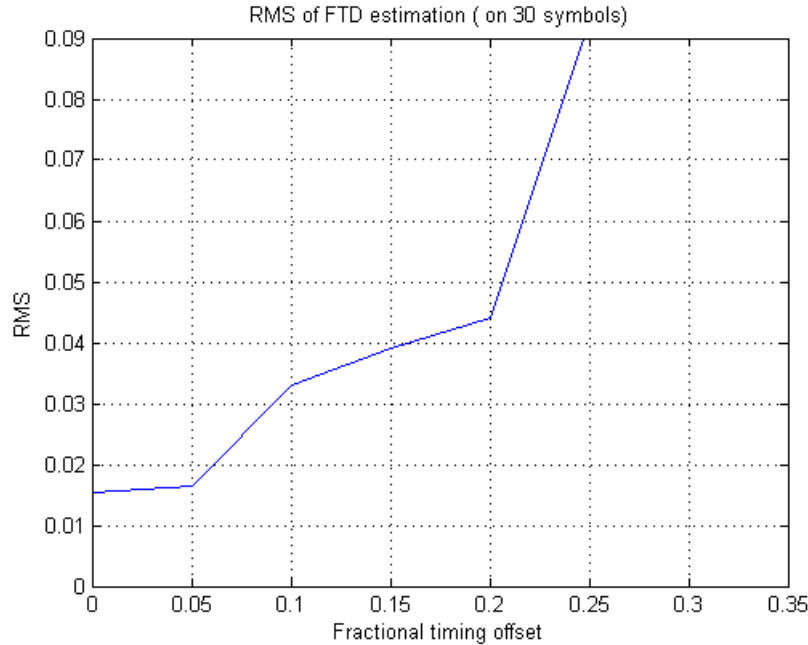


Figure 4-32. RMSE with perfect channel estimation (4QAM,  $E_b/N_0=10$  dB)

In conclusion, it seems that the method performs well as long as the BER is kept reasonable ( $10^{-1}$  or below), which should always be the case during tracking (hence in actual transmission). The linearity range is around  $\pm 30\%$  in the best situations, and is limited by the detection error rate in other cases. The acquisition range could be further increased by using the error correcting decoding inside the loop, so that less decision errors are made. This however increases the delay inside the synchronization loop and thus decreases the tracking performance for varying channels.

### 3.5.3 Tracking Simulations

In this section, we investigate actual tracking simulations. Each simulation starts with some FTD, and the timing is adjusted every 30 symbols according to the estimation method and the procedure described above. The amplitude of the adjustment (which is directly related to the gain of the tracking loop) is set to half of the normalized FTD estimation. Imperfect channel estimation is used in all these simulations with the DL-AMC32 pilot pattern. Figure 4-23 shows an example of such a simulation, for a starting FTD of 0.2, with 4-QAM and  $E_b/N_0=15$  dB. The initial error is recovered in a few iterations and the remaining jitter is kept around 1% of the symbol duration.

In order to compute the jitter, several of those simulations are run, and the average remaining timing error after convergence is computed. Figure 4-24 shows the average jitter obtained as a function of the signal to noise ratio ( $E_b/N_0$ ). All simulations start with an initial FTD of 0.2. As expected in the example simulation, the jitter is lower than 1%, even at low SNR.

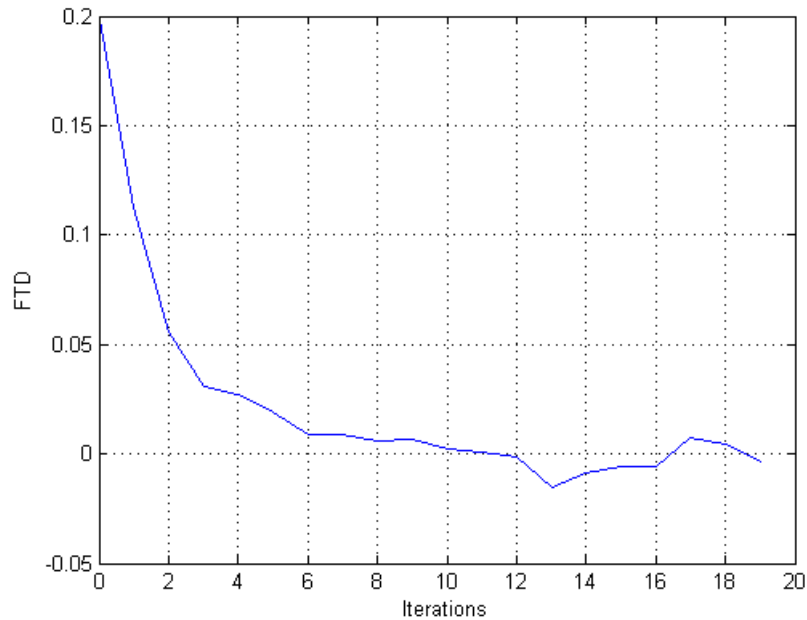


Figure 4-33. Example of tracking simulation

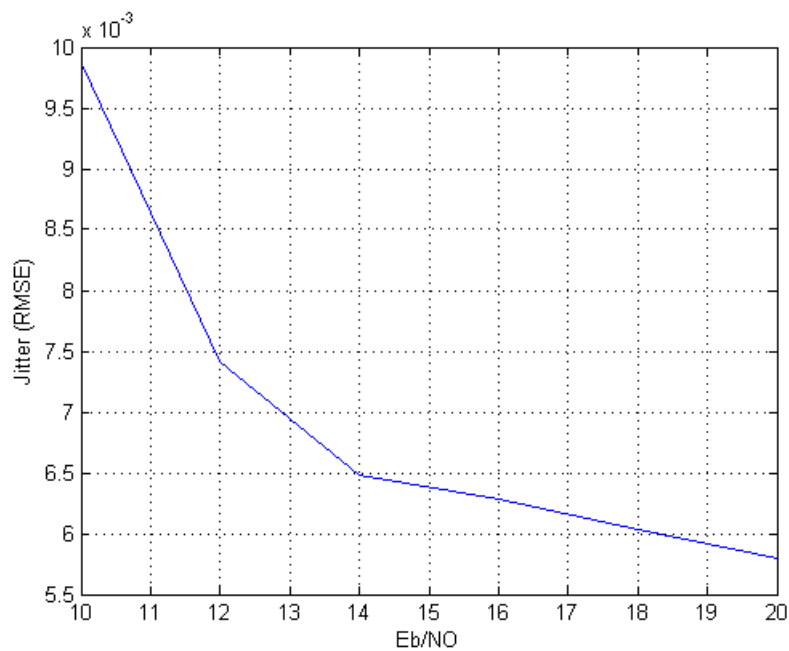


Figure 4-34. Jitter vs. signal to noise ratio

In addition to the jitter characteristics, it is interesting to investigate whether there is any risk of divergence of the algorithm, especially when the initial FTD is high, and hence when the estimation is not in the linearity range. For various initial values of the fractional time delay, multiple identical

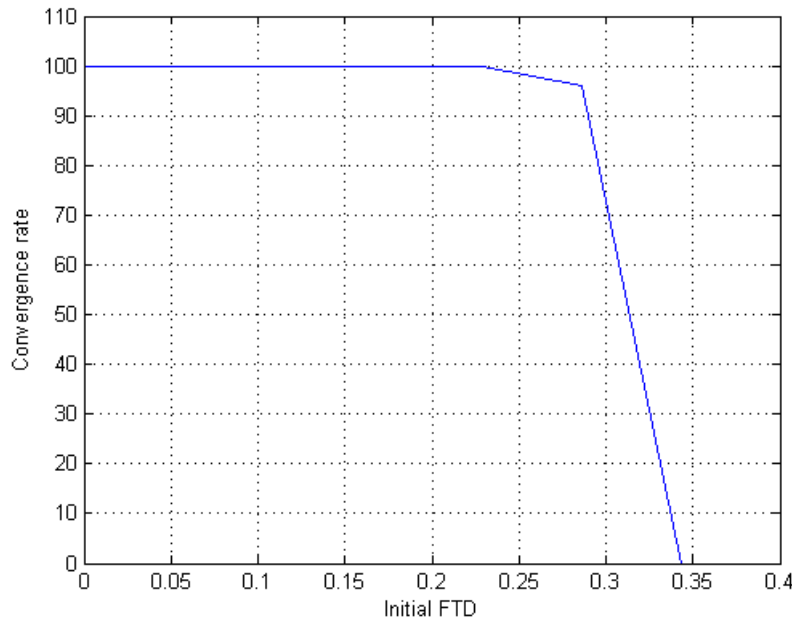


Figure 4-35. Convergence rate of the tracking scheme (4-QAM,  $E_b/N_0=15$  dB)

### 3.5.4 Conclusion

Several simulations have been presented showing the viability of the proposed tracking scheme in a WiMAX-like scenario. The s-curve has been shown to be linear on a range of around  $\pm 20\%$  of the symbol duration, even with imperfect channel estimation. The method seems robust enough against detection errors, up to an uncoded BER of 0.1. The presence of coding might even decrease the detection errors and thus further improve the robustness of the method in low SNR situations. Tracking simulations have also shown that a reasonable jitter can be maintained and almost no divergence occur as long as the initial FTD stays within the linear zone of the s-curve. All these results indicate that pilots are not necessary to maintain the timing during transmission. The timing can be tracked blindly, as long as some accurate channel estimation is performed. Now, in order to significantly decrease the amount of pilots, it will be necessary to study (semi-)blind channel estimation techniques.

All the above simulations have been performed in the downlink case. As for many other synchronization problems, the uplink in a multi-user scenario creates additional issues that need to be taken care of before being able to implement this method.

### 3.6 Filter Bank Memory Preloading and Frequency Domain Processing

In high speed communication systems, the transmission of the data is preceded by an initialization phase which serves to align the receiver and the transmitter and to measure the channel for equalization purposes. When burst transmission is employed, as in high efficiency multiuser radio and wireless networks, the initialization phase can be introduced at the beginning of each burst. In this case, the burst begins with a preamble of one or several symbols, the transmission parameters are estimated and the estimations are used for the transmission of the data. The preamble-based estimations can be refined or updated during the rest of the burst with the help of known symbols called pilots. Alternatively, the preamble can be introduced only once in a group of symbols, in order to reduce the loss of throughput.

Once the presence of the useful signal has been detected by the receiver, the transmission parameters which have to be estimated are the timing offset, the frequency offset, in order to align the transmitter and the receiver in time and frequency, and the channel frequency response, in order to compensate for the distortion. Since the preamble must be made as short as possible, it is desirable to perform the estimations of the 3 parameters simultaneously. The channel estimation at all the sub-carrier frequencies requires a complete multicarrier symbol. In order to take into account the channel impulse response and the timing offset, the preamble must be greater than one symbol. In fact, a convenient choice is 2 consecutive identical symbols which, in addition, due to the periodicity of the received signal, allows for a simple CFO measurement method. These symbols are derived from a pseudo-random sequence in order to satisfy the requirements of flat frequency spectrum and reduced peak-to-average power ratio (PAPR).

As far as initialization in FBMC is concerned, the issue with the approach is the impulse response of the prototype filter which imposes a transition phase. An illustration is given in Figure 3-29, where the system has 128 sub-channels and the synthesis filter bank (SFB) in the transmitter generates a real signal, which implies that 256 sub-channels are used altogether, to account for both positive and negative frequencies. The prototype filter length is  $L=1025$  and the symbol overlapping factor is  $K=4$ . The impulse response of the prototype filter shown in Figure 3-29 provides the coefficients of the filter bank.

A crucial feature for the present topic is that the frequency response of the prototype filter is zero at the frequencies which are integer multiples of the sub-channel spacing, as shown in Figure 3-30. With this feature, at their center frequencies, the filters in the bank are independent.

The delay of the linear phase prototype filter is  $(L-1)/2=512$ , which corresponds to 2 multicarrier symbols. When data are applied to the system, a transition phase of 2 symbols is introduced, as illustrated in Figure 3-31.

Now, the objective of the present section is to show how the prototype filter transition phase for the preamble can be skipped and how the transition phase for the data can be exploited to improve the estimations of the transmission parameters. In addition, simple and efficient means for the estimations are provided.

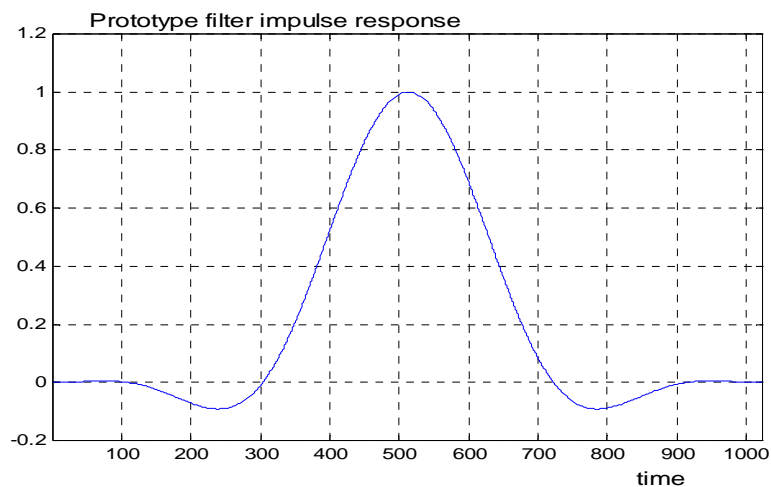


Figure 3-36. An example of prototype filter impulse response

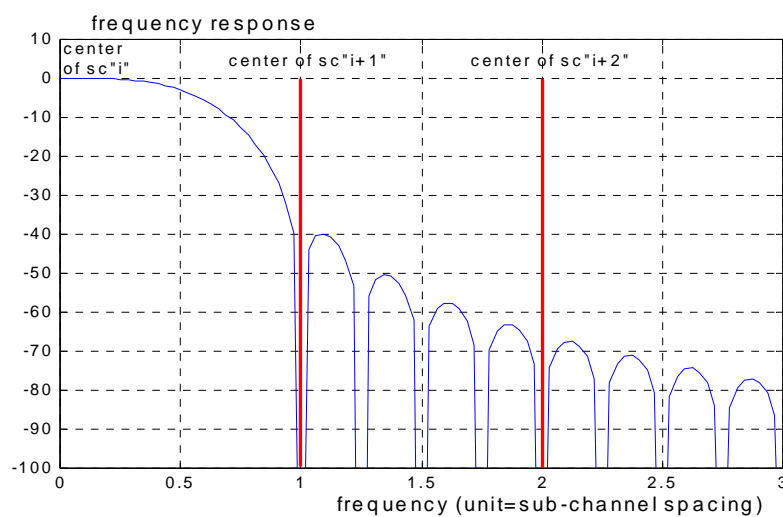


Figure 3-37. Frequency response of the prototype filter and positioning of neighbouring sub-channels

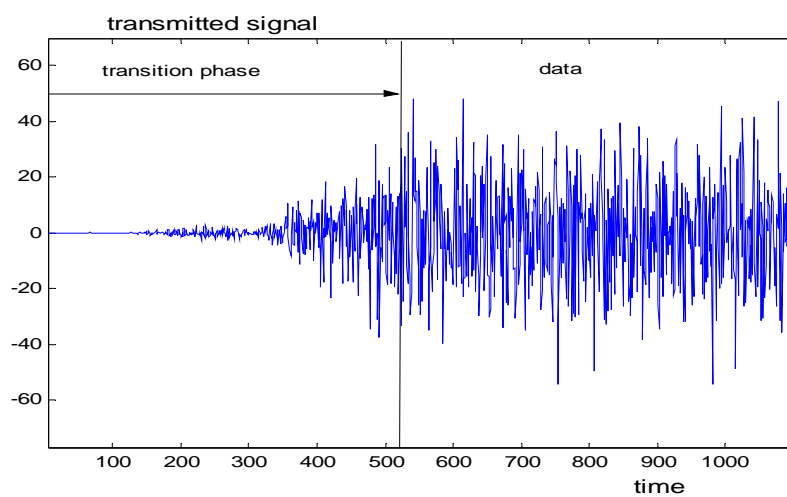


Figure 3-38. Transition phase in the transmitted signal

### 3.6.1 The Memory Preloading Concept

The SFB in the transmitter consists of the inverse FFT and the polyphase network (PPN), as shown in Figure 3-32. The IFFT receives the set of data to be transmitted at each symbol and its output is propagated in the memories of the PPN at the symbol rate. The SFB output,  $y(n)$ , is fed to the channel. Now, if the same set of data is repeated at the input of the synthesis filter bank, the same set of samples appears repeatedly at the output of the inverse FFT and it is stored in the memories of the polyphase network. Then, all the memories of the polyphase network contain the same set of samples. In these conditions, a periodic signal is generated by the SFB and fed to the channel. At the output of the channel, the received signal is periodic and the period is the multicarrier symbol duration. The structure of the analysis filter bank (AFB) in the receiver is shown in Figure 3-33. The received signal  $r(n)$  is fed to the memories of the PPN, which contain the same set of samples each. From the content of these memories, the receiver restores the transmitted data.

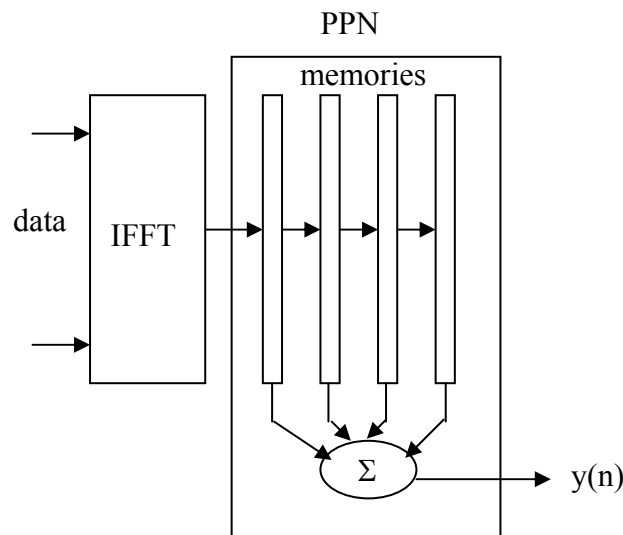


Figure 3-39. Structure of the SFB in the transmitter

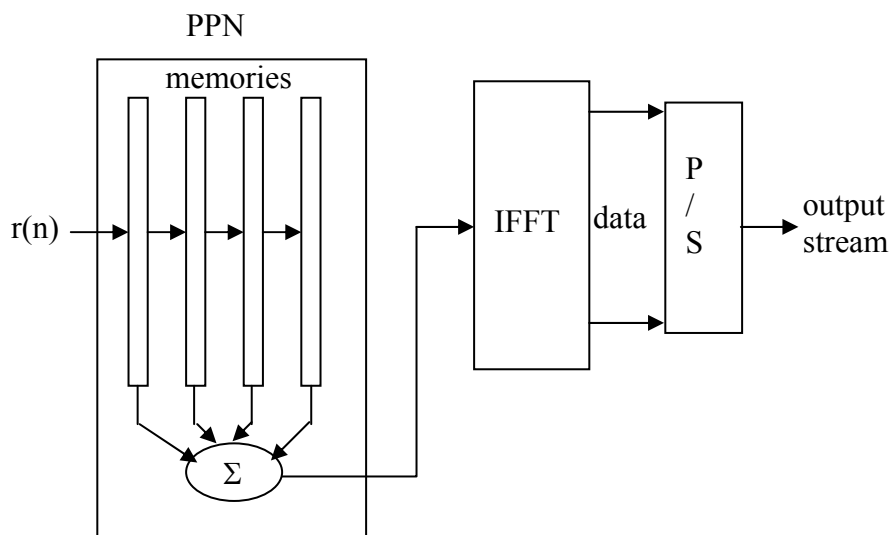


Figure 3-40. Structure of the AFB in the receiver

Now, if a periodic signal  $y(n)$  is to be generated without any transition phase, it is sufficient to preload the memories of the synthesis filter bank with the set of samples produced by the inverse FFT. Then, to demodulate the signal at the output of the channel without the transition phase, it is sufficient to fill the AFB memories with the first received set of samples corresponding to the symbol length. With this preloading technique, implemented in both the transmitter and the receiver, there is no transition phase for the preamble.

As concerns the data, they are not periodic and the transition phase must be kept if the highest level of performance is required. However, this transition phase can be included in the preamble.

When maximum efficiency is sought, the FBMC approach resorts to OQAM modulation, in which the multicarrier symbol rate is the inverse of the sub-channel frequency spacing as in OFDM, but the equivalent of the real and imaginary parts of the complex data are shifted in time by half a symbol duration. The two interleaved sequences obtained are added to form the transmitted signal. In the preamble, there is little to be gained with the interleaved sequence and it is set to zero, which is the equivalent of the BPSK modulation in OFDM.

The preamble symbols and the data symbols appearing in the two interleaved sequences are shown in Figure 3-34, where the preamble symbols are denoted by  $P$  and the data symbols are denoted by  $D_i$  and  $D'_i$ .

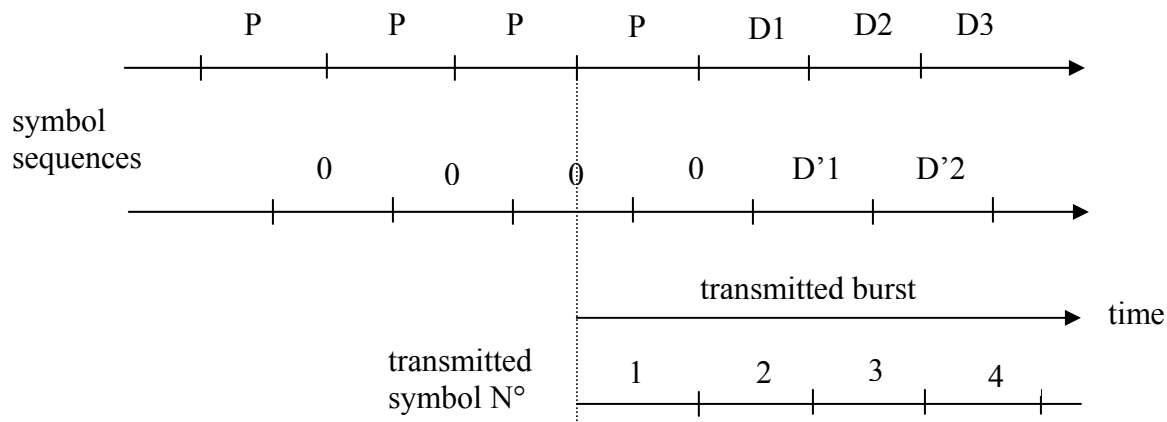


Figure 3-41. Symbol sequences and transmitted burst

According to the memory preloading technique, the latest time for the transmitted burst to start is the last preamble symbol, as shown in the figure. With this scheme, the first  $M$  transmitted samples,  $M$  being the number of samples in the duration of a multicarrier symbol, contain the preamble symbol  $P$  only. The contributions of the preamble and data symbols in the 4 first transmitted sets of  $M$  samples are shown in Figure 3-35.

Next, the first received  $M$  samples are loaded into the memories of the AFB of the receiver to demodulate the first preamble symbol. The demodulation of the first data symbol  $D_1$  takes place when



the  $K$  memories of the receiver AFB contain the symbol D1, i.e. 4 symbols after. The 3 demodulated symbols in-between are preamble symbols.

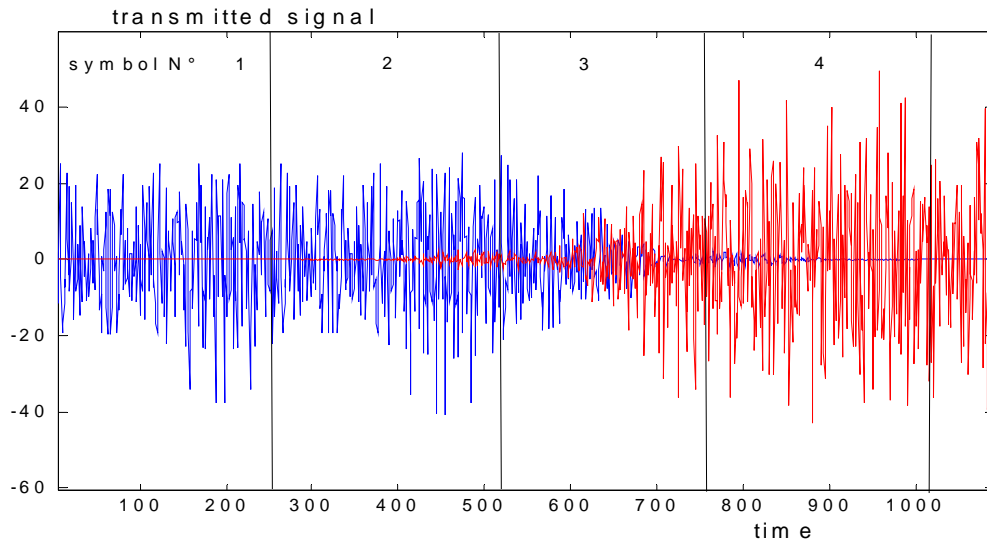


Figure 3-42. First transmitted sets of  $M$  samples ( blue : preamble ; red : data )

An illustration is given in Figure 3-36. In the simulation, the filter bank parameters are as indicated in the above sections, 115 sub-channels out of 128 are used and the corresponding samples at the output of the AFB are serialized, as shown in Figure 3-33, to provide the output data stream and give a global view of the transmission channel. Note that half the transmission capacity is used in the preamble, since the interleaved sequence has been set to zero as indicated above.

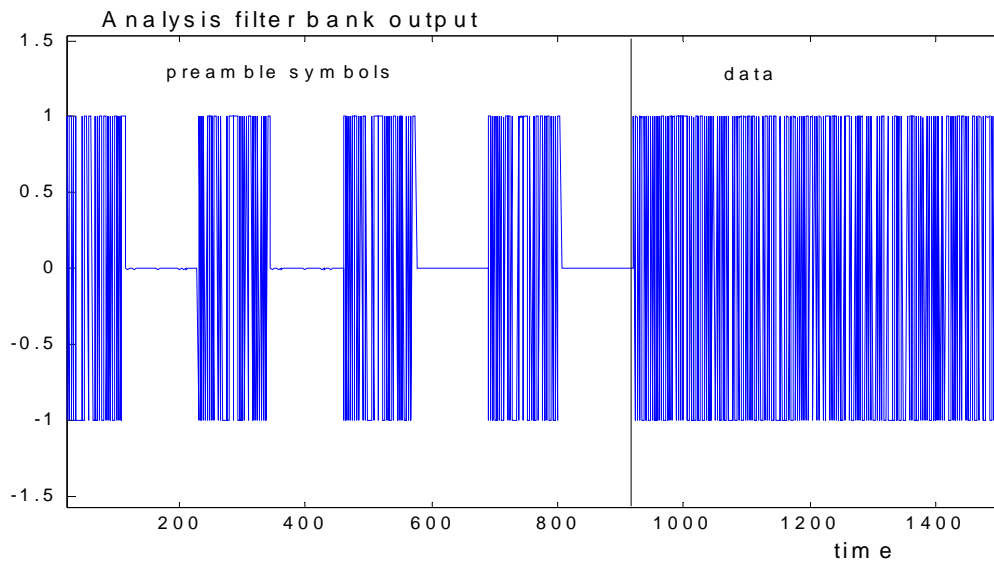


Figure 3-43. Output of the AFB in the receiver after serialization

In this simulation, the SFB and AFB are connected back to back, no transmission channel is present.

### 3.6.2 Transmission Parameter Estimation

As attested by Figure 3-29, Figure 3-31 and Figure 3-35, the first half of the second set of  $M$  transmitted samples contains a very small contribution of the data symbol  $D1$  and, therefore, it can be considered as a repetition of the preamble symbol, which is necessary to estimate the channel parameters.

To begin with, the carrier frequency offset can be measured by conventional techniques, based on the signal repetition mentioned above. Next, the frequency response of the channel is given by the output of the receiver AFB. An illustration is given by simulation. A channel with deep fading and the impulse response shown in Figure 3-37 is inserted between the transmitter and the receiver.

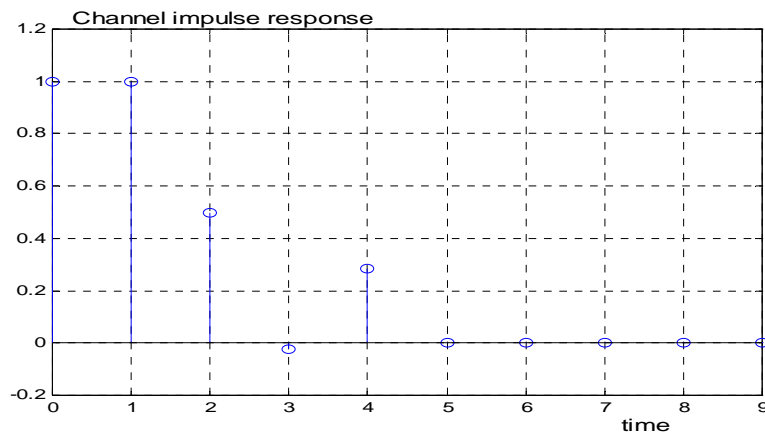


Figure 3-44. Channel impulse response

The discrete Fourier transform of this impulse response is used to equalize the sub-channels at the output of the AFB in the receiver. The signal obtained after serialization is shown in Figure 3-38.

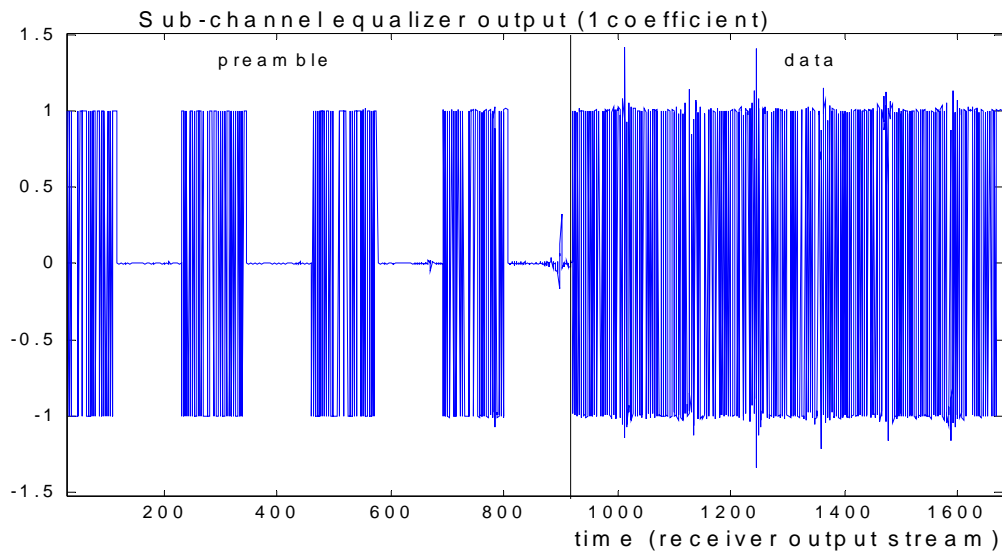


Figure 3-45. Output of the AFB after equalization and serialization

In the first preamble symbol, since there is no superposition of preamble and data signals, the AFB output is perfectly equalized by the FFT of the channel, which means that the filter bank approach and the FFT lead to the same estimation.

The next step is the determination of the timing offset in the receiver, using the outputs of the sub-channels. A simple and efficient technique consists of eliminating the modulation at the output of each sub-channel and, then, computing the inverse FFT, which provides an estimation of the channel impulse response. For example, a delay of 10 samples is introduced at the receiver input and the channel impulse response estimated in this manner is shown in Figure 3-39. The delay is correctly estimated.

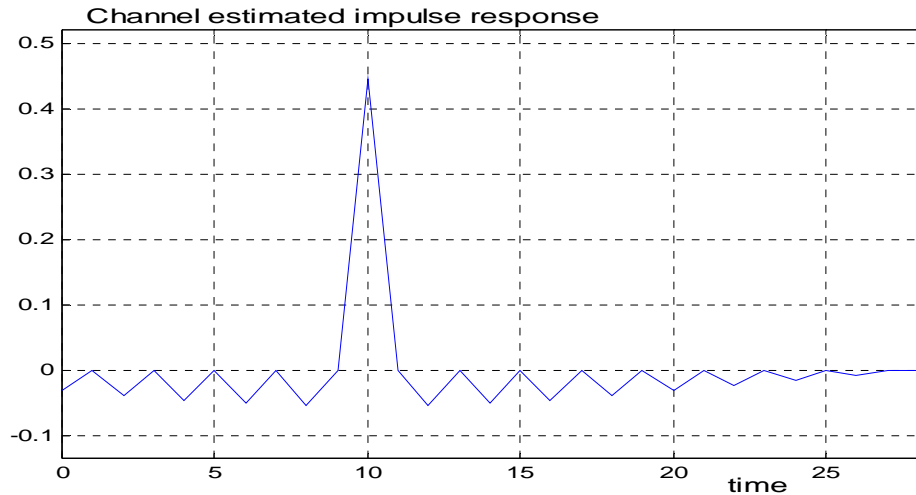


Figure 3-46. Channel impulse response estimation, in the case of a pure delay

Now, the channel impulse response of Figure 3-39 is combined with the delay of 10 samples. The estimated impulse response is shown in Figure 3-40. Again, the delay is correctly estimated.

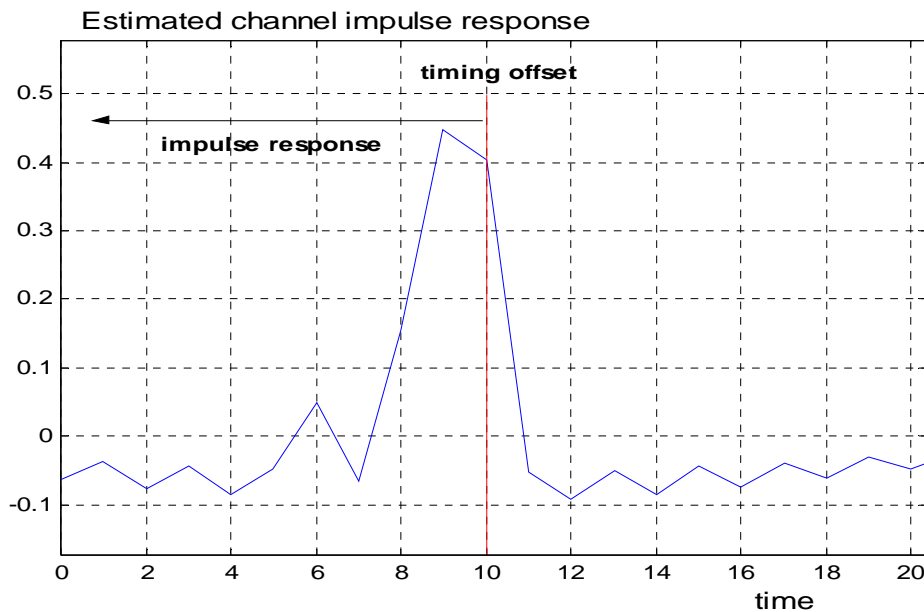


Figure 3-47. Estimation of time offset in the presence of channel distortion.

Then, the robustness to additive white Gaussian noise is investigated. The availability of several preamble symbols in the receiver can be exploited to carry out noise measurements and improve the signal to noise ratio.

The presence of 4 preamble symbols in the receiver is due to the fact that the symbol P is present in 4 consecutive blocks of M samples in the transmitted burst. When noise is added to the channel, the first received set of M samples contains noise samples which are preloaded in the AFB memories along with the useful signal. As a consequence, the noise samples which are added to the preamble symbols at the AFB output are correlated and the expected SNR improvement provided by averaging over 4 blocks is less than 6 dB.

An illustration is given in Figure 3-41. The channel has no distortion, only additive noise and the SNR is 20dB. The measurement of the noise power for each of the 4 preamble symbols yields the following numbers : [0.0074 0.0080 0.0064 0.0076]. After signal averaging, the noise power is 0.0035, which is a reduction of about 3 dB.

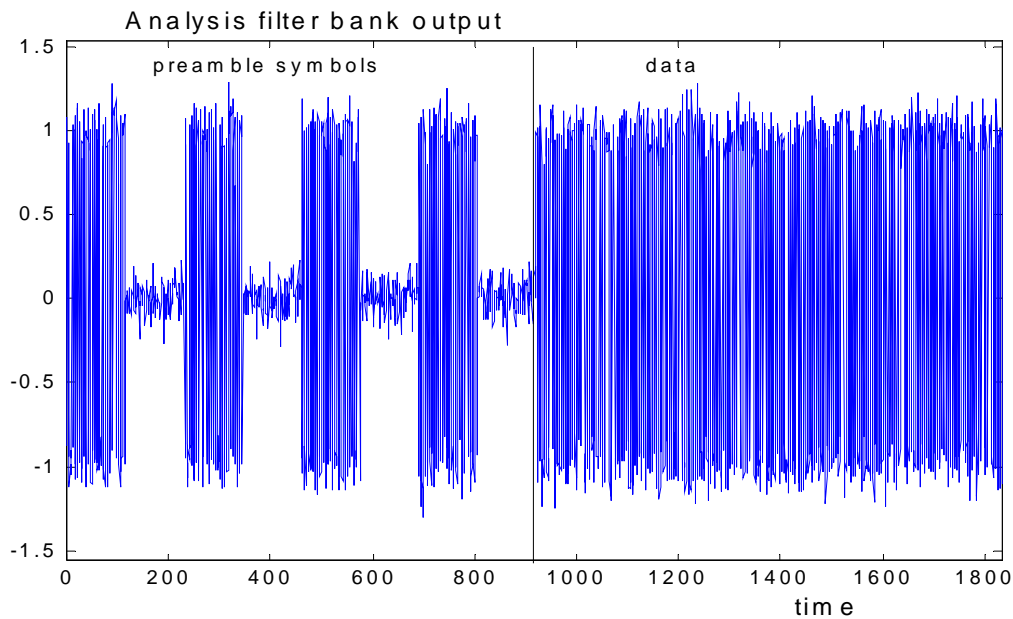


Figure 3-48. Output of the AFB after serialization, with SNR=100 (20 dB)

### 3.6.3 Compatibility with OFDM Transmission Parameter Estimation

The transmitted signal shown in Figure 3-35 can be exploited in the OFDM context, to obtain the channel parameters. By applying an FFT to the first symbol, CFO, channel frequency response and timing offset are derived as above. However, in the second and third initialization symbols, the data signal is present and it impacts the measurements.

### 3.7 Burst structures

The topic of burst truncation, shortening the ‘tails’ of the transmission burst, is of great importance when overheads in time are to be minimized in order to maximize the spectral efficiency of the FBMC modulation. In case of the PHYDYAS reference filter bank with overlapping factor of 4, the transmitted burst waveform is extended by 1.75 FBMC/OQAM symbols, on both sides of the burst, beyond the symbols actually used for data. In WiMAX like system, the length of the downlink burst is typically 20 ... 40 FBMC/OQAM symbols, so including the burst tails fully in the transmission frame would reduce the spectral efficiency by about 9...20 percent. The uplink part of the frame is typically somewhat shorter and maybe be split into a number of independent bursts (due to the use of different types of zones and due to the use of the same subcarriers by different users). Consequently, the burst tails would have even more significant effect in the uplink.

PHYDYAS Deliverable 2.1 [8] included a general study of the effects of burst truncation in filter bank based multicarrier modulation. Raised-cosine window was used to smoothen the truncation effects, and the performance was evaluated in terms of mean-squared error in symbol detection, out-of-band leakage and bandwidth efficiency for different truncation lengths and roll-off values.

In this section, we focus on the burst truncation effects in FBMC systems, considering both uplink and downlink, using the burst truncation model developed in [8]. Also a novel idea of including auxiliary pilots in the heavily truncated part of the burst is investigated. The main focus is on a WiMAX-like case, but also a case with milder burst truncation is considered as an alternative for using full bursts in cognitive radio scenarios.

#### 3.7.1 Burst Truncation in WiMAX-Like FBMC System

We consider here the 10 MHz WiMAX case, with the FFT size of  $M=1024$  and overlapping factor  $K=4$ , leading to impulse response length of  $4096 \pm 1$ .

In D2.1, 432 samples was proposed as the tail length around the uplink/downlink transmission gaps to match the overall frame length. This was found to result in adequately low spectral leakage and interference level in data symbols.

The uplink and downlink bursts are not synchronized at sample level, and there is no need (and it is not possible) to adjust the gap length to be in a specific relation to the FBMC/OQAM symbol length. However in the uplink, the different users’ bursts should be aligned to a common frame structure, and feasible lengths are multiples of half FBMC/OQAM symbol, 512 samples in the case under study. Based on the earlier studies and on the desire to minimize the transmission gaps and burst tails, a natural choice is to choose 512 samples as the length of the burst tail. Then the overall gap in the data symbol stream, consisting of the post-tail of previous burst and pre-tail of the next burst, would be one FBMC/OQAM symbol.

If the truncated tail length is exactly 512 samples, the post-tail of previous burst and pre-tail of next burst would slightly overlap in practice, due to channel delay spread and due to imperfect time synchronization of different uplink users. As an example, a timing difference of  $10 \mu\text{s}$  corresponds to 112 samples. Thus the tail length of 400 samples results in  $20 \mu\text{s}$  gap of zeros between the tails, which is

expected to be sufficient to accommodate worst-case channel delay spread and timing miss-alignment. In the following, we will consider tail lengths of 512 samples and 400 samples as alternatives. It is obvious that some overlap of the tails due to a weak multipath is not very critical. However, to optimize the truncation length, the related parameters should be well-specified and extensive simulation studies would be needed.

One specific idea is that, even though the burst tails are heavily-truncated, it is possible to allocate auxiliary pilots in the corresponding half-FBMC/OQAM symbols. This is possible because there is no need to observe or process the auxiliary pilots themselves, they are only used for forcing the secondary parts of the pilots to zero. This idea can be used for constructing multicarrier preambles, where the pilot symbols have well-controlled secondary parts (in practice zero). A burst structure including such a preamble in the beginning of a data burst is shown in Figure 3-42 (a). Here a pilot is included in every 3<sup>rd</sup> subcarrier, following the WiMAX model (three interlaced pilot sequences can be included in the preamble, one for each sector of a base station). Figure 3-42 (b) shows, for reference, a burst structure where the auxiliary pilots are not included in the truncated part. Figure 3-42 (c) shows one possible burst structure for uplink cases where different users are using the same group of subcarriers in consecutive time slots (e.g., WiMAX uplink PUSC mode with slot rotation). The basic idea here is to reduce the overhead in data transmission rate by moving the auxiliary pilots to burst tails.

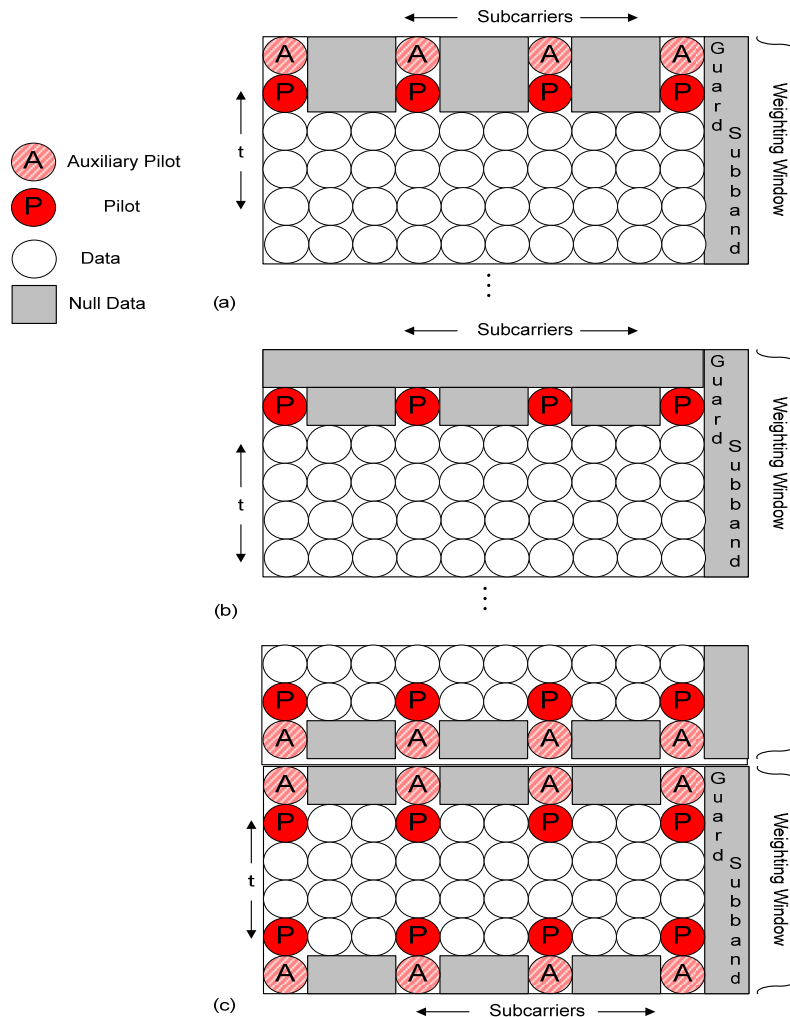


Figure 3-49. Burst structures with tail truncation. (a) Burst model with preamble and auxiliary pilots in pre-tail. (b) Reference burst model with preamble but no auxiliary pilots in pre-tail. (c) Possible uplink burst structure with auxiliary pilots in tails.

### 3.7.2 Burst Truncation in Cognitive Radio Scenarios

It is obvious that in cognitive radio scenarios, the spectral leakage must be very well under control, and the burst tails should be extended compared to what is feasible in the WiMAX like case. Anyway, modest burst truncation can be considered to reduce the overheads due to time-domain gaps between transmission bursts. In the cognitive radio context, we consider the burst tail length of one FBMC/OQAM symbol, i.e., double compared to the WiMAX like case. Table 2-1 shows the overheads in data rate due to the burst tails with the two truncation lengths, in comparison to the full (non-truncated) burst length, for the overlapping factors of  $K=3$  and  $K=4$ .

Table 2-1. Overheads due to burst transitions for  $K=\{3, 4\}$  for full transitions in burst and for transition lengths of one FBMC/OQAM symbol and half FBMC/OQAM symbol. Overhead measured as the number of high-rate samples per transmission burst.

	$K=3$	$K=4$
Full transitions	$2.5M$	$3.5M$
Truncated, long	$2M$	$2M$
Truncated, short	$M$	$M$

### 3.7.3 Numerical Results

We have tested the ideas presented above through simulations. The three cases of Figure 3-42 are included in the study. The average pilot symbol (consisting of primary pilot and auxiliary pilot) power level is 5.5 dB above the average power level of data symbols. 64-QAM modulation is used. The following metrics are observed in the simulations:

- Pilot MSE: Ratio of the average interference energy observed in the primary part of a subcarrier pilot sample normalized to the primary pilot energy. With the used pilot boost, the data MSE is expected to be somewhat higher (but no more than 3 dB) than the pilot MSE.
- Spectral leakage outside the used frequency band measured during the burst tail (i.e., during the truncated auxiliary pilot, when it is present). This is obviously the worst case situation, and an essential criterion when considering the minimum guardband between different non-synchronized FBMC multiplexes. The spectral leakage is measured as the ratio of the average energy of a specific out-of-band (complex) subcarrier sample normalized to the average energy of 64-QAM data symbols.
- Spectral leakage outside the used frequency band measured during the first pilot/data symbol. These results (more specifically the interference level at subcarrier 2) can be used for evaluating the worst-case interference between two different uplink users, having synchronized slot structures, the same power level, and one subcarrier as a guard-band.

***WiMAX-like case***

Figure 3-43 shows the pilot MSE as a function of the truncation parameters using the burst structure of Figure 3-42(a). Figure 3-44 shows the pilot MSE as a function of the raised cosine ratio for overall tail lengths of 400, 512, and 1024 samples, using the burst structures of Figure 3-42(a) and (c). Figure 3-45 shows the spectral leakage effect as a function of the distance from the band edge with selected values of the raised cosine ratio for tail lengths of 400 and 512 and burst structures of Figure 3-42. Figure 3-46 shows the spectral leakage for the burst structures of Figure 3-42 (b) and (c) during the first pilot/data symbols. We can make the following observations:

- It is possible to include the auxiliary pilot in the burst tail while keeping the pilot MSE at a low level.
- There is a clear tradeoff between MSE performance and spectral leakage when adjusting the raised cosine ratio. A relaxed value of MSE, below -30 dB, can be achieved with any RC ratio for the long (1024 samples) tail length, with RC ratios below 0.7 with tail length of 512 and with RC-ratios below 0.3 with tail length of 400.
- The overlapping factor has a small effect on MSE,  $K=3$  resulting in slightly (less than 1 dB) smaller MSE.
- The worst-case spectral leakage with the slot structures of Figure 3-42 (a) and (c) are very similar, as expected.
- Including an auxiliary pilot in the burst tail increases spectral leakage somewhat, especially during the truncated tail and also during the first pilot and data symbols. With the shorter tail lengths, the uplink burst structure of Figure 3-42(c) is reasonable only when the adjacent subcarrier blocks, with 1 subcarrier guard-band, are synchronized.
- When adjusting the raised cosine ratio, there is also a tradeoff between spectral leakage at the second subcarrier and at higher distances.
- With the tail length of 400, it is difficult to find a convenient MSE and spectral leakage behavior simultaneously, at least when considering high-order data modulation, if the target is to use single subcarrier as guardband.
- Table 2-2 shows the MSE and spectral leakage characteristics for selected downlink and uplink cases with RC-ratios resulting in convenient tradoffs. The spectral leakage level at 2<sup>nd</sup> subcarrier from band edge is included as the criterion for uplink cases. Assuming synchronized uplink users, the spectral leakage during the first pilot and data symbols is the essential criterion. The required guardband for the whole FBMC multiplex, in terms of number of subcarriers for -60 dB worst-case spectral leakage level is a common criterion for all cases.

Table 2-2. Characteristics of burst truncation effects in WiMAX-like case with tail length of 512 samples (half FBMC/OQAM symbol).

	Tail RC-ratio	Pilot MSE	Spectral leakage at 2 <sup>nd</sup> subcarrier from band edge during first data/pilots symbols	Required guardband for -60 dB worst-case leakage level (at edge subcarrier during tail)
Downlink with AP during tail	0.6	-34 dB	-	7 subcarriers
Downlink, no	0.6	-34 dB	-	5 subcarriers



AP during tail				
Uplink with AP during tail	0.4	-38 dB	-34 dB	10 subcarriers
Uplink, no AP during tail	0.4	-38 dB	-44 dB	7 subcarriers

In summary, the idea of including auxiliary pilots in the truncated burst tails with the tail length of half of the FBMC/OQAM symbol seems to be possible but requires, especially in the uplink design, careful optimization of all the related aspects. The spectral leakage level at the second subcarrier, -34 dB, leads to tight power control requirements for the uplink users, while the pilot MSE level is even lower than required. In future work, other truncation windows should be considered in order to see if better tradeoff regarding the spectral leakage could be found.

If auxiliary pilots are not included in the truncated burst tails, the spectral leakage at the second subcarrier is significantly relaxed, but also the overhead in data transmission rate is increased in schemes like UL-PUSC with slot rotation. On the other hand, extending the burst tail to full OFDM/OQAM symbol would introduce even bigger overhead.

### *Cognitive radio case*

Considering the use of longer truncated tail length, equal to the length of an FBMC/OQAM symbol, it is seen from Figure 3-44 that the pilot MSE level is small enough with any value of the RC-ratio. From Figure 3-47 we can also see that the spectral leakage is at a much lower level. The RC-ratio of 0.2 gives a good tradeoff between worst-case spectral leakage at the second subcarrier from the band edge and at higher distances. The spectral leakage at the second subcarrier is at the level of -48 dB when auxiliary pilots are included in the burst tails, and at -50 dB when not. The worst-case spectral leakage level of -70 dB is reached using 6 subcarriers as guardband when auxiliary pilots are in the burst tail, and using 5 subcarriers when not.

It should be noted that also the transmitter power amplifier nonlinearity will introduce spectral leakage, which will also compromise the sharpness of the transmitted signal spectrum. In practice, these two effects should be balanced in the design.

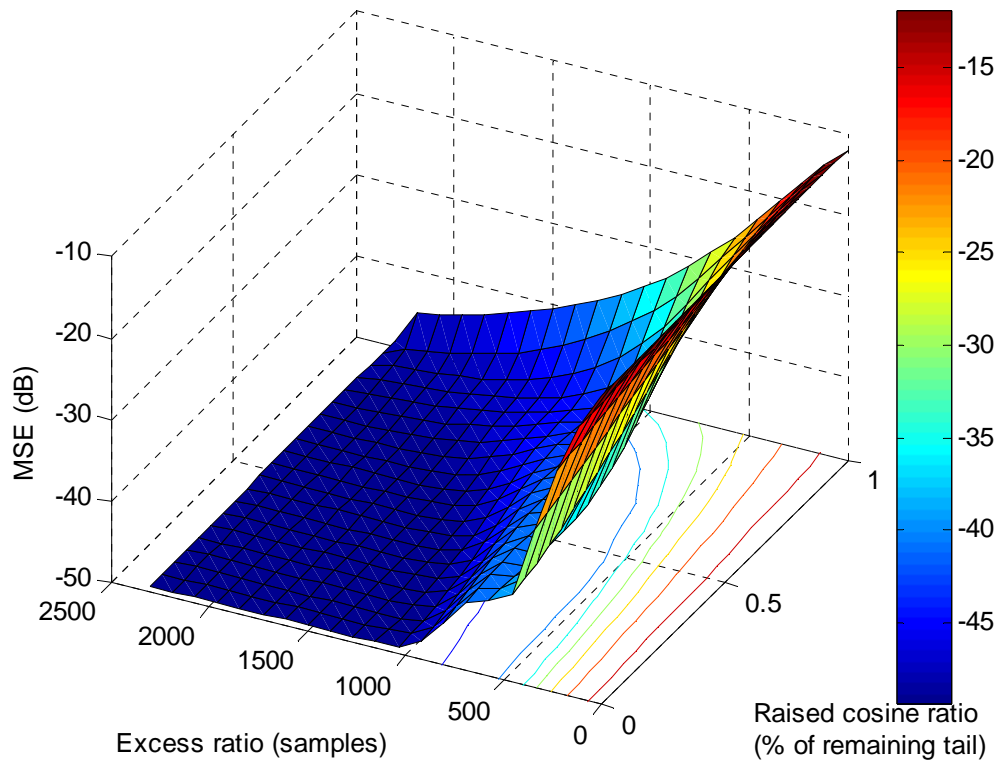


Figure 3-50. Pilot MSE as a function of burst truncation parameters (burst structure of Figure 3-42 (a)).

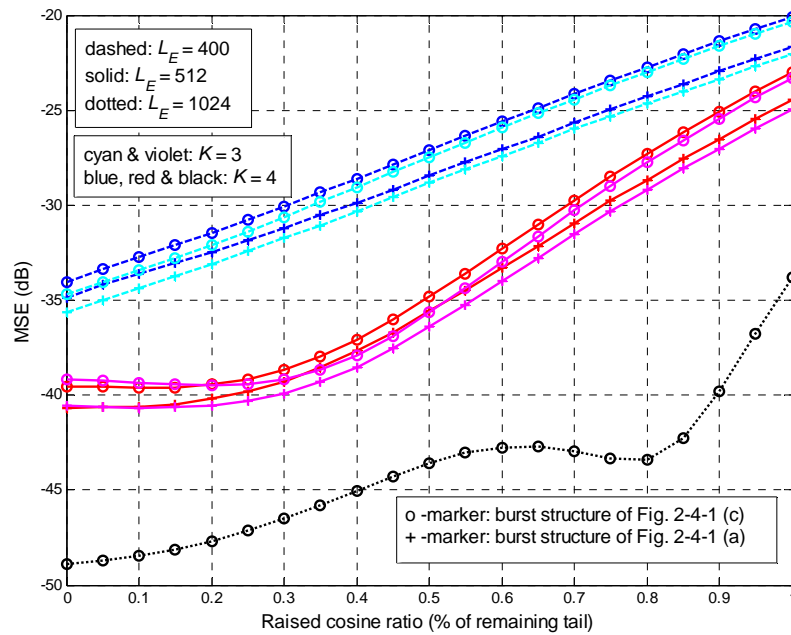


Figure 3-51. Pilot MSE with tail lengths of  $L_E = \{400, 512, 1024\}$  samples.

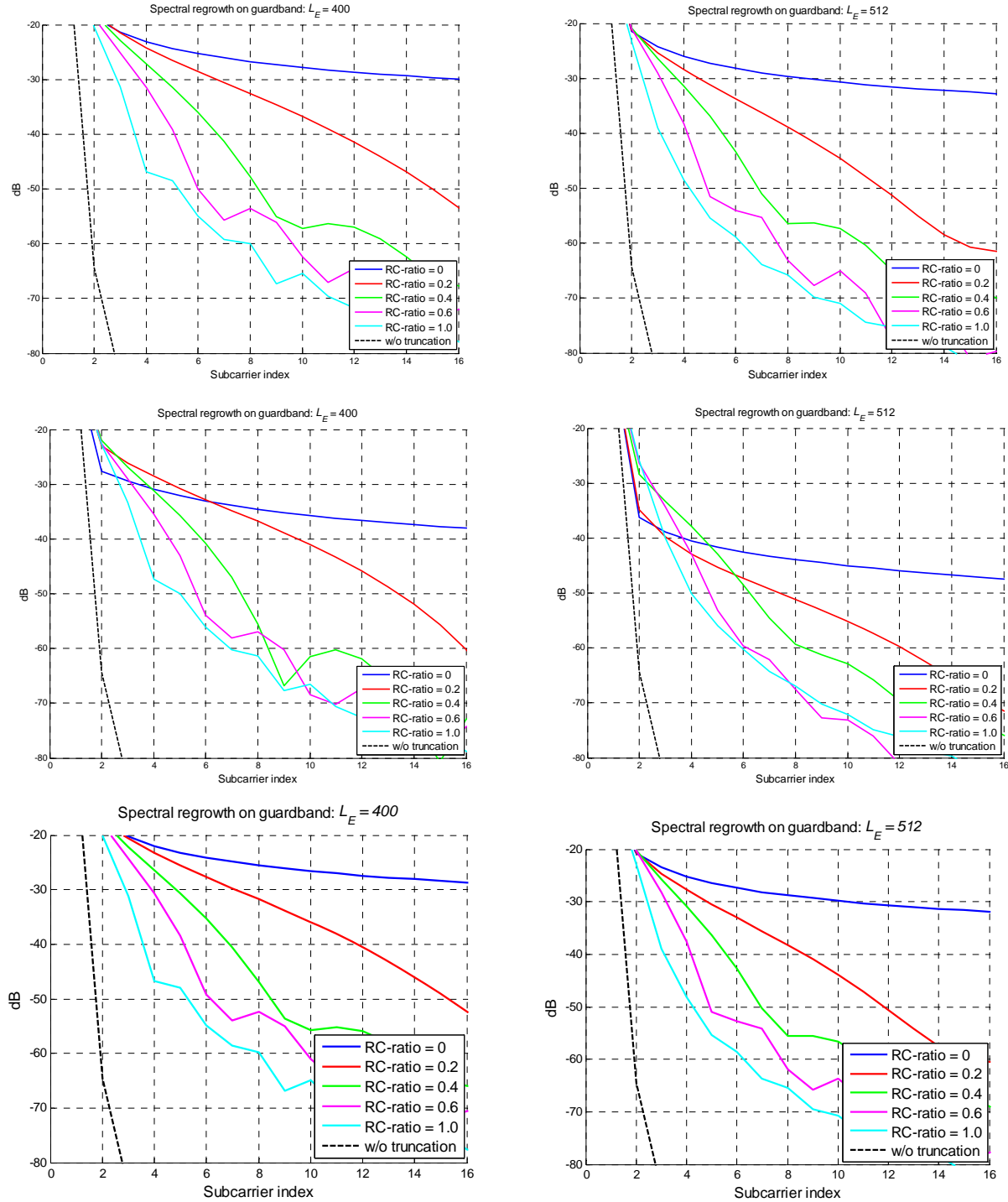


Figure 3-52. Spectral leakage outside the active band (indexes: 0= the last active band subcarrier, 1= the first guard band subcarrier) measured during the truncated auxiliary pilot with tail lengths of  $L_E = 400$  samples (left) and  $L_E = 512$  samples (right). The auxiliary pilot – pilot pair located in the band edge subcarrier. Burst structure as in Figure 3-42(a) (upper), Figure 3-42(b) (middle), and Figure 3-42 (c) (lower).

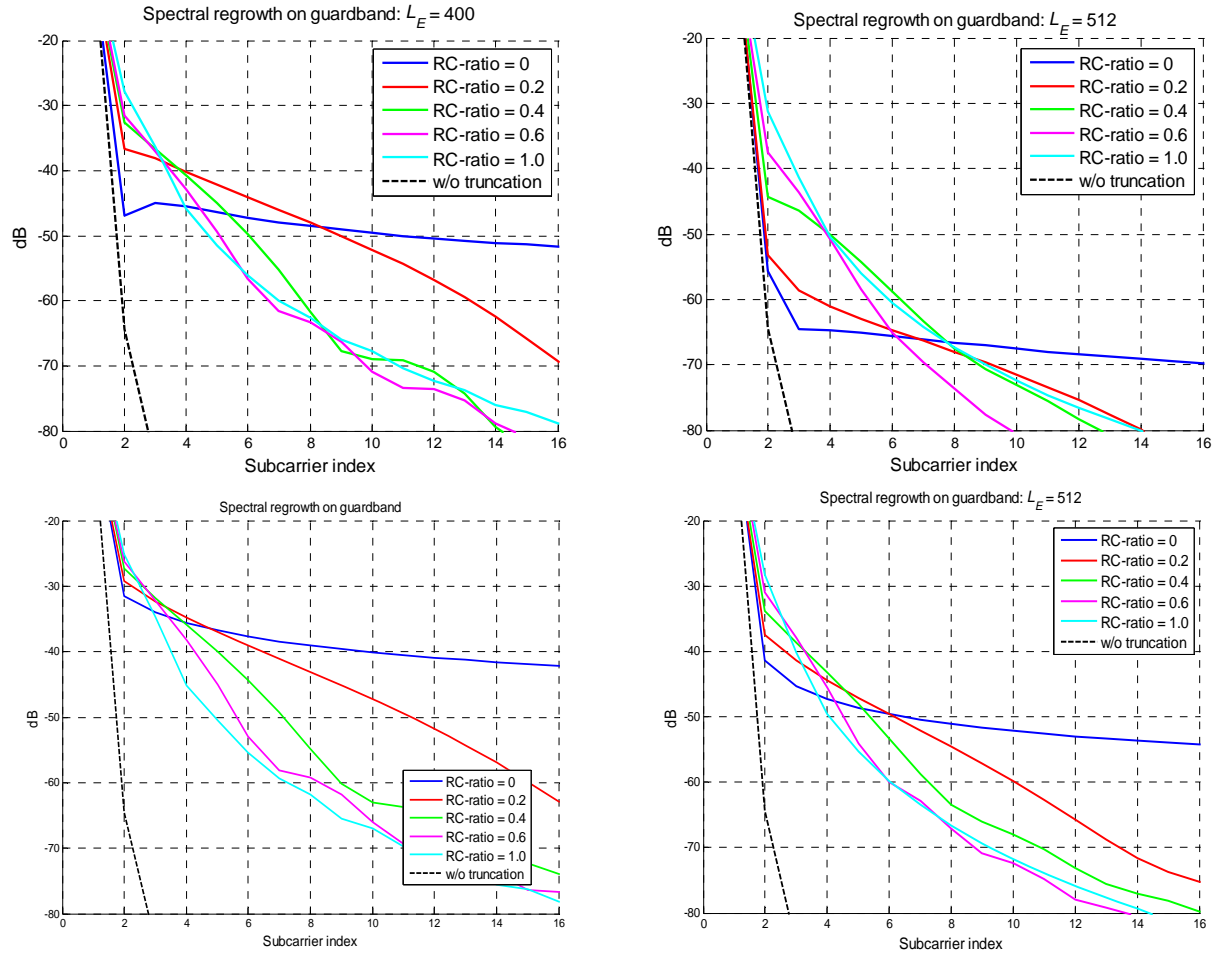


Figure 3-53. Spectral leakage outside the active band (indexes: 0= the last active band subcarrier, 1= the first guard band subcarrier) measured during the primary pilot with tail length of  $L_E = 400$  samples (left) and 512 samples (right). The auxiliary pilot – pilot pair located in the active band edge subcarrier. Burst structure as in Figure 3-42(b) (upper) and Figure 3-42(c) (lower).

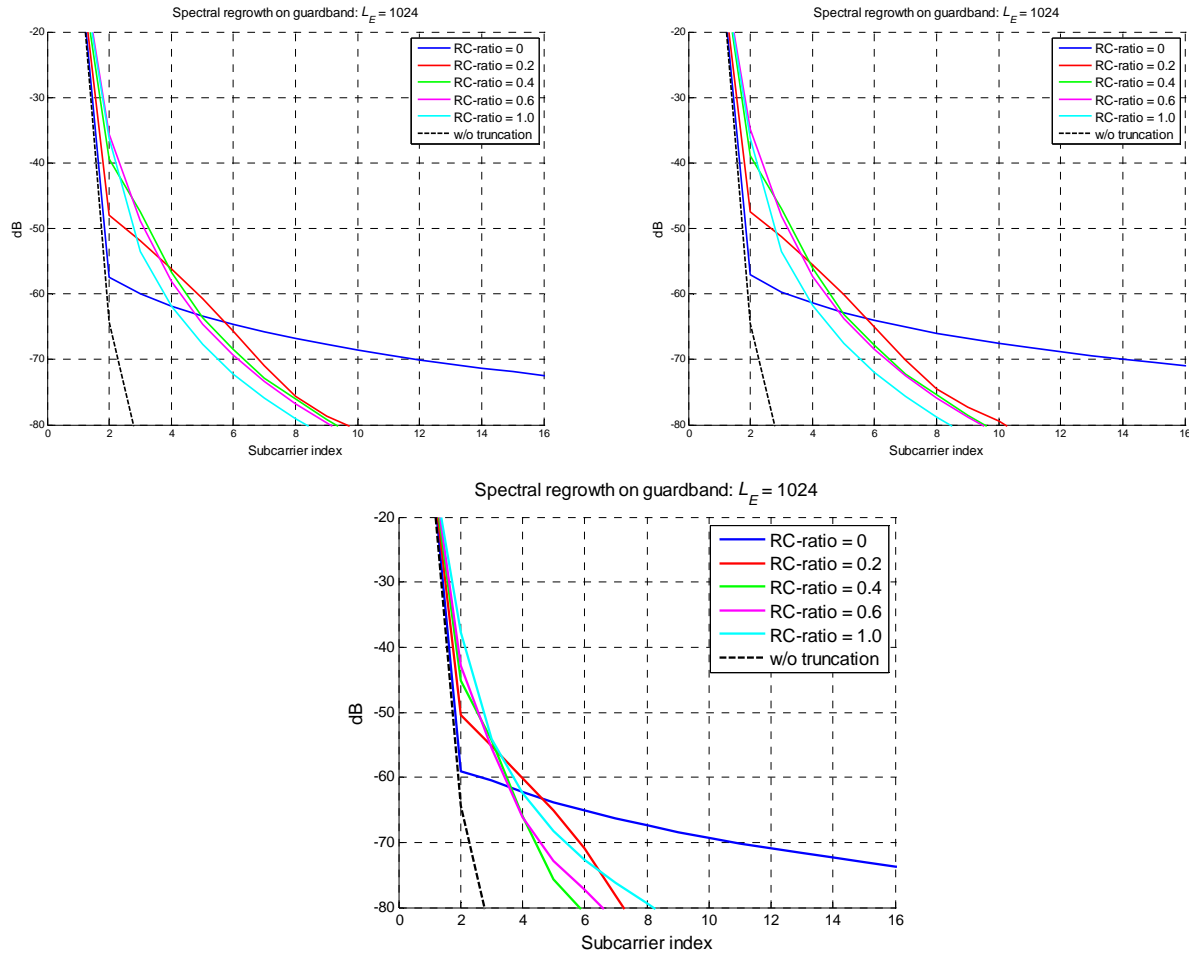


Figure 3-54. Spectral leakage outside the active band (indexes: 0= the last active band subcarrier, 1= the first guard band subcarrier) measured during the truncated auxiliary pilot with tail length of  $L_E = 1024$  samples. The auxiliary pilot – pilot pair located in the active band edge subcarrier. Burst structure as in Figure 3-42(a) (upper-left), Figure 3-42(c) (upper-right) and Figure 3-42(b) (lower).

## 4 Synchronization and Initialization in Uplink

The uplink, in a base station ruled network, is characterized by the fact that the different users are not necessarily synchronized, at least at the beginning of the connection.

### 4.1 Synchronization Based on Preamble

Preamble-based synchronization techniques derived in Section 3.2.2 can also be used in the uplink of a multiuser FBMC system. Specifically, the joint ML phase offset, CFO and symbol timing estimator, exploiting a short known preamble embedded in the burst received from each of  $U$  users, is derived. Since the waveforms of the different users are nearly orthogonal, the ML approach leads to  $U$  different joint estimators. Moreover, for each user the phase estimate is in closed form, and, then, the joint ML symbol timing and CFO estimator requires a two-dimensional maximization procedure. Therefore, a more feasible joint CFO and symbol timing estimator that provides a closed form CFO estimate is derived. The performance of the proposed estimator is assessed via computer simulations both in AWGN and multipath channel.

#### 4.1.1 Joint CFO and symbol Timing Estimator

In this section we derive the joint ML phase, CFO and symbol timing estimator for the uplink of a multiuser FBMC, by exploiting the transmission of a training sequence, embedded in the transmitted burst. In particular, let us consider a preamble of  $N_{TR}$  FBMC symbols, the training sequence of the  $i$ th user, is given by

$$z_i[m] = \sum_{k \in M_u^i} \sum_{n=0}^{2N_{TR}-1} d_{k,n} \theta_{k,n} \beta_{k,n} p[m - nM/2] e^{j \frac{2\pi}{M} km}. \quad (80)$$

The received signal in AWGN channel, when the information-bearing signal  $s_i[m]$  of the  $i$ th user presents a timing offset  $\tau_i$ , a CFO  $\varepsilon_i$ , a carrier phase offset  $\phi_i$  and an attenuation  $|c_i|$ , can be expressed as

$$r[m] = \sum_{i=1}^U e^{j2\pi \left[ \frac{k\varepsilon_i + \phi_i}{M} \right]} |c_i| s_i[m - \tau_i / T_s] + n[m]. \quad (81)$$

By considering an observations window of length  $M\eta$  samples containing the non-zero support of the preamble received from each user, the likelihood function in AWGN channel for the unknown parameters  $\{\tau_i\}_{i=1}^U$ ,  $\{\varepsilon_i\}_{i=1}^U$  and  $\{\phi_i\}_{i=1}^U$  is given by (up to an irrelevant multiplicative factor)

$$\Lambda(\underline{\tilde{\tau}}, \underline{\tilde{\varepsilon}}, \underline{\tilde{\phi}}) = \exp \left\{ -\frac{T_s}{N_0} \sum_{m=0}^{M\eta-1} \left| r[m] - \sum_{i=1}^U |c_i| e^{j \frac{2\pi \tilde{\varepsilon}_i}{M} m} e^{j2\pi \tilde{\phi}_i} \tilde{z}_i[m - \tilde{\tau}_i / T_s] \right|^2 \right\} \quad (82)$$

where  $\underline{\tilde{\tau}} = (\tau_1, \tau_2, \dots, \tau_U)$ ,  $\underline{\tilde{\varepsilon}} = (\varepsilon_1, \varepsilon_2, \dots, \varepsilon_U)$  and  $\underline{\tilde{\phi}} = (\phi_1, \phi_2, \dots, \phi_U)$ .

By replacing (80) in (82) and dropping irrelevant multiplicative and additive factors we get

$$\ln \Lambda(\underline{\tilde{\tau}}, \underline{\tilde{\varepsilon}}, \underline{\tilde{\phi}}) = \sum_{i=1}^U \text{Re} \left[ |c_i| e^{-j2\pi \tilde{\phi}_i} \gamma(\tilde{\tau}_i, \tilde{\varepsilon}_i) \right] \quad (83)$$

where

$$\gamma(\tilde{\tau}_i, \tilde{\varepsilon}_i) = \sum_{m=0}^{\eta M-1} r[m] \tilde{z}[m - \tilde{\tau}_i / T_s]^* e^{-j \frac{2\pi \tilde{\varepsilon}_i}{M} m}. \quad (84)$$

In particular, in the derivation of (83), we have neglected the quantity

$$\sum_{m=0}^{\eta M-1} \left| \sum_{i=1}^U |c_i| e^{j2\pi \tilde{\phi}_i} e^{j \frac{2\pi}{M} \tilde{\varepsilon}_i m} \tilde{z}_i \left[ m - \tilde{\tau}_i / T_s \right] \right|^2 = C_1 + C_2 \quad (85)$$

since it is weakly dependent on the parameters to be estimated under the assumption that the observations window contains the non-zero support of the preamble received from each user and that the CFO of each user is sufficiently small. In fact, in this case the first contribution in the RHS of (85)

$$C_1 = \sum_{i=1}^U |c_i|^2 \sum_{m=0}^{\eta M-1} \left| \tilde{z}_i \left[ m - \tilde{\tau}_i / T_s \right] \right|^2 \quad (86)$$

is independent of the phase offset and the CFO, and slightly dependent of the symbol timing, while the second term in the RHS of (85)

$$C_2 = 2 \operatorname{Re} \left\{ \sum_{i_1=1}^U \sum_{i_2=1}^{U-i_1} \sum_{m=0}^{\eta M-1} |c_{i_1}| |c_{(i_1+i_2)}| e^{j(\tilde{\phi}_{i_1} - \tilde{\phi}_{(i_1+i_2)})} e^{j \frac{2\pi}{M} (\tilde{\varepsilon}_{i_1} - \tilde{\varepsilon}_{(i_1+i_2)}) m} \tilde{z}_{i_1} \left[ m - \tilde{\tau}_{i_1} / T_s \right] \tilde{z}_{(i_1+i_2)} \left[ m - \tilde{\tau}_{(i_1+i_2)} / T_s \right]^* \right\} \quad (87)$$

related to the scalar product between the signal of the different users, is negligible since the spectra of these signals essentially don't overlap. The joint ML CFO, phase offset and symbol timing is given by

$$\hat{\phi}_{i_{ML}} = \frac{1}{2\pi} \angle \{ \gamma(\tilde{\tau}_i, \tilde{\varepsilon}_i) \}, i = 1, \dots, U, \quad (88)$$

and, moreover,

$$(\hat{\tau}_{i_{ML}}, \hat{\varepsilon}_{i_{ML}}) = \arg \max_{(\tilde{\tau}_i, \tilde{\varepsilon}_i)} [\gamma(\tilde{\tau}_i, \tilde{\varepsilon}_i)], \quad i = 1, \dots, U. \quad (89)$$

As in the case of the ML estimator derived in Section 3.2.2, the solution of the considered two-dimensional maximization problem can be found only by numerical methods. Therefore, to obtain a more feasible synchronization scheme that requires two one-dimensional maximization procedures, let us suppose that the CFO of the  $i$ th user is sufficiently small that within a time  $\Delta Q$  comparable with the length of the prototype filter, it results that  $e^{-j \frac{2\pi}{M} \tilde{\varepsilon}_i \Delta Q} \approx 1$ , into the case of a training sequence of total length  $N_{TR} = 1$  it follows that

$$\begin{aligned}
& \sum_{m=0}^{\eta M-1} r[m] \tilde{z}_i[m - \tilde{\tau}_i / T_s]^* e^{-j \frac{2\pi \tilde{\epsilon}_i}{M} m} \\
&= \sum_{n=0}^1 \sum_{k \in M_u^i} d_{k,n} (\theta_{k,n} \beta_{k,n})^* \underbrace{\sum_{m=0}^{\eta M-1} r[m] p[m - nM / 2 - \tilde{\tau}_i / T_s] e^{j \frac{2\pi}{T} k (\tilde{\tau}_i - m)} e^{-j \frac{2\pi \tilde{\epsilon}_i}{M} m}}_{w_n^{(k)}(\tilde{\epsilon}_i, \tilde{\tau}_i)} \\
&\approx \sum_{n=0}^1 \sum_{k \in M_u^i} d_{k,n} (\theta_{k,n} \beta_{k,n})^* w_n^{(k)}(0, \tilde{\tau}_i) e^{-j \pi \tilde{\epsilon}_i n}
\end{aligned} \tag{90}$$

then

$$\gamma(\tilde{\epsilon}_i, \tilde{\tau}_i) = \underbrace{\sum_{k \in M_u^i} d_{k,0} \theta_{k,0}^* \beta_{k,0}^* w_0^{(k)}(0, \tilde{\tau}_i)}_{A(\tilde{\tau}_i)} + e^{-j \pi \tilde{\epsilon}_i} \underbrace{\sum_{k \in M_u} d_{k,1} \theta_{k,1}^* \beta_{k,1}^* w_1^{(k)}(0, \tilde{\tau}_i)}_{B(\tilde{\tau}_i)} \tag{91}$$

Therefore, the joint ML estimator in (89) can be simplified as

$$\hat{\tau}_i = \arg \max_{\tilde{\tau}_i} [A(\tilde{\tau}_i) + B(\tilde{\tau}_i)] \quad i = 1, \dots, U \tag{92}$$

$$\hat{\epsilon}_i(\hat{\tau}_i) = \frac{1}{\pi} \angle \{ A^*(\hat{\tau}_i) B(\hat{\tau}_i) \} \quad i = 1, \dots, U. \tag{93}$$

#### 4.1.2 Numerical Results

In this section the performance of the proposed AML estimator reported in (92) and in (93) is assessed via computer simulations. A number of  $10^3$  Monte Carlo trials has been performed under the following conditions:

- the value of the timing offset and the CFO are uniformly distributed in  $[-0.5, 0.5)$  and  $T_s \{-M/2, M/2\}$ , respectively. In particular, the symbol timing is supposed to be an integer multiple of the sampling period  $T_s$ ;
- the size of the set of subcarriers is  $M=1024$  while the number of users is  $U=4$  and  $M_u^i=256$   $i = 1, \dots, 4$  indicates the number of subcarriers per user;
- two different kinds of allocation schemes, blockwise and interleaved are considered In the blockwise scheme, a block of  $M_u^i=256$   $i = 1, \dots, 4$  adjacent subcarriers is assigned to the  $i$ th user. On the contrary in the interleaved scheme, group of adjacent subcarriers are allocated to different users;
- the preamble is made up of  $N_{TR} = 1$  FBMC symbols;
- numerical results have been obtained by considering two different scenarios: AWGN channel and multipath channel modelled using the Vehicular-A channel model of ITU-R. Moreover, the channel is fixed in each run but it is independent from one run to another.

In Figure 4-1 and Figure 4-2, it is reported the BER obtained by exploiting the proposed joint symbol timing and CFO AML algorithm and that observed in the case of perfect synchronization. The results show that, both in AWGN and multipath channel, the BER obtained by exploiting the proposed estimator is nearly coincident with that obtained in the case of perfect synchronization in the whole range of considered SNR values and for both allocation schemes.



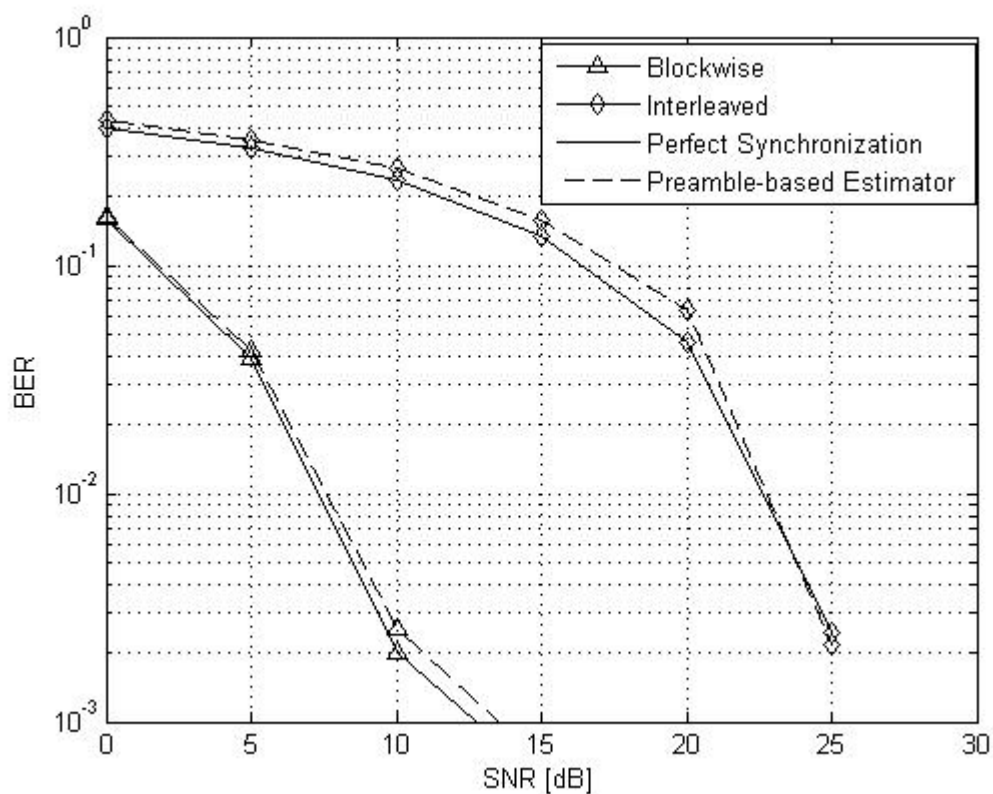


Figure 4-1. BER of the considered estimator in AWGN channel.

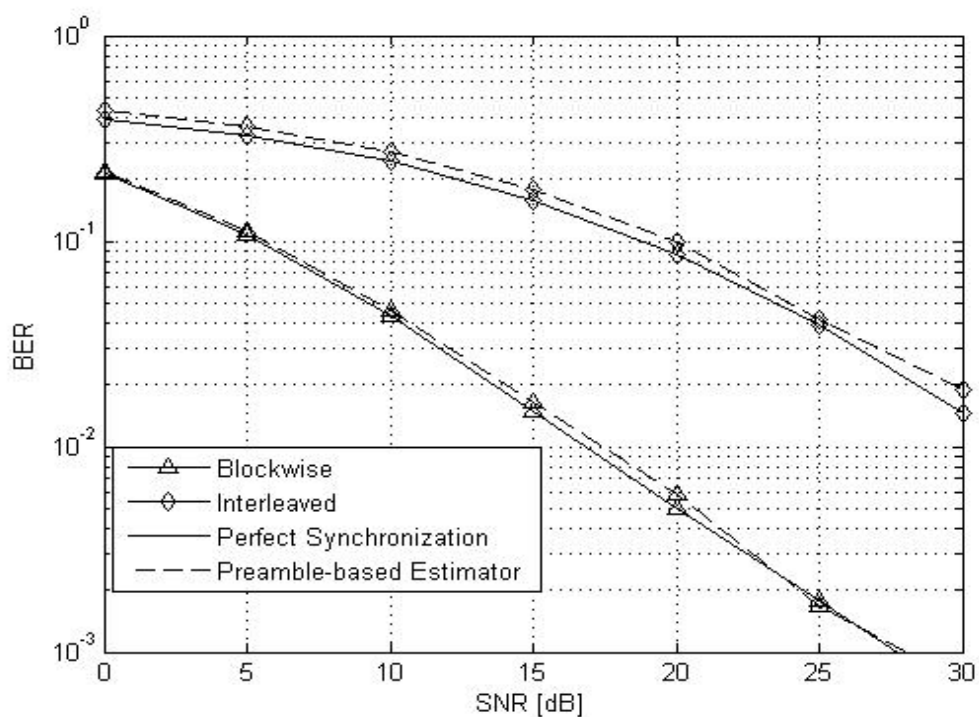


Figure 4-2. BER of the considered estimator in multipath channel.

## 4.2 Synchronization Based on Scattered Pilots

Here we consider the application of the scattered pilot based methods of Section 3.4 to the uplink synchronization, now utilizing the pilots of a group of subcarriers instead of utilizing pilots in all the active subcarriers of the FBMC multiplex.

One fundamental difference, in comparison to downlink, is that the base-station receiver receives different groups of subcarriers from multiple independent transmitters which are not perfectly synchronized. In the presence of any differences in the FTD or CFO values, it is not possible to synchronize the receiver AFB perfectly to all the uplink users simultaneously. We have seen in Section 3.4 that CFO and FTD compensation methods are useful for the downlink synchronization, but in the uplink they are in an even more important role. Effective compensation methods, exploiting the frequency domain separation of the unsynchronized users, could be helpful in developing simplified, effective overall synchronization schemes for cognitive radios.

The possibilities of CFO compensation are obviously limited to a fraction of the subcarrier spacing, depending on the modulation order. On the other hand, there are no fundamental limitations to compensate any fractional timing offset. The FTD compensator basically needs to implement a fractional time delay for the subcarrier sample sequences. The interpolation based approach has been addressed in PHYDYAS Deliverable 3.1 [8]. Also, it was shown in [8] how the multitap subcarrier equalizers can be used for compensating the FTD. Here we utilize 3-tap subcarrier equalizer for this purpose. Section 4.4 studies more broadly the performance of multitap subcarrier equalizers in compensating the timing offsets.

Since the definition of the UL-PUSC is still open in FBMC, we selected the UL-AMC23 configuration and tested transmissions bursts utilizing different numbers of adjacent (in time and frequency domain) slots. Each AMC23 slot consists of 18 consecutive subcarriers and 3 MC symbols, according to WiMAX specifications and as can be seen in [4] and [8]. The CFO and FTD compensation ranges are somewhat smaller than in the above study due to the bigger spacing between pilots within the same subcarrier or MC symbol, as can be seen in the following results. Originally, three transmission sizes were considered: 4x2, 8x4 and 16x8 slots. However, in the quasi-static channel model of these simulations, the performance of 8x4 lies between the other extremes and is not shown here for the sake of readability of the figures.

Figure 4-3 presents the BER performance with respect to the CFO and the FTD for the 4-QAM modulation at similar conditions as in the previous set of simulations. The results for different transmission burst sizes are presented, including CFO amplitude correction by the 3-tap equalizer and 1 iteration at the synchronization stage. The BER results without the iteration and CFO amplitude compensation are not included because they are very similar to the depicted performances. It can be seen that the strongest penalty in performance for the smaller transmission burst comes when increasing the FTD. In the quasi-static channel, the performance with respect to CFO is very close for both sizes.

The following two figures show sections of Figure 4-3 at fixed CFO and at fixed FTD values, respectively. Only in the figure presenting the BER performance as a function of the CFO (with fixed FTD) the results for the simpler synchronization are included to show the limited performance improvement around 15% CFO.

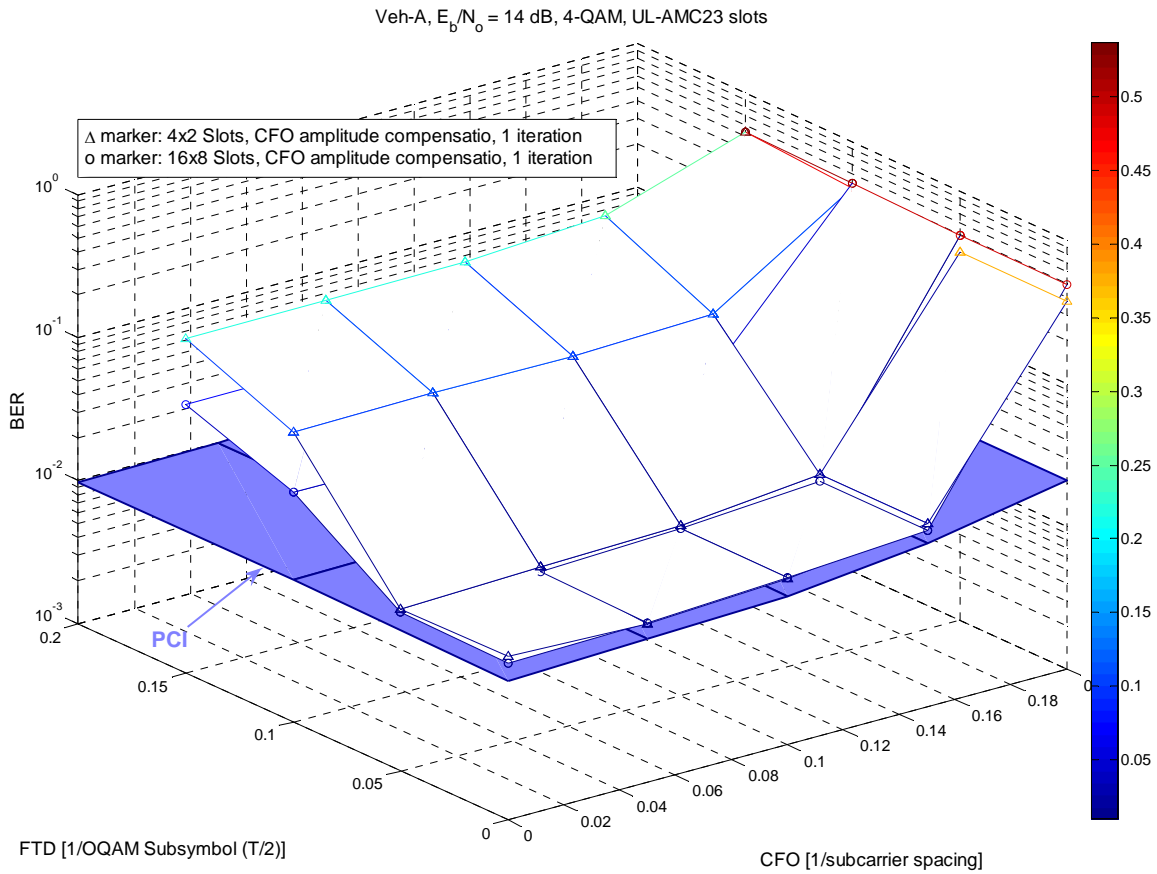


Figure 4-3. BER performance vs. CFO and FTD for uplink transmission of 16x8 and 4x2 AMC23 slots in Vehicular-A channel at  $E_b/N_o = 14$  dB using 4-QAM. Synchronization performed with CFO amplitude compensation in the 3-tap equalizer and 1 synchronization iteration.

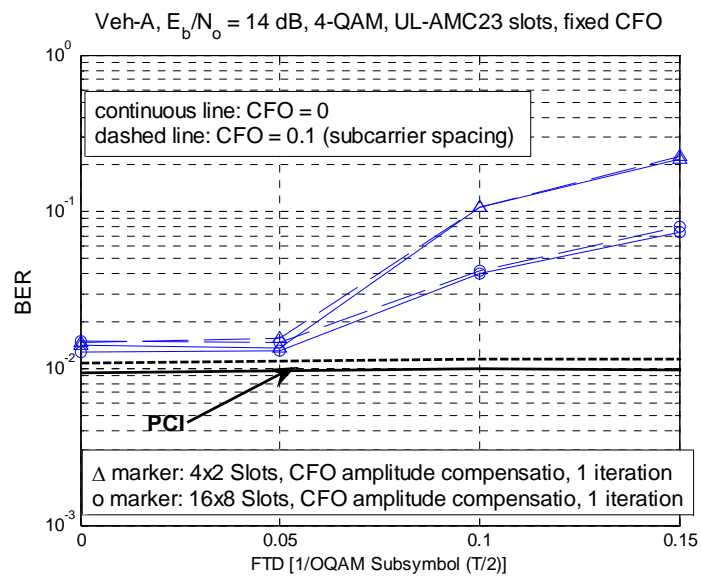


Figure 4-4. BER performance vs. FTD at CFO = 0 and 10% of subcarrier spacing for an uplink transmission of 16x8 and 4x2 AMC23 slots in Vehicular-A channel at  $E_b/N_o = 14$  dB using 4-QAM. Synchronization performed with CFO amplitude compensation in the 3-tap equalizer and 1 synchronization iteration.

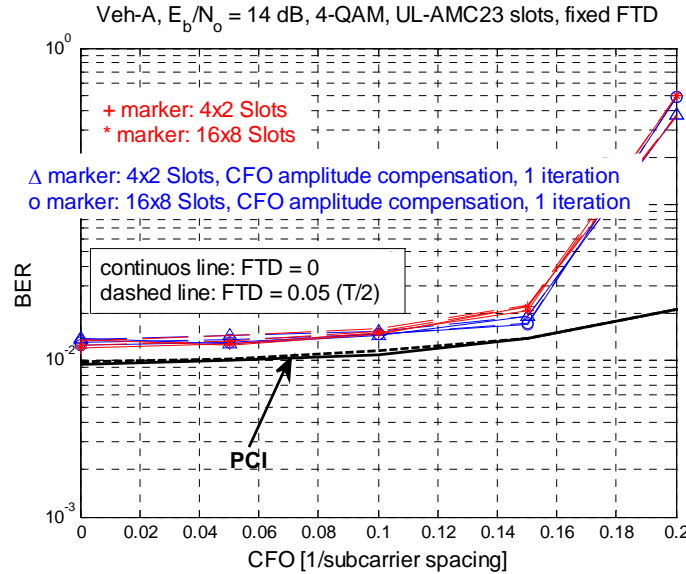


Figure 4-5. BER performance vs. CFO at FTD = 0 and 5% of FBMC/OQAM subsymbol ( $T/2$ ) for an uplink transmission of 16x8 and 4x2 AMC23 slots in Vehicular-A channel at  $E_b/N_o = 14$  dB using 4-QAM. Different synchronization options.

The following results present the root mean squared errors in the FTD and CFO estimates. Figure 4-6 shows the RMS error in FTD estimation as a function of both, FTD and CFO. The behaviour for both transmission burst sizes is very similar, so the degradation in the BER performance is more likely to be due to worse channel interpolation rather than due to the FTD estimation. Figure 4-7 shows a graph of the RMS in the CFO estimation. Here we can see that there is a larger difference in the estimates, depending on the size and also on the choice of the synchronization scheme. Interestingly, in 4-QAM, the CFO amplitude compensation and iteration does worsen slightly the estimation performance. However, the difference between the synchronization methods is quantitatively small. The difference between the burst sizes is larger and it partially explains the BER performance difference.

These results show that the performance of the UL-AMC23 slots is similar to the performance of the short frame using all the carriers, within the smaller operating range due to the greater distance between pilots. It is expected that the FTD range can be enhanced by relocating the phase of pilots of different MC symbols onto one MC symbol, taking into account the estimated CFO. This would reduce the gaps between pilots and permit a wider time delay.

Next we present similar BER performance results for 64-QAM at  $E_b/N_o = 20$  dB. Since this higher order modulation is more sensitive to distortion, the CFO and FTD range within which the performance is acceptable is reduced when compared to the 4-QAM case. Figure 4-10 presents the BER performance for two different transmission burst sizes and also for two synchronization options. With 64-QAM the gain of performing the amplitude compensation for the CFO with the 3-tap equalizer followed by an iteration of the synchronization block is clearly visible. Especially in the CFO direction the difference is

notable. Figure 4-11 and Figure 4-12 show the sections for fixed CFO and FTD, respectively. The RMS errors in CFO and FTD estimation behave similarly as in the results for 4-QAM, but with different quantitative values due to the different effective operating SNR. Figure 4-8 and Figure 4-9 show sections of Figure 4-6 and Figure 4-7, respectively, to improve the readability of the results.

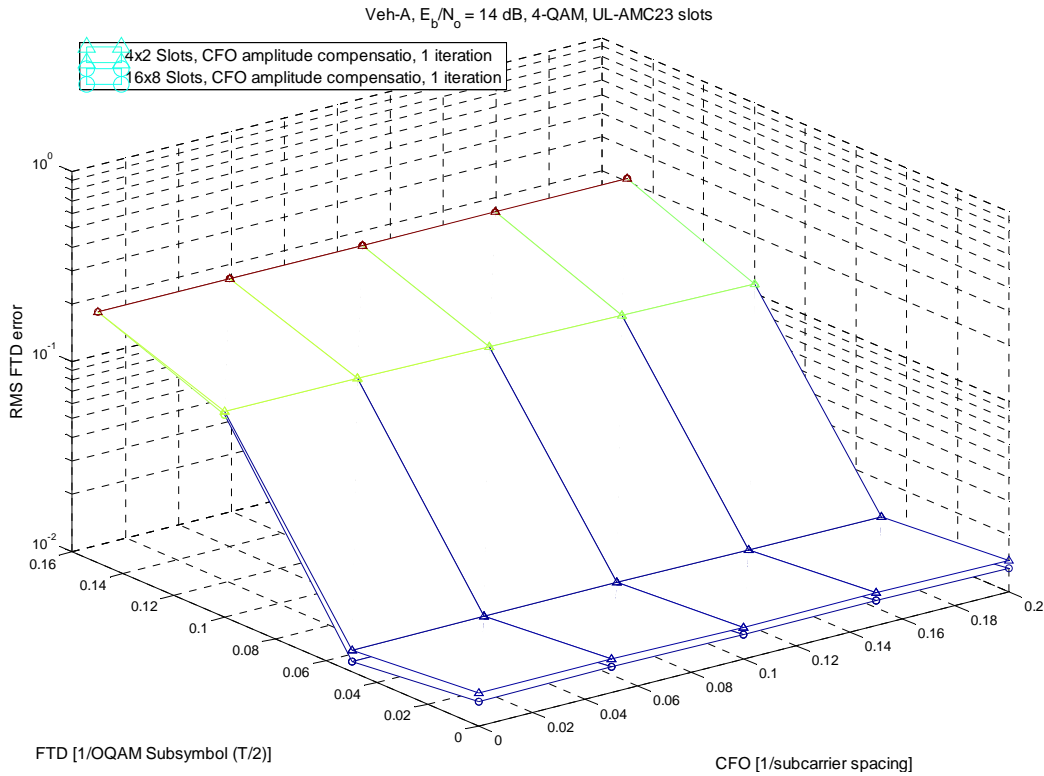


Figure 4-6. RMS error in FTD estimation in an uplink transmission of 16x8 and 4x2 AMC23 slots in Vehicular-A channel at  $E_b / N_o = 14$  dB using 4-QAM. Synchronization performed with CFO amplitude compensation in the 3-tap equalizer and 1 synchronization iteration.

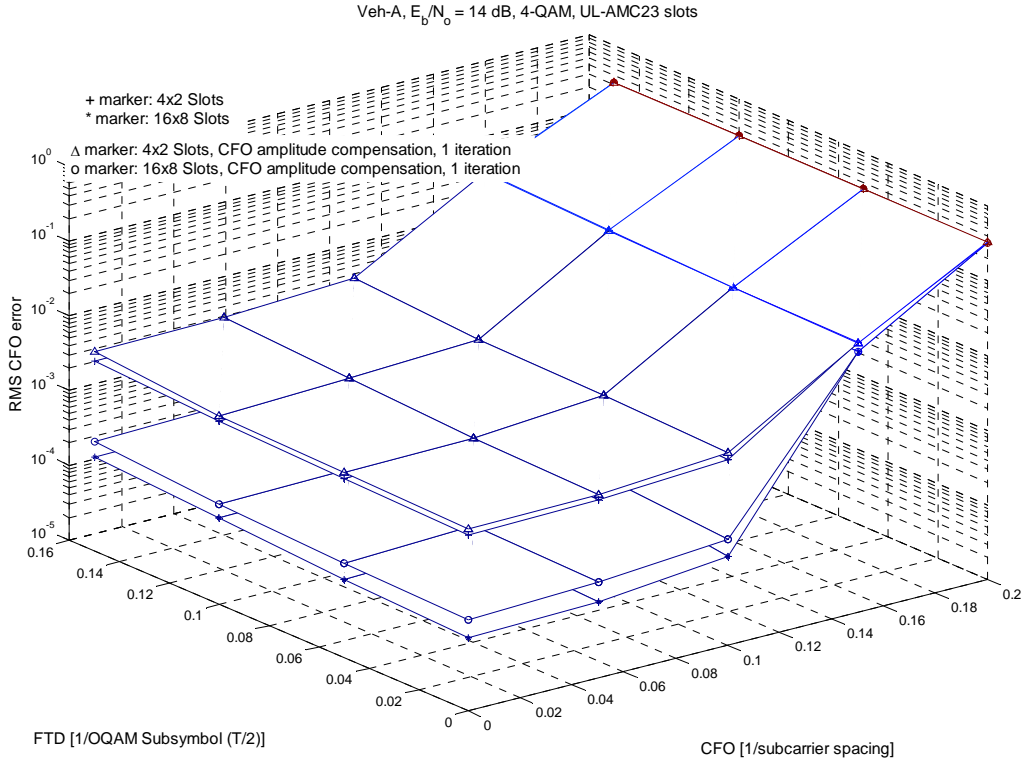


Figure 4-7. RMS error in CFO estimation in an uplink transmission of 16x8 and 4x2 AMC23 slots in Vehicular-A channel at  $E_b / N_o = 14$  dB using 4-QAM. Different synchronization options.

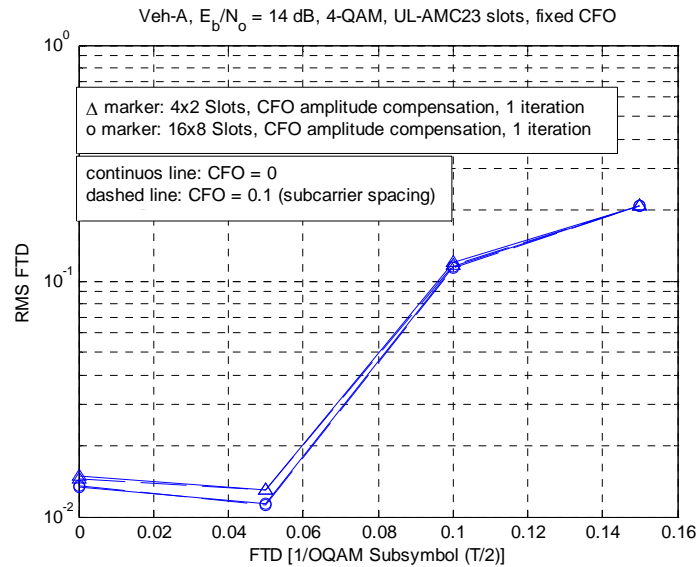


Figure 4-8. RMS error in FTD estimation for fixed CFO = 0 and 10 % of subcarrier spacing. Uplink transmission of 16x8 and 4x2 AMC23 slots in Vehicular-A channel at  $E_b / N_o = 14$  dB using 4-QAM . Synchronization performed with CFO amplitude compensation in the 3-tap equalizer and 1 synchronization iteration.

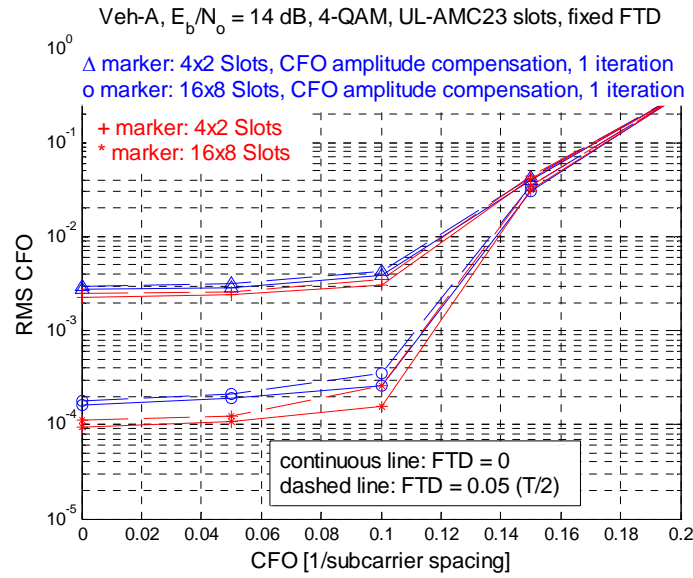


Figure 4-9. RMS error in CFO estimation at fixed FTD = 0 and 5% of FBMC/OQAM subsymbol (T/2) for an uplink transmission of 16x8 and 4x2 AMC23 slots in Vehicular-A channel at  $E_b/N_o = 14$  dB. 4-QAM. Different synchronization options.

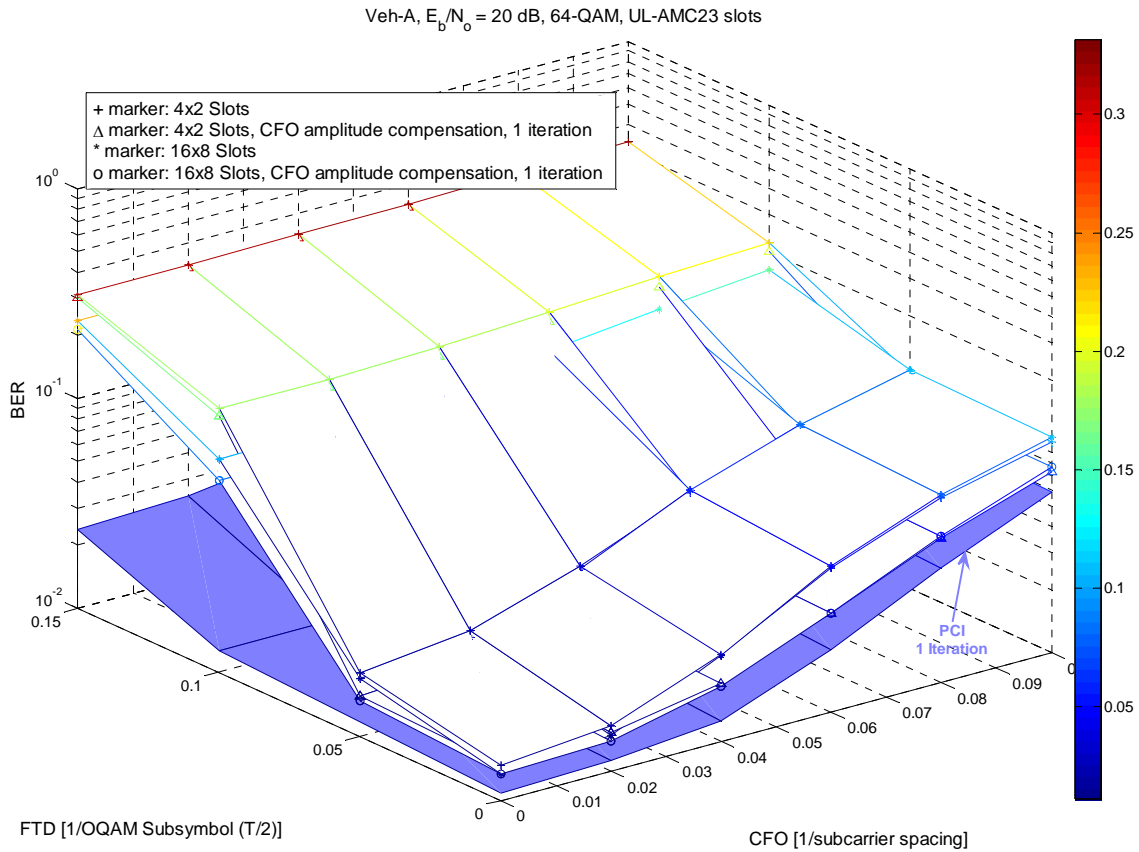


Figure 4-10. BER performance vs. CFO and FTD for uplink transmission of 16x8 and 4x2 AMC23 slots in Vehicular-A channel at  $E_b/N_o = 20$  dB using 64-QAM. Different synchronization options.

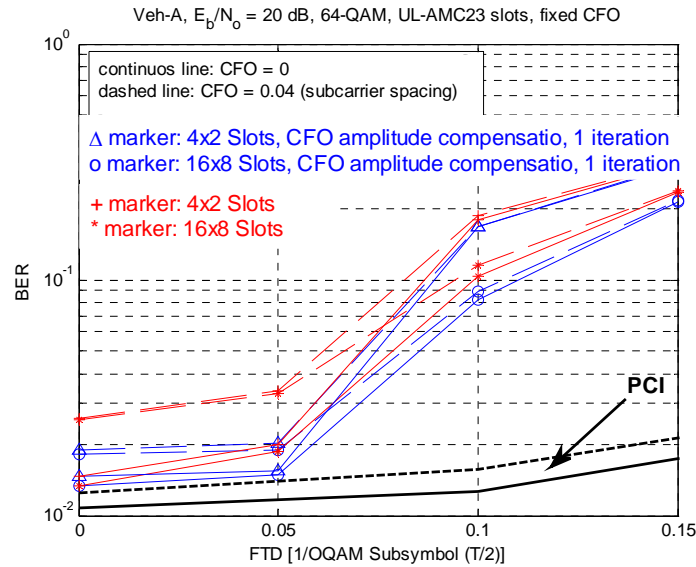


Figure 4-11. BER performance vs. FTD at  $\text{CFO} = 0$  and 4% of subcarrier spacing for an uplink transmission of 16x8 and 4x2 AMC23 slots in Vehicular-A channel at  $E_b/N_o = 20$  dB using 64-QAM. Different synchronization options.

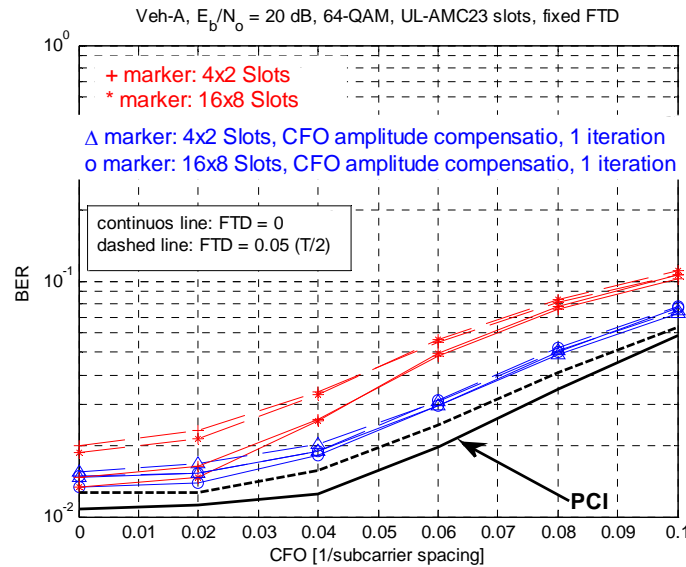


Figure 4-12. BER performance vs. CFO at  $\text{FTD} = 0$  and 5% of FBMC/OQAM subsymbol ( $T/2$ ) for an uplink transmission of 16x8 and 4x2 AMC23 slots in Vehicular-A channel at  $E_b/N_o = 20$  dB using 64-QAM. Different synchronization options.

Finally we focus on the performance with somewhat modified channel conditions, such as mobility of 60 km/h and reduced  $E_b/N_o = 5$  dB. For these simulations we have used the smallest transmission size of 4x2 UL-AMC23 slots and have considered the case with the synchronization iteration. Figure 4-13



shows the BER results. It is interesting to note, that the mobility of 60 km/h has a relatively low effect on the BER performance. The degradation is greatest when reaching the extreme at which the CFO starts to seriously worsen the performance. In Figure 4-14 we can see the effect on the FTD estimation error. Here the mobility case is not included in the figure because it is almost not distinguishable from the static user performance. Figure 4-15 presents the RMS CFO estimation error as a function of the FTD and CFO and the next Figure shows a couple of sections for fixed FTDs. The CFO estimation errors differ visibly for different channel situations. In the channel with more noise, however, the estimation error surpasses 1% of subcarrier bandwidth at 8% CFO. It is also noticeable that, even though the RMS error in the mobility case more than doubles compared to the static user case, the BER performance in this 4-QAM case is still quite close to the static user BER performance. Therefore, for 4-QAM transmission of important mapping and system information data, a CFO RMS error of less than 1% seems to be acceptable.

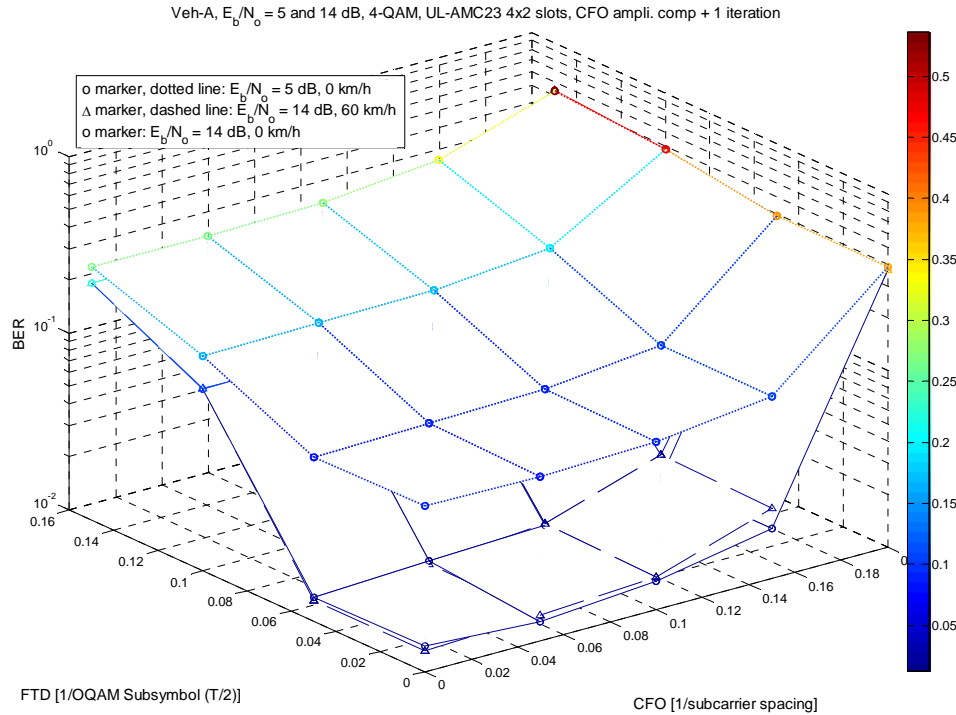


Figure 4-13. BER performance vs. CFO and FTD for uplink transmission of 4x2 AMC23 slots in Vehicular-A channel at  $E_b/N_o = 5$  dB and  $E_b/N_o = 14$  dB using 4-QAM. Static user and user with 60 km/h mobility. Synchronization with CFO amplitude distortion correction and 1 iteration.

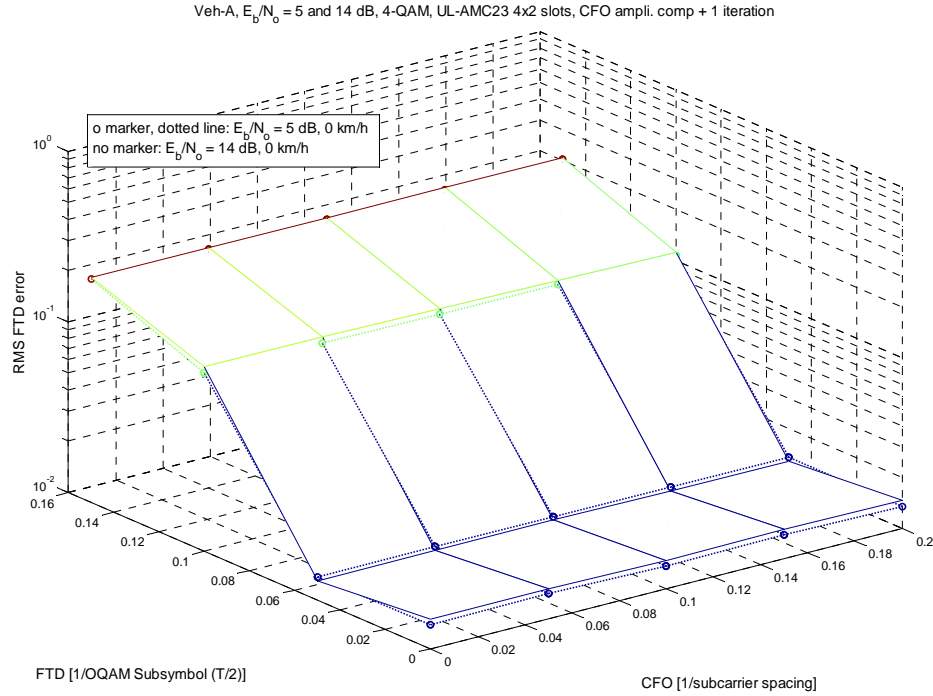


Figure 4-14. RMS FTD error vs. CFO and FTD for uplink transmission of 4x2 AMC23 slots in Vehicular-A channel at  $E_b/N_o = 5$  dB and  $E_b/N_o = 14$  dB using 4-QAM. Synchronization with CFO amplitude distortion correction and 1 iteration.

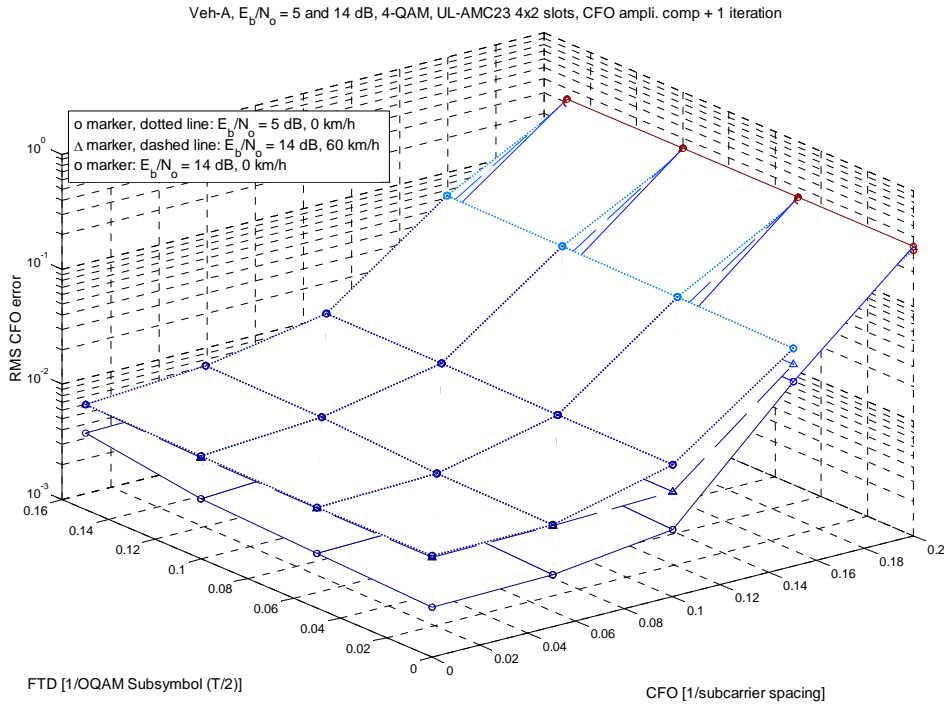


Figure 4-15. RMS CFO error vs. CFO and FTD for uplink transmission of 4x2 AMC23 slots in Vehicular-A channel at  $E_b/N_o = 5$  dB and  $E_b/N_o = 14$  dB using 4-QAM. Static user and user with 60 km/h mobility. Synchronization with CFO amplitude distortion correction and 1 iteration.

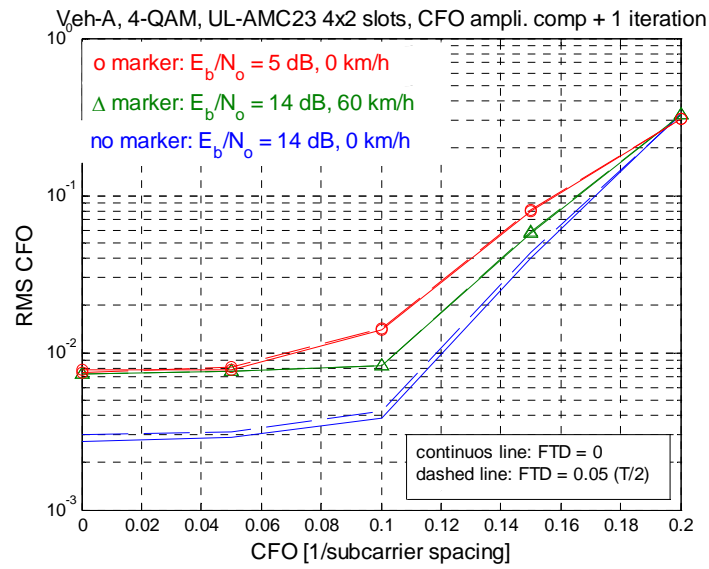


Figure 4-16. RMS CFO error vs. CFO at fixed FTD for uplink transmission of 4x2 AMC23 slots in Vehicular-A channel at  $E_b/N_o = 5$  dB and  $E_b/N_o = 14$  dB using 4-QAM. Static user and user with 60 km/h mobility. Synchronization with CFO amplitude distortion correction and 1 iteration.

### 4.3 The Case of Arbitrary Timing Offset

The two situations of multicarrier burst transmission, namely downlink and uplink, lead to different issues. In the downlink case, the base station sends a burst to all the users and each user receives the full burst and selects the sub-channels which have been allocated to him. The timing offset can be compensated by each user through a time shift, exploiting an estimation of this timing offset. The accuracy required for the estimation depends on the length of the sub-channel equalizers. With a single coefficient sub-channel equalizer, the signal-to-noise ratio (SNR) as a function of the delay is shown in Figure 4-26, for a system with 128 sub-channels. It appears that the residual timing offset must be smaller than 2 samples if the targeted SNR exceeds 40 dB (QAM 256).

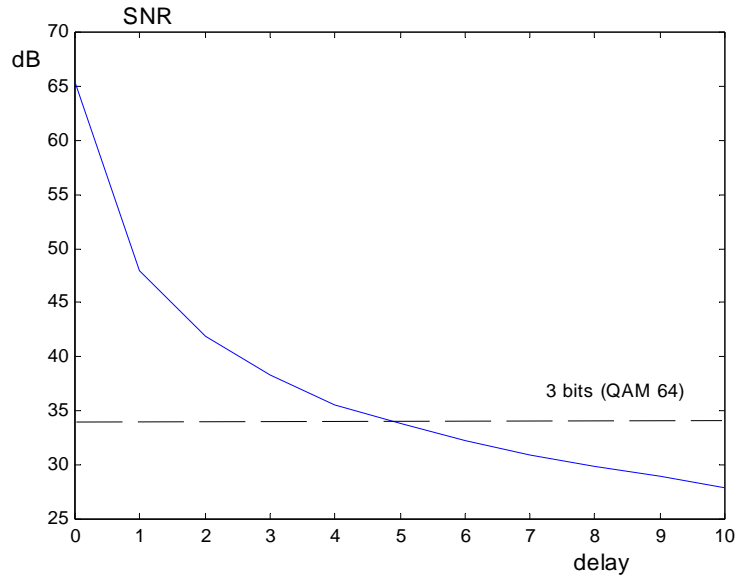


Figure 4-17. SNR versus delay for a single coefficient sub-channel equalizer

In the uplink case, the base station receives signals from users assumed not synchronized, at least at the beginning of the connection. Therefore, it is not possible to implement the relevant time shift to compensate for the timing offset of a particular user. It is shown below that it is possible to design the sub-channel equalizer at the beginning of the burst so that any timing offset can be accommodated.

#### 4.3.1 Sub-channel Equalization with Timing Offset

It is assumed that the burst begins with preamble symbols which are known to the receiver and allow for an estimation of the channel response  $C(i)$  at the center of the sub-channel with index “i”. As soon as the channel frequency response estimation is available, the sub-channel equalizer coefficients are calculated and loaded for the processing of the payload data signal. The block diagram of the receiver is shown in Figure 4-27.

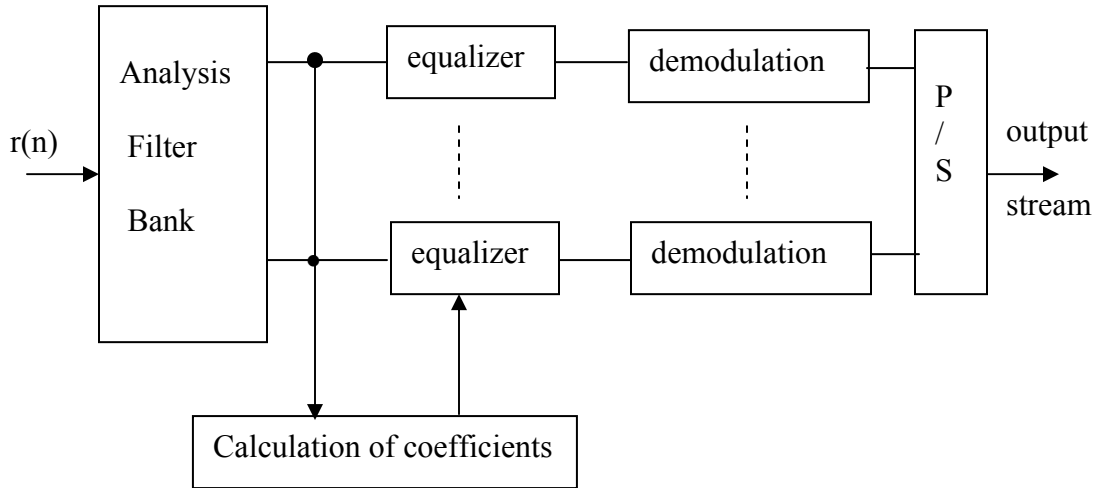


Figure 4-18. Block diagram of the receiver

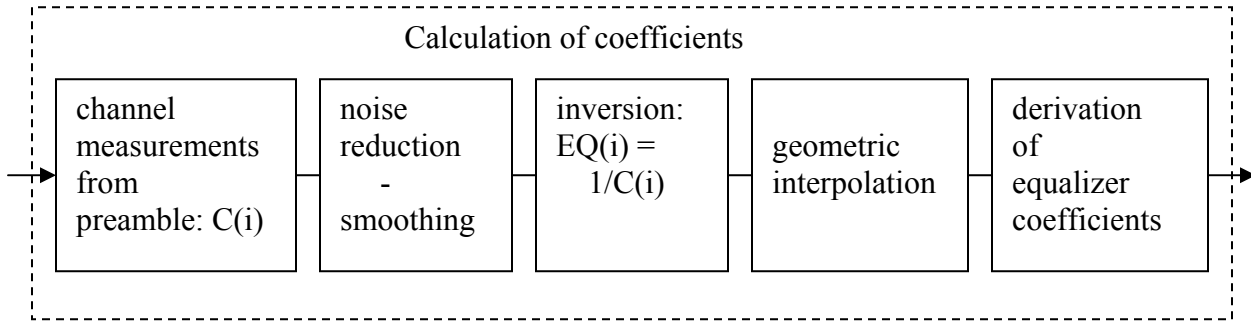


Figure 4-19. Procedure to compute the equalizer coefficients at the beginning of the burst

The procedure proposed to derive the coefficients is depicted in Figure 4-28. It involves 3 main steps, namely noise reduction, geometric interpolation and derivation of coefficient values.

The noise reduction step is useful in the presence of high level noise and it can yield significant gains in SNR. It can be based on the FFT, considering that the channel impulse response is much shorter than the multicarrier symbol period.

The derivation of the coefficient values can be based on the frequency sampling technique described in deliverable D3.1 [8]. Then, frequency domain interpolation is necessary.

*The interpolation problem* : in the presence of a delay, it is necessary, in order to perform the frequency domain interpolation, to separate the amplitude and the phase. Then, conventional linear techniques can be applied. A concise alternative approach is geometric interpolation. In the presence of a pure delay  $\tau$ , the channel response is expressed by

$$C(i) = e^{-j2\pi \frac{i}{N} \tau} \quad (94)$$

where  $N$  is the number of sub-channels. An intermediate sample is expressed by

$$C(i + \frac{1}{2}) = e^{-j2\pi \frac{i+\frac{1}{2}}{N} \tau} = C(i) e^{-j2\pi \frac{\tau}{N} \frac{1}{2}} \quad (95)$$

and

$$C(i + \frac{1}{2}) = C(i) \sqrt{C(i+1)C^*(i)} \quad (96)$$

This is the geometric interpolation, which turns out to be perfectly suited to the pure delay. Obviously, it can be extended to the combination of the channel frequency response and a delay.

#### 4.3.2 Simulation Results

In order to illustrate the performance which can be attained with the above scheme, the following simulation setup is used. The total number of sub-channels is  $N=128$ , of which 115, with indices 8-122, carry data. The sub-channel equalizer has 5 coefficients and 2 samples are interpolated in the frequency domain, between 2 known samples. The curve SNR versus delay is given in Figure 4-29.

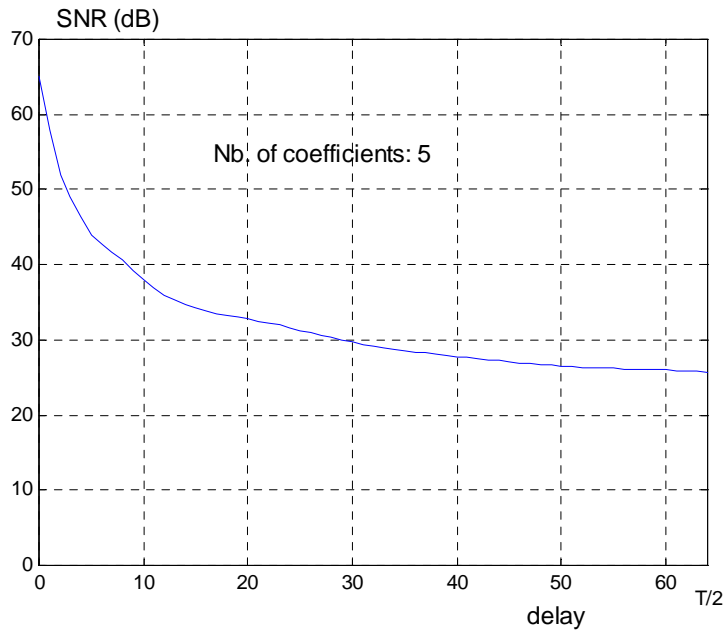


Figure 4-20. Performance of the 5 coefficient equalizer versus delay

The delay 64 corresponds to half the sub-channel sample period and it is the worst case.

From these results, it can be concluded that initial equalization of any delay is possible with a 5 coefficient equalizer. The 26 dB minimum SNR allows for the transmission of 2 bits (QAM16) with a 9 dB margin. Of course, if a time alignment of the distant user is feasible and the delay becomes smaller than 8 samples, then the SNR exceeds 40 dB and QAM256 can be employed with ample margin.

## 5 Achievements and Conclusion

Principal contribution of WP2 to PHYDYAS project has been the definition of a strategy for synchronization, initialization and tracking in single antenna FBMC systems. The main achievements of WP2 and the signal processing tools which have been generated can be resumed in the following list:

- optimized techniques for the joint estimation of CFO and timing offset, considering both full block of sub-channels (downlink) and groups of sub-channels (uplink).
- methods to exploit scattered pilots in the bursts for joint CFO and timing offset estimation and compensation in both downlink and uplink transmission
- a filter bank memory preloading technique to accelerate initialization and ease compatibility with OFDM,
- an impulse response shortening procedure, to minimize the duration of the initialization and overheads in data transmission rate in time-division duplexing based transmission

Research work has been also directed toward the development of simulation software for inclusion in the demonstrator to WP9 for simulation. Precisely, the algorithms developed in the WP2 are

- Scattered pilot based synchronization scheme for WiMAX-like FBMC system, including also the burst truncation functions, and integrated with the filter bank modules developed under WP5.
- Preamble-based and blind synchronization techniques for joint symbol timing and CFO estimation in both the uplink and the downlink scenarios.

The strategies which can be recommended, at the present stage of the work, for initialization in FBMC are related to the considered scenario. These strategies could be:

### 1) Cognitive radio:

- a sequence of  $K+1$  identical preamble symbols is applied to the input of the SFB, to generate two identical signal blocks,
- CFO estimation is performed in the time domain,
- timing offset estimation is performed in the time or frequency domain,
- channel frequency response estimation is obtained,
- the sub-channel equalizer coefficients are derived from the channel estimation,
- adaptive equalizers track the evolutions of the channel during the burst.

The procedure could be repeated for every burst.

### 2) WiMAX-like context (a spectral gap is present between systems)

- filter bank memory preloading is exploited and 2 identical preamble symbols are applied to the input of the SFB,
- same procedure as above,
- impulse response shortening is implemented to reduce the transition time for data at the beginning of the burst and at the end.

### 3) Alternative frequency-domain synchronization scheme

- Initial synchronization resulting in CFO accuracy of  $\pm 10\%$  of subcarrier spacing. (This could take a fairly long time, in the order of 100's of ms). It is assumed that the high-level

synchronization scheme is able to maintain this CFO accuracy also in the idle mode and when switching between different frequency channels.

- Frequency-domain CFO & FTD estimation and compensation, channel estimation and equalization, based on preamble and/or scattered pilots. In contrast, e.g., to WiMAX scheme, strict time-alignment is not required.
- The resulting accuracy after frequency-domain compensation is sufficient for detecting 4QAM modulation. It is assumed that the transmission always begins with 4QAM, but the latter part of the burst (or burst sequence) may carry high-order modulation. After estimating the synchronization parameters, time-domain compensation of CFO and/or FTD is carried out, if needed, before starting the reception of the higher-order modulated waveform.



## 6 References

- [1] M. Morelli, C.C.J. Kuo and M.O. Pun “Synchronization techniques for orthogonal frequency division multiple access (OFDMA): a tutorial review,” *Proc. IEEE* vol. 95, No. 7, pp 1394-1427, July 2007.
- [2] T. Schmidl, D. Cox, "Robust Frequency and Timing Synchronization for OFDM", *IEEE Trans. Comm.*, pp. 1613-1621, December 1997.
- [3] T. Fusco, A. Petrella and M. Tanda, “Data-Aided symbol timing and CFO synchronization for filter bank multicarrier systems,” accepted for publication on *IEEE Trans. Wireless Commun.*
- [4] Deliverable 2.1, “Transmit/receive processing (single antenna),” ICT-211887 PHYDYAS, July 2008.
- [5] T. Fusco, A. Petrella and M. Tanda “Non-data-aided carrier-frequency offset estimation for pulse shaping OFDM/OQAM systems,” *Signal Processing* vol. 88, Issue 8, pp 1958-1970, August 2008.
- [6] T. Fusco, L. Izzo, A. Petrella, M. Tanda: “Blind symbol timing estimation for OFDM-OQAM systems,” *Proc. of 3rd International Symposium on Communications, Control and Signal Processing (ISCCSP 2008)* St. Julians, Malta, March 12-14 2008.
- [7] J.-P. Javaudin, D. Lacroix, A. Rouxel, “Pilot-aided channel estimation for OFDM/OQAM,” in *Proc. Vehicular Technology Conf. (VTC 2003-Spring)*, pp. 1581-1585, April 2003.
- [8] Deliverable 3.1, “Transmit/receive processing (single antenna),” ICT-211887 PHYDYAS, July 2008.
- [9] M. Bellanger, “Frequency offset compensation per sub-channel”, PHYDYAS internal report, April 20